UiO : Department of Physics
University of Oslo

A first principles study of lattice thermal conductivity in *X*NiSn (*X* = Ti, Zr, Hf) half-Heusler alloys for thermoelectric applications

Simen Nut Hansen Eliassen

Master's Thesis, Spring 2016

Summary

The present work investigates heat conduction from lattice vibrations in a class of materials called half-Heuslers. The composition under investigation was *X*NiSn half-Heusler alloys where *X*=Ti, Zr or Hf. These materials have received a lot of attention for their favorable properties for thermoelectric applications. However, their lattice thermal conductivity is too high to be applicable as a thermoelectric material. Previous studies have shown that lattice thermal conductivity can be reduced by isoelectronic substitutions on the *X*-site or by reducing the grain size. The lattice thermal conductivity is calculated by using density functional theory and the phonon Boltzmann transport equation with the frozen phonon approach. Anharmonic three-phonon scattering was used to assess κ_{l} of pure TiNiSn, ZrNiSn and HfNiSn, the results had good accordance to experimental values. However, a slight overestimation was observed due to the fact that experimental samples exhibit microstructures which may affect the κ_{l}. The effect of alloying was then explored within the virtual crystal approximation, making it possible to screen all possible ternary substitutions in the composition $\mathrm{Ti}_x\mathrm{Hf}_y\mathrm{Zr}_{1-x-y}\mathrm{NiSn}$. The lowest κ_{l} was found for the binary substitution where *X*=Ti and Hf, in the composition $\mathrm{Ti}_{0.5}\mathrm{Hf}_{0.5}\mathrm{NiSn}$. Finally, a simple model for boundary scattering was used to quantify the effect of finite grain sizes on κ_{l}. Using values of the grain size obtained from experimental measurements as input when calculating lattice thermal conductivity showed very good accordance to experimental measurements of κ_{l}. This study demonstrated that modeling based on first principles can be used to quantify contributions from various scattering mechanisms and thus predict the thermal conductivity of given alloy compositions with a specific grain size.

Acknowledgments

I would like to express my gratitude to my supervisors, Ole Martin Løvvik and Kristan Berland, for the encouragement the past two years. Their commitment to my supervision gave me motivation from the start to the very end, and their guidance was invaluable for me to finish this thesis.

My stay in the ICAMS-group at Rühr University, Germany, was very pleasant due to the hospitality from the people in the group. A special thanks goes to Georg Madsen for his welcoming attitude and scientific input on the thesis and for making me feel welcome in his team for the short period of time I was there; also, a special thanks goes to Ankita Katre for teaching me to efficiently use the PHONO3PY package and helping me with all coding difficulties I came across. They have both helped me to develop the tools used in this thesis.

The thesis has been a part of the national coordinated project THELMA. I thank all members in the project for helpful input and comments, especially Matthias, Cristina and Raluca. Also, thanks to the BATE-group for their valuable comments under all presentations I held at the Friday-meetings. I am grateful for the great working environment in the Structure Physics group. Aside from studying, I had some great non-scientific related activities with the group. I thank Adrian and Monika for the great company during the numerous coffee breaks. Again, thanks to Adrian for proof-reading the thesis the last two days before deadline.

Lastly, I am grateful for my family for their love and support during all these years.

Contents

List of Figures

List of Tables

Abbreviations

BTE Boltzmann transport equation.

BZ Brillouin zone.

DFT density functional theory.

DOS density of states.

FCC face-centered cubic.

GGA generalized gradient approximation.

LA longitudinal acoustic.

LO longitudinal optic.

MFP mean free path.

PBE Perdew, Burke and Ernzerhof.

RTA relaxation time approximation.

TA transverse acoustic.

TO transverse optic.

VCA virtual crystal approximation.

Chapter 1

Introduction

A higher demand for energy can be related to an increased population and higher standard of living. We are today strongly dependent on energy sources as fossil fuels, and it is well known that fossil fuels contaminate the climate with emission of greenhouse gases. We need to find new energy sources which are renewable and clean, with no emission of additional greenhouse gases.

There are a lot of energy that dissipates into the atmosphere in the form of heat. This waste heat could be utilized to produce electricity, but the conversion efficiency is too low to have an impact on a global energy scale. Thermoelectricity could be used for this purpose, which is related to direct conversion of a heat to electricity, or vice versa. As a power generator, thermoelectricity has found its way into some niche application areas, e.g. space probes. This is due to the durability and stability of thermoelectric power generators. On the other hand, thermoelectric materials can be used as refrigerators and spot-on coolers for micro-electronics.

It has been invested a lot in research to obtain high-performance thermoelectric materials: one route is to find new materials, and another route is to carefully engineer existing materials in such a way that they exhibit the properties of interests.

This chapter will be an introduction to thermoelectricity and the physical properties which govern the conversion efficiency. The end of this chapter will include a motivation of the thesis.

1.1 Thermoelectricity

Thermoelectricity can be described as a two way process. One of the descriptions is conversion of heat into electricity. This process make use of a temperature gradient over the materials to produce electricity. The reverse effect uses an electric current through

the material to produce a temperature difference on each side. These two processes are called the Seebeck effect and Peltier effect, respectively.

1.1.1 Seebeck Effect

In 1821, T. J. Seebeck discovered the first of the thermoelectric effects. He showed that by joining two dissimilar materials, and holding the junction at two different temperatures, i.e. T and $T + \Delta T$, produces a voltage difference across the junction.

The mobile charge carriers on the hot side will diffuse to the cold side which results in an electric field opposite of the motion of the charges. One says that the system is in equilibrium when no more diffusion occurs due to the opposed electric field.

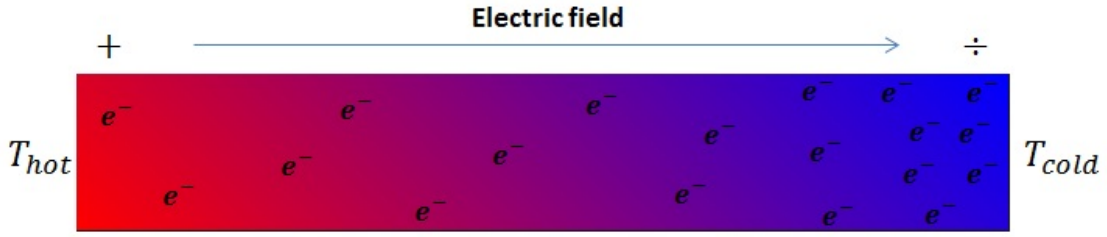

Figure 1.1: An illustration of a thermoelectric material in a temperature gradient. The negative charge carriers diffuses from the hot side to the cold side, which induces an electric field.

The voltage difference between the hot and the cold side is called the Seebeck voltage. This voltage per unit temperature difference is called the Seebeck coefficient S, also known as the thermopower, and has units of V/K. This is an intrinsic property of the material and the Seebeck coefficient is defined as

$$S = -\frac{\Delta V}{\Delta T} = -\frac{V_{\text{hot}} - V_{\text{cold}}}{T_{\text{hot}} - T_{\text{cold}}}, \tag{1.1}$$

where ΔV is the voltage difference between the hot and the cold side and ΔT is the temperature difference.

1.1.2 Peltier Effect

A few years later, J. C. Peltier discovered another effect which is nowadays known as the Peltier effect. He observed that when an electrical current passes through a junction of two dissimilar materials, heat was either rejected or absorbed at the junction. The heat absorbed or rejected at the junction per unit time is defined as

$$Q = (\Pi_A - \Pi_B)I, \tag{1.2}$$

where Π_A and Π_B are the Peltier coefficient of material *A* and *B*, respectively. The Peltier coefficient is a measure of the amount of heat carried per unit charge. This effect is largely due to the difference in Fermi energies of the two materials [1].

The Seebeck and Peltier coefficient are related to each other by a simple relation, known as one of the Thomson relations,

$$\Pi = TS. \tag{1.3}$$

The simple relation states that the Peltier coefficient is proportional to the Seebeck coefficient at a given temperature.

1.1.3 Figure of Merit

The efficiency of a thermoelectric material can be determined by the dimensionless factor called the *figure of merit* (ZT),

$$ZT = \frac{S^2\sigma}{\kappa_\mathrm{e} + \kappa_\mathrm{l}}T, \tag{1.4}$$

where S is the Seebeck coefficient, σ is the electrical conductivity and the numerator $S^2\sigma$ is called the power factor. The denominator is the total thermal conductivity, where κ_e and κ_l are the electronic- and lattice contributions, respectively. A high ZT value denotes a good thermoelectric material, and ZT higher than one are considered good thermoelectric materials.

For an efficient process, it is necessary to have materials with good electrical conductivity; otherwise, the scattering of electrons will generate heat on both sides of the material and reduce the thermal gradient. Similarly, the Seebeck coefficient has to be maximized to produce the highest possible voltage difference. To maintain a high thermal gradient between the hot and cold side, the material should be a poor thermal conductor. All the parameters are strongly influenced by the material's crystal structure; therefore, the parameters are interdependent. The electrical conductivity and the electronic contribution to the thermal conductivity are proportional to each other, which is given by the Wiedemann-Franz law,

$$\kappa_\mathrm{e} = \sigma LT, \tag{1.5}$$

where L is called the Lorentz number which is a function of charge carrier concentration and temperature. Because of the propotionality of electrical conductivity and electronic contribution to thermal conductivity, obtaining a low thermal conductivity and a high

power factor at the same time requires a low lattice contribution to the thermal conductivity.

1.1.4 Thermoelectric Materials

There exist various thermoelectric materials which operates at different working temperatures with different efficiency. Ioffe reported as early as in 1957 that the best thermoelectric materials are the heavily doped semiconductors [2]. Figure 1.2 presents some of the most common thermoelectric materials for energy generation or refrigeration.

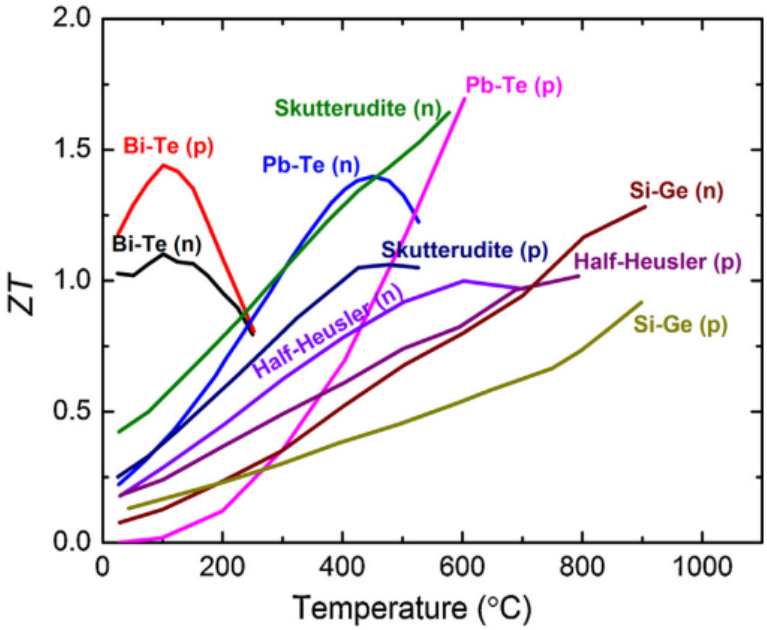

Figure 1.2: The figure of merit as a function of temperature for different n- and p-type thermoelectric materials [5].

The most widespread application of thermoelectric materials is in refrigeration purposes at room temperature with materials such as alloys of Bi_2Te_3 and Sb_2Te_3 and Bi_2Se_3 [3]. For thermoelectric generation at temperatures in the range of 500-900$^\circ C$, materials based on group-IV tellurides are typically used such as PbTe, GeTe or SnTe [4]. For applications at higher temperatures, the Si-Ge alloys have been used [3].

Other interesting materials for thermoelectric applications are structures which contains cages within the unit cell. Skutterudites [6, 7] and clathrates [8, 9] are such materials, and have shown promising thermoelectric properties. One advantage of these types of materials is the possibility to fill the cages resulting in an effective reduction of

the lattice thermal conductivity. Another potential class of materials for thermoelectric applications is the half-Heusler alloys, which will be discussed in the next section.

1.2 Half-Heusler Alloys

Half-Heusler alloys are ternary compounds with the general formula *XYZ* which forms the MgAgAs structure. The *X*, *Y* and *Z* atoms form three interpenetrating face-centered cubic (FCC) sublattices, with corresponding Wyckoff positions at 4a (0, 0, 0), 4b (1/2, 1/2, 1/2) and 4c (1/4, 1/4, 1/4). The half-Heusler structure can be viewed as a sublattice of the zinc-blende structure which consists of atoms at Wyckoff positions 4a and 4c with an interpenetrating rock-salt structure with atoms at position 4a and 4b, as illustrated in figure 1.3.

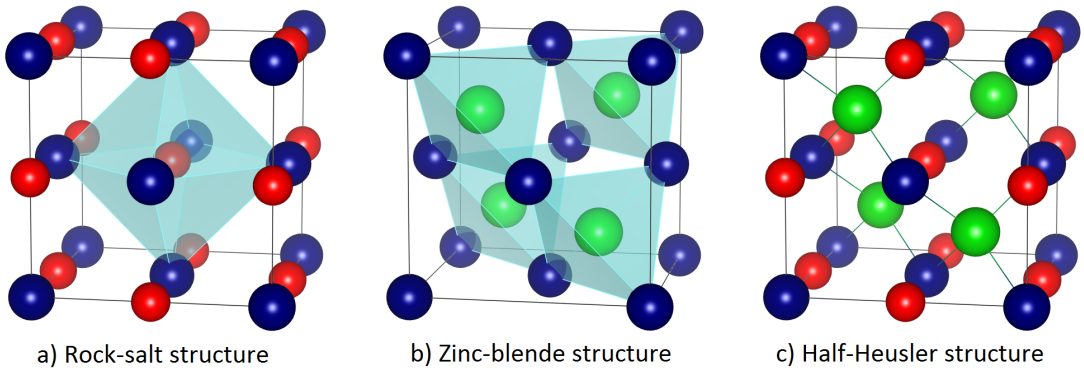

Figure 1.3: An illustration of a) rock-salt b) zinc-blende and the c) half-Heusler structure. This figure and all other atomic models are made in the visualization tool VESTA [10].

Half-Heusler alloys are particular interesting due to the wide variety of combinations making it possible to use inexpensive, earth-abundant and environmentally friendly elements [11]. The possible choices of the X, Y and Z atoms are shown in figure 1.4. Another great advantage is the possibilities for doping on the Z site to improve the charge carrier concentration and simultaneously introduce mass-disorder on the X and Y site to decrease the lattice thermal conductivity.

One of the most promising half-Heusler for thermoelectric application is the n-type *X*NiSn, where *X*=Ti, Zr or Hf. The *X*NiSn alloys are narrow band gap semiconductors resulting in a high effective mass and large Seebeck coefficient [13, 14]. Combining their high Seebeck coefficient with their high electrical conductivity, a high power factor may be achieved [15, 16]. However, their relatively high thermal conductivity remains a problem for efficient energy conversion [15–19]. The thermal conductivity is reported

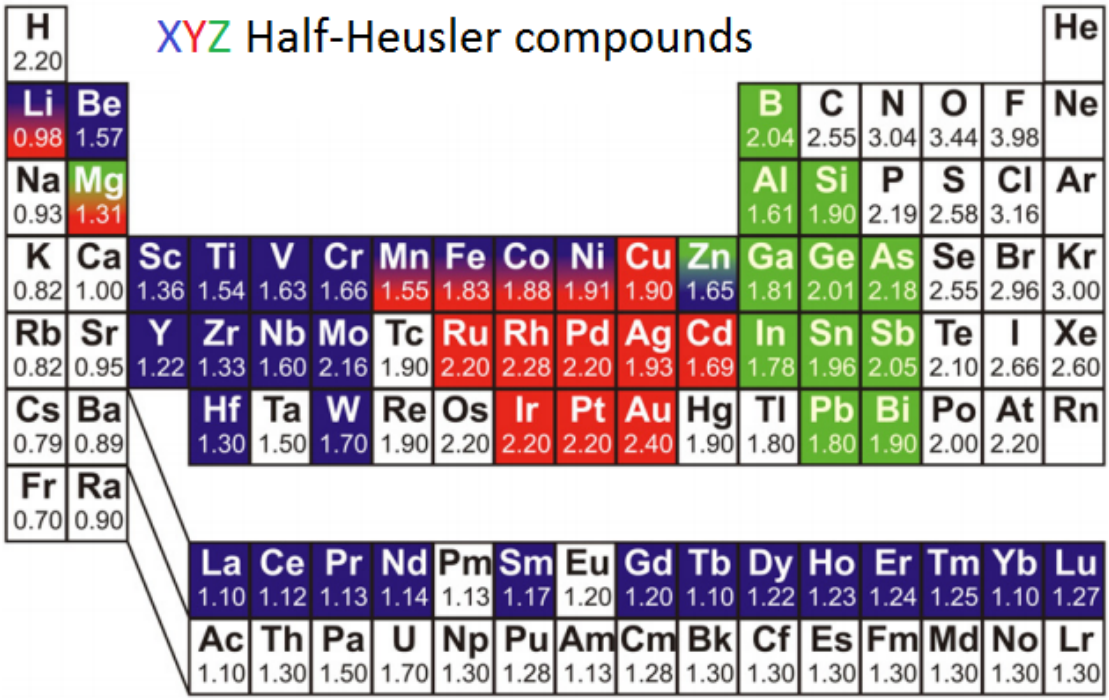

Figure 1.4: The periodic table of the elements with a color scheme for the possibilities of the X, Y and Z atoms in the half-Heusler compound [12].

to be as high as 15 W/mK, which is almost five times greater than commercial Bi_2Te_3 [20].

Various methods have been deployed to reduce the thermal conductivity. An isoelectronic substitution on the X-site has shown to efficiently reduce the thermal conductivity without altering the electric conductivity [5, 16, 18, 21–25]. A binary substitution at the X-site has shown to reduce κ_l up to 50% [23, 26–28]. Ternary substitution at the X-site can further reduce κ_l [21, 29–31].

Heat carriers in the low frequency range are particularly sensitive to scattering from grain boundaries, and lowering the grain size in XNiSn alloys has shown to be an effective method to reduce κ_l [15, 24, 26, 32–36].

1.3 Motivation for the Thesis

The XNiSn half-Heusler alloys are promising candidates for thermoelectric application. Maintaining the temperature gradient is vital for the material to be considered a good thermoelectric material; however, the half-Heusler alloys have shown to have a lattice thermal conductivity five times greater than commercial Bi_2Te_3. The main goal for

the thesis is to investigate the quantities that govern lattice thermal conductivity in the *X*NiSn alloys. Lattice thermal conductivity is directly related to the phonons in a lattice structure. The dynamics of the phonons can be calculated from first principles, and this thesis will conduct such calculations within the harmonic approximation. The calculations will yield frequency of the phonons and other related properties, e.g. density of states and heat capacity. The harmonic approximation fails to capture interactions between phonons; thus, the heat transport within the harmonic approximation are perfect. To calculate the lattice thermal conductivity, anharmonicity has to be included. Once the anharmonicity is included in the calculations, one have the possibility to calculate the phonon-phonon scattering rates and the lattice thermal conductivity.

First principles calculations with mass-disorder and boundaries will be very computational demanding; thus, the thesis will investigate additional models to account for scattering mechanisms for a reduction in κ_l: scattering from mass-disorder and grain boundaries. Quantifying an effective and predictive model for these scattering mechanisms will be one of the goals of the thesis.

Chapter 2

Theory of Phonons

The physics behind phonons is important in order to understand how to obtain a low lattice thermal conductivity. Phonons can be described as collective excitations of atoms or molecules in condensed matter phases. The word "phonon" stems from the Greek word "$\phi\omega\nu\hat{n}$", which translates to sound or voice.

This chapter will start with some basic solid state physics: a description of crystal lattices in real and reciprocal space. Section 2.2 will discuss lattice dynamics and derive the dynamical matrix within the harmonic approximation. However, there are no interactions between the vibrations within the harmonic approximation; thus, the heat conduction is infinite. Including phonon-phonon interactions is necessary in order to calculate the lattice thermal conductivity, and the derivation of the phonon-phonon interactions is shown in the following section. The chapter ends with a description of different scattering mechanisms which will be utilized in the calculations of lattice thermal conductivity.

The structure of this chapter is inspired by the references [37, 38]. Additional details can be found in the references [39, 40]. The basics of solid state physics can be found in any introductory solid state physics text book, such as [41, 42].

2.1 Periodic Crystal Structures

2.1.1 Bravais Lattice

An ideal crystal consists of an infinite repetition of an identical group of atoms. This group is called a basis and may consist of just one atom or a volume of several atoms. The position of the basis may be described with the translation vectors $\mathbf{a}_1$, $\mathbf{a}_2$ and $\mathbf{a}_3$, in such way that any point $\mathbf{R}$ has the exact same surroundings translated by any integer of

the translation vectors,

$$\mathbf{R} = l_1\mathbf{a}_1 + l_2\mathbf{a}_2 + l_3\mathbf{a}_3, \tag{2.1}$$

where l_1, l_2 and l_3 are arbitrary integer numbers. The set of $\mathbf{R}$ for all l_1, l_2 and l_3 defines the crystal lattice.

A primitive unit cell consists of only one lattice point, whereas a non-primitive unit cell consists of several lattice points. The conventional cubic unit cell is one such non-primitive unit cell. The primitive unit cell has a smaller volume compared to the conventional unit cell. The figure 2.1 illustrates the difference in the shape of a conventional and primitive unit cell. There are a limited number of possible arrangements of the lattice points. The set of the possible arrangements are known as Bravais lattices, and there exists in total 14 such lattices.

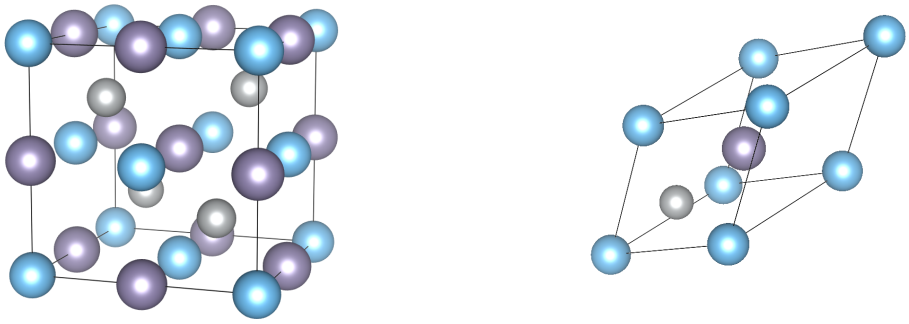

(a) Conventional unit cell

(b) Primitive unit cell

Figure 2.1: Comparison of a conventional versus primitive half-heusler.

2.1.2 Reciprocal Lattice

Every crystal structure has two lattices associated with it: one in real space and one in reciprocal space. The reciprocal lattice is a periodic set of points which obeys the relation

$$e^{i\mathbf{G}\cdot\mathbf{R}} = 1, \tag{2.2}$$

where the vector $\mathbf{G}$ is the reciprocal lattice vector which constructs the lattice points in the reciprocal space. The units of the vectors in real space are length, but the units in the reciprocal space are given as the inverse of the length.

The $\mathbf{G}$-vector is defined as a set of reciprocal translation vectors times any integer number m_1, m_2 and m_3,

$$\mathbf{G} = n_1\mathbf{b} + n_2\mathbf{b}_2 + n_3\mathbf{b}_3, \tag{2.3}$$

where $\mathbf{b}_1$, $\mathbf{b}_2$ and $\mathbf{b}_3$ are the reciprocal translation vectors. The vectors $\mathbf{b}_1$, $\mathbf{b}_2$ and $\mathbf{b}_3$ can be constructed from the vectors of the Bravais lattice the following way,

$$\mathbf{b}_1 = \frac{2\pi}{\Omega}\mathbf{a}_2 \times \mathbf{a}_3; \quad \mathbf{b}_2 = \frac{2\pi}{\Omega}\mathbf{a}_1 \times \mathbf{a}_3; \quad \mathbf{b}_3 = \frac{2\pi}{\Omega}\mathbf{a}_1 \times \mathbf{a}_2, \tag{2.4}$$

where $\Omega = |\mathbf{a}_1 \cdot (\mathbf{a}_2 \times \mathbf{a}_3)|$ is the volume of the primitive unit cell in the real space. From equation (2.1), (2.3) and (2.4), one can derive the following property,

$$\mathbf{a}_i \cdot \mathbf{b}_j = 2\pi\delta_{ij}. \tag{2.5}$$

δ_{ij} is the Kronecker's delta, which is equal to 1 if $i = j$ and zero otherwise.

An alternative way to view the reciprocal lattice vectors is by viewing them as wave vectors which yields plane waves with the periodicity of the Bravais lattice,

$$e^{i\mathbf{G}\cdot\mathbf{r}} = e^{i\mathbf{G}\cdot\mathbf{r}}e^{i\mathbf{G}\cdot\mathbf{R}} = e^{i\mathbf{G}\cdot(\mathbf{r}+\mathbf{R})}, \tag{2.6}$$

where $\mathbf{r}$ is the position vector of an atom in a unit cell. This definition obeys the relation $e^{i\mathbf{G}\cdot\mathbf{R}} = 1$ from equation (2.2).

A more detailed, physical and mathematical, description of the reciprocal space can be found in any solid state physics book [41, 42].

2.1.3 Brillouin Zone

The Brillouin zone (BZ) is an uniquely defined volume in the reciprocal space, and the boundaries of the volume are related to planes between lattice points in the reciprocal lattice. The BZ is constructed by placing planes normal to the mid-point of the reciprocal lattice vector $\mathbf{G}$. The first BZ is the volume enclosed by such planes with the shortest possible reciprocal lattice vector. Any position inside the first BZ is closer to the lattice point of origin compared to any other points in the crystal lattice.

An illustration of the first BZ for a body-cetered cubic (BCC) and for a face-centered cubic (FCC) is given in figure 2.2. The letters in the figure 2.2a and 2.2b denotes high symmetry points. At such a point, the distance to the origin is equal to the distance to the nearest lattice point.

By using Bloch's wave description of periodic structures, it is found that the solution of the wave function for the whole structure can be characterized by the behavior within

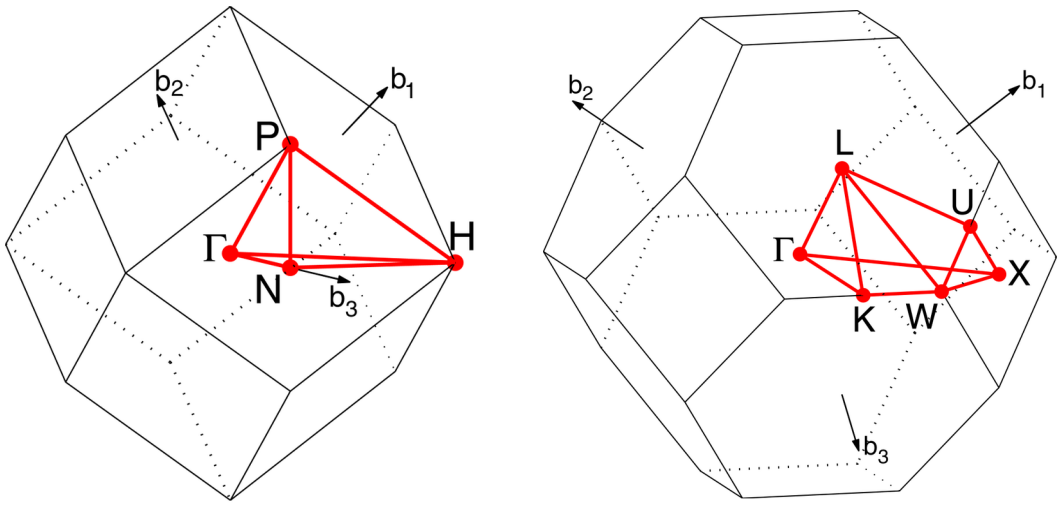

(a) 1st BZ of BCC **(b)** 1st BZ of FCC

Figure 2.2: The first BZ of a) BCC and b) FCC structure with the symmetry points [43].

a single BZ. Furthermore, by using the symmetry in the point group of the lattice the first BZ can be reduced to the irreducible BZ. It is common to utilize this symmetry in computational methods to reduce the cost of the calculations; thus, it is only necessary to solve Schrödinger's equation for a periodic crystal structure within the irreducible BZ.

2.2 Classical Description of Lattice Dynamics

2.2.1 Traveling Waves in a Crystal

Born and von Kármán introduced the concept of periodic boundary condition, and the condition is used to describe an infinitely large system using smaller unit cells of the system. An effect of the periodic boundary condition is that one can ignore the surfaces; thus, makes it convenient to describe bulk properties.

In an unbounded crystal, the vibrations are considered as traveling waves extending throughout the whole crystal. The atomic displacement u_α from its equilibrium position $r(\mathbf{lb})$ can be expressed as

$$u_\alpha(\mathbf{lb}, t) = \frac{1}{\sqrt{m_b}} U_\alpha(\mathbf{b}|\mathbf{q}) \mathrm{e}^{\mathrm{i}(\mathbf{q}\cdot\mathbf{l} - \omega(\mathbf{q})t)}. \tag{2.7}$$

The displacement $u_\alpha(\mathbf{lb}, t)$ is along the α-direction, where $\alpha = 1, 2, 3$ and represents the Cartesian axes, and it depends on the wave vector $\mathbf{q}$ of the traveling wave. The vectors $\mathbf{l}$

and $\mathbf{b}$ are the position vectors of the unit cell l and atom b, respectively. Further notations will address unit cells as l and atoms as b; it is given that the unit cell l and atom b have a corresponding position vector $\mathbf{l}$ and $\mathbf{b}$, respectively. $U_\alpha(\mathbf{b}|\mathbf{q})$ describes the amplitude and direction of the motion of atom b, as produced by a lattice wave with wave vector $\mathbf{q}$. The angular frequency as a function of $\mathbf{q}$ is called the dispersion relation for the propagation of traveling waves.

Because of the periodicity, the directions and amplitudes of the motions for atom b in unit cell l is equal to the directions and amplitudes of the motions of the corresponding atom b in a different unit cell l' where $l \neq l'$. Thus, one only need to consider $3n$ motions with n equal to the number of atoms in the unit, instead of the motion of all atoms in the crystal.

2.2.2 Interatomic Forces

The crystal potential energy denotes the formation energy of the crystal with the atoms in their equilibrium position. The atoms vibrate around their equilibrium position shown as the atomic displacement in equation (2.7).

The crystal potential energy is given as $V(u_\alpha(\mathbf{lb}), u_\beta(\mathbf{l'b'}), u_\gamma(\mathbf{l''b''}), \cdots)$, and it can be expressed as a function of the instantaneous displacement $u_\alpha(\mathbf{lb})$ of all atoms. It is not only a function of the displacement of a single atom, but contains also the displacement of two or more displaced atoms simultaneously. The expression can be expanded as a Taylor series:

$$\begin{aligned} V &= V_0 + \sum_{\mathbf{lb}} \sum_{\alpha} \left.\frac{\partial V}{\partial u_\alpha}\right|_0 u_\alpha(\mathbf{lb}) + \frac{1}{2} \sum_{\mathbf{lb},\mathbf{l'b'}} \sum_{\alpha\beta} \phi_{\alpha\beta}(\mathbf{lb},\mathbf{l'b'}) u_\alpha(\mathbf{lb}) u_\beta(\mathbf{l'b'}) \\ &\quad + \frac{1}{3!} \sum_{\mathbf{lb},\mathbf{l'b'},\mathbf{l''b''}} \sum_{\alpha\beta\gamma} \phi_{\alpha\beta\gamma}(\mathbf{lb},\mathbf{l'b'},\mathbf{l''b''}) u_\alpha(\mathbf{lb}) u_\beta(\mathbf{l'b'}) u_\gamma(\mathbf{l''b''}) + \cdots \\ &= V_0 + V_1 + V_2 + V_3 + \cdots , \end{aligned} \tag{2.8}$$

where V_0 is an energy constant at the equilibrium position. The first derivative is equal to the force exerted on the displaced atom b in the unit cell l by all other atoms in the crystal,

$$F_\alpha(\mathbf{lb}) = -\frac{\partial V}{\partial u_\alpha(\mathbf{lb})}. \tag{2.9}$$

The subscript 0 in the Taylor expansion of the potential energy from equation (2.8) denotes that one are evaluating the positions in the equilibrium configuration. Thus, the forces are zero, and one can exclude V_1 from equation (2.8).

The second-order forces constants is given by $\phi_{\alpha\beta}$, which is the second derivative of the crystal potential,

$$\phi_{\alpha\beta}(\mathbf{lb}, \mathbf{l'b'}) = -\left.\frac{\partial^2 V}{\partial u_\alpha(\mathbf{lb})\partial u_\beta(\mathbf{l'b'})}\right|_0 = -\left.\frac{\partial F_\alpha(\mathbf{lb}, \mathbf{l'b'})}{\partial u_\beta(\mathbf{l'b'})}\right|_0. \tag{2.10}$$

$\phi_{\alpha\beta}(\mathbf{lb}, \mathbf{l'b'})$ represents the forces exerted on atom b in unit cell l in direction α by an unit displacement in the β-direction of atom b' in unit cell l'.

$\phi_{\alpha\beta\gamma}$ denotes the third-order force constants which are related to the third derivative of the crystal potential energy,

$$\begin{aligned}\phi_{\alpha\beta\gamma}(\mathbf{lb}, \mathbf{l'b'}, \mathbf{l''b''}) &= \left.\frac{\partial^3 V}{\partial u_\alpha(\mathbf{lb})\partial u_\beta(\mathbf{l'b'})\partial u_\gamma(\mathbf{l''b''})}\right|_0 \\ &= -\left.\frac{\partial^2 F_\alpha(\mathbf{lb}, \mathbf{l'b'})}{\partial u_\beta(\mathbf{l'b'})\partial u_\gamma(\mathbf{l''b''})}\right|_0.\end{aligned} \tag{2.11}$$

$\phi_{\alpha\beta\gamma}(\mathbf{lb}, \mathbf{l'b'}, \mathbf{l''b''})$ represents the forces exerted on atom b in unit cell l in direction α when two other atoms $l'b'$ and $l''b''$ are displaced in the β- and γ-direction, respectively.

From equation (2.10), one see that the second-order force constants $\phi_{\alpha\beta}(\mathbf{lb}, \mathbf{l'b'})$ must follow the symmetry condition:

$$\phi_{\alpha\beta}(\mathbf{lb}, \mathbf{l'b'}) = \phi_{\beta\alpha}(\mathbf{l'b'}, \mathbf{lb}). \tag{2.12}$$

The periodicity of the lattice requires that if a unit cell is translated relative to itself by a lattice vector $\mathbf{R}(\mathrm{l})$, it will coincide with itself; that is, for any integer of the unit cell l, the force from a displacement of a single atom b will have the same value, independently of the unit cell l. It makes the second-order force constants $\phi_{\alpha\beta}(\mathbf{lb}, \mathbf{l'b'})$ not separately dependent on the cell indices l and $\mathrm{l'}$, but the relative cell index $\mathrm{l'} - \mathrm{l}$. This result can be expressed as a function of the relative position vector of the unit cell,

$$\phi_{\alpha\beta}(\mathbf{lb}, \mathbf{l'b'}) = \phi_{\alpha\beta}(\mathbf{0b}, (\mathrm{l'} - \mathrm{l})\mathbf{b'}), \tag{2.13}$$

which is called the *lattice translation symmetry* condition.

2.2.3 The Dynamical Matrix

Within the harmonic approximation, one only consider the force constants in the Taylor series up to the second derivative. Ignoring the higher ordered terms of (2.8), the

potential energy can be written as

$$V_{\text{harm}} = V_0 + \frac{1}{2} \sum_{\mathbf{0b},(\mathbf{l}'-\mathbf{l})\mathbf{b}'} \sum_{\alpha\beta} \phi_{\alpha\beta}(\mathbf{0b}, (\mathbf{l}'-\mathbf{l})\mathbf{b}') u_\alpha(\mathbf{0b}) u_\beta((\mathbf{l}'-\mathbf{l})\mathbf{b}'), \tag{2.14}$$

where we have used the lattice translation symmetry condition.

The equations of motion for the bth atom in the lth unit cell can be written as follows,

$$m_b \ddot{u}_\alpha(\mathbf{0b}, t) = - \sum_{(\mathbf{l}'-\mathbf{l})\mathbf{b}'} \sum_{\beta} \phi_{\alpha\beta}(\mathbf{0b}, (\mathbf{l}'-\mathbf{l})\mathbf{b}') u_\beta((\mathbf{l}'-\mathbf{l})\mathbf{b}', t), \tag{2.15}$$

where m_b is the mass of the bth atom. The coefficient $\phi_{\alpha\beta}(\mathbf{0b}, (\mathbf{l}'-\mathbf{l})\mathbf{b}')$ represents the forces along the α-direction exerted on the bth atom, when the b'th atom is displaced in the β-direction in the unit cells $l'-l$ relative to each other.

By substituting the atomic displacement in equation (2.7) into the equation of motions (2.15), one get

$$\omega^2(\mathbf{q}) U_\alpha(\mathbf{b}|\mathbf{q}) = \sum_{\mathbf{b}'\beta} D_{\alpha\beta}(\mathbf{b}\mathbf{b}'|\mathbf{q}) U_\beta(\mathbf{q}|\mathbf{b}'), \tag{2.16}$$

with non-trivial solutions when

$$|D_{\alpha\beta}(\mathbf{b}\mathbf{b}'|\mathbf{q}) - \omega^2(\mathbf{q}) \delta_{\alpha\beta} \delta_{\mathbf{b}\mathbf{b}'}| = 0. \tag{2.17}$$

The matrix $D_{\alpha\beta}(\mathbf{b}\mathbf{b}'|\mathbf{q})$ is called the *dynamical matrix* and is given as

$$D_{\alpha\beta}(\mathbf{b}\mathbf{b}'|\mathbf{q}) = \frac{1}{\sqrt{(m_b m_{b'})}} \sum_{(\mathbf{l}'-\mathbf{l})} \phi_{\alpha\beta}(\mathbf{0b}, (\mathbf{l}'-\mathbf{l})\mathbf{b}') \mathrm{e}^{\mathrm{i}\mathbf{q}\cdot(\mathbf{l}'-\mathbf{l})}. \tag{2.18}$$

The dynamical matrix consists of $3n \times 3n$ matrix elements: the second-order force constant matrix which is a 3×3 matrix and $n \times n$ pairs of atom b and atom b'. Thus, equation (2.17) will have $3n$ solutions for each wave vector $\mathbf{q}$. The frequency will be denoted as $\omega(j\mathbf{q})$, where $j = 1, 2, 3, \cdots, 3n$, and it represents the phonon branches. Thus, there exists $3n$ frequencies for each wave vector $\mathbf{q}$.

It can be shown that the dynamical matrix is *Hermitian* for any value of $\mathbf{q}$ [40],

$$D_{\alpha\beta}(\mathbf{b}\mathbf{b}'|\mathbf{q}) = (D_{\alpha\beta}(\mathbf{b}'\mathbf{b}|\mathbf{q})^*)^T. \tag{2.19}$$

This implies that the phonon dispersion squared are real; thus, $\omega(j\mathbf{q})$ is either real or purely imaginary. From the equation for atomic displacement (2.7), a purely imaginary

$\omega(j\mathbf{q})$ would imply that the atomic displacement increases exponentially to infinity or decreases exponentially to zero. Imaginary solutions denotes an unstable crystal structure; thus, only real values of the phonon dispersion $\omega(j\mathbf{q})$ are expected to meet the condition of crystal stability.

The collective motion of atom b in the α-direction for a given phonon branch j and wave vector $\mathbf{q}$ can be described with a polarisation vector $\mathbf{e}_\alpha(\mathbf{b}|j\mathbf{q})$. One particularly element of the polarisation vector describes the motion of a given atom b, vibrating in a given phonon mode $j\mathbf{q}$ along x-, y- or z-direction. Thus, the polarisation vector is a $3n \times 1$ column matrix, and it can be expressed as

$$\mathbf{e}_\alpha(\mathbf{b}|j\mathbf{q}) = \begin{Bmatrix} U_1(1|j\mathbf{q}) \\ U_2(1|j\mathbf{q}) \\ U_3(1|j\mathbf{q}) \\ U_1(2|j\mathbf{q}) \\ \vdots \\ U_3(n|j\mathbf{q}) \end{Bmatrix}. \tag{2.20}$$

The polarisation vector $\mathbf{e}(\mathbf{b}|j\mathbf{q})$ is an eigenvector consisting of n linearly independent vectors, satisfying the orthonormality and closure conditions, given as

$$\sum_{\mathbf{b}\alpha} \mathbf{e}^*_\alpha(\mathbf{b}|j\mathbf{q})\mathbf{e}_\alpha(\mathbf{b}|j'\mathbf{q}) = \delta_{jj'}, \tag{2.21}$$

$$\sum_{j} e^*_\beta(\mathbf{b}'|j\mathbf{q})e_\alpha(\mathbf{b}|j\mathbf{q}) = \delta_{\alpha\beta}\delta_{jj'}, \tag{2.22}$$

Equation (2.16) can be rewritten with respect to the frequency $\omega(j\mathbf{q})$ and the polarisation vector $\mathbf{e}_\alpha(\mathbf{b}|j\mathbf{q})$,

$$\omega^2(j\mathbf{q})\mathbf{e}_\alpha(\mathbf{b}|j\mathbf{q}) = \sum_{\mathbf{b}'\beta} D_{\alpha\beta}(\mathbf{b}\mathbf{b}'|\mathbf{q})\mathbf{e}_\beta(\mathbf{b}'|j\mathbf{q}). \tag{2.23}$$

From the orthonormality condition (2.21) and closure condition (2.22), the eigenvalues of equation (2.23) are decoupled and do not interact with each other. Solving this equation yields the phonon dispersion $\omega(j\mathbf{q})$.

2.2.4 Dispersion Relation

The phonon dispersion relation is now given as $\omega(j\mathbf{q})$, where $j\mathbf{q}$ represents the *normal modes* of vibrations. One have $3n$ normal modes in a system with n atoms. The modes

are "normal" in the sense that they are decoupled and an excitation of one normal mode will not cause any motion of a different mode, i.e. there is no energy transfer between modes.

In the special case when $\mathbf{q} \to 0$, three of the solutions of $\omega(j\mathbf{q})$ goes to zero. Those modes are called *acoustic modes* or *acoustic phonons*. A proof of this is given in reference [44]. The remaining $3n-3$ modes are called the *optical phonons*. The acoustic phonons are long wavelength vibrations with coherent movement of atoms in the direction $\alpha = 1, 2, 3$. In contrast, optical phonons have short wavelength with out-of-phase movements of the atoms in the lattice, and they will only occur if the system is composed of atoms with different charge or mass [39].

Any vibrational motion corresponding to any of the branches can have their motion longitudinal or transverse to the wave vector, i.e. $\mathbf{e}||\mathbf{q}$ or $\mathbf{e} \perp \mathbf{q}$. It is also possible to have a mixture of these motions. In an isotropic crystal, the polarisation vector can be written as mutually independent polarisations of a given wave vector $\mathbf{q}$,

$$\mathbf{e}_{\mathrm{L}}||\mathbf{q}; \quad \mathbf{e}_{\mathrm{T}_1} \perp \mathbf{e}_{\mathrm{T}_2} \perp \mathbf{q}, \tag{2.24}$$

where $\mathbf{e}_{\mathrm{L}}$ is the longitudinal vibrations. $\mathbf{e}_{\mathrm{T}_1}$ and $\mathbf{e}_{\mathrm{T}_2}$ is the transverse vibrations with a degeneration of the eigenvalues. However, if one considers a cubic system, purely longitudinal and transverse modes occur only along high symmetry points. In the case of the FCC half-Heusler structure, these pure modes occur when the wave vector $\mathbf{q}$ is along the $[100]$, $[110]$ and $[111]$ directions, corresponding to $\Gamma \to \mathrm{X}$, $\Gamma \to \mathrm{K}$ and $\Gamma \to \mathrm{L}$ points, respectively.

The phonon modes of TiNiSn are illustrated in figure 2.3. There are three distinct atoms in TiNiSn; thus, from the definition of phonon branches $j = 3n$, one expect in total nine phonon branches, and all nine phonon branches are observed in figure 2.3. The lower three branches are the acoustic phonons and the six upper branches are the optical phonons. Going from zero frequency and upwards we get the three acoustic branches: the first two are the transverse acoustic (TA) branches and the third is the longitudinal acoustic (LA) branch, denoted $\mathrm{T}_1\mathrm{A}$, $\mathrm{T}_2\mathrm{A}$ and LA. The next three branches are optical branches: there are two transverse optic (TO) branches and one longitudinal optic (LO) branch denoted $\mathrm{T}_1\mathrm{O}$, $\mathrm{T}_2\mathrm{O}$, LO. The last three are also optical branches: $\mathrm{T}_1\mathrm{O}'$, $\mathrm{T}_2\mathrm{O}'$ and LO'. Noteworthy, the transverse modes are degenerated only along the directions $[100]$ and $[111]$, but not along $[110]$.

A non-analytic correction term can be included to account for the induced macroscopic polarization from the LO motion of TO branch [45]. This is seen as a LO-TO splitting at the zone center for the higher energetic optical phonon branches.

The slope of the phonon dispersion is related to the group velocity in the following

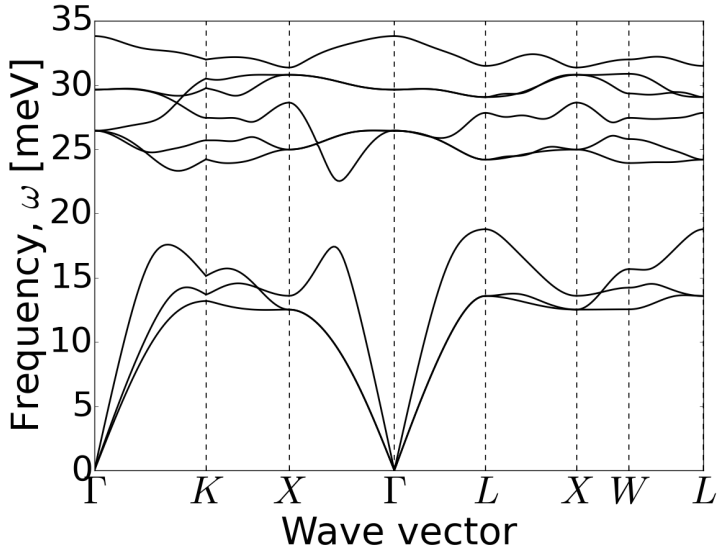

Figure 2.3: Phonon dispersion of TiNiSn

manner,

$$v_{j\mathbf{q}} = \frac{\partial \omega(j\mathbf{q})}{\partial \mathbf{q}}, \tag{2.25}$$

which is the change in frequency with respect to the reciprocal space of the phonons. The acoustic phonons have steeper slopes resulting in a higher group velocity compared to the optical modes.

2.3 Hamiltonian for a Three Dimensional Crystal

2.3.1 Introducing Quantum Mechanics

This section will describe vibrational motions in the Hamiltonian formalism. We start by adding the potential energy expanded up to the third-order to the Hamiltonian for kinetic energy,

$$\begin{aligned}\hat{H} = &\sum_{\mathbf{lb}} \frac{\mathbf{p(lb)p(lb)}}{2m_b} + \frac{1}{2}\sum_{lb,l'b'}\sum_{\alpha\beta}\phi_{\alpha\beta}(\mathbf{lb},\mathbf{l'b'})u_\alpha(\mathbf{lb})u_\beta(\mathbf{l'b'}) \\ &+ \frac{1}{3!}\sum_{lb,l'b',l''b''}\sum_{\alpha\beta\gamma}\phi_{\alpha\beta\gamma}(\mathbf{lb},\mathbf{l'b'},\mathbf{l''b''})u_\alpha(\mathbf{lb})u_\beta(\mathbf{l'b'})u_\gamma(\mathbf{l''b''}).\end{aligned} \tag{2.26}$$

The first term is the kinetic energy, the constant V_0 from the Taylor series is set to zero for convenience and $\mathbf{p}(\mathbf{lb})$ denotes the momentum operator for an atom with position $\mathbf{b}$ in a unit cell $\mathbf{l}$ with mass m_b. The first step consists of a Fourier transformation of coordinate $\mathbf{u}(\mathbf{lb})$ and momentum $\mathbf{p}(\mathbf{lb})$,

$$\mathbf{u}(\mathbf{lb}) = \frac{1}{\sqrt{N_0\Omega}} \sum_{\mathbf{q}} \mathbf{X}(\mathbf{qb}) \mathrm{e}^{\mathrm{i}\mathbf{q}\cdot\mathbf{l}}, \tag{2.27}$$

$$\mathbf{p}(\mathbf{lb}) = \frac{1}{\sqrt{N_0\Omega}} \sum_{\mathbf{q}} \mathbf{P}(\mathbf{qb}) \mathrm{e}^{-\mathrm{i}\mathbf{q}\cdot\mathbf{l}}. \tag{2.28}$$

$N_0 = N_1 N_2 N_3$ is the total number of unit cells and Ω is the volume of one unit cell; therefore, $N_0\Omega$ is the total volume of the crystal. We call $\mathbf{X}$ and $\mathbf{P}$ the *normal coordinate* of the variables $\mathbf{u}$ and $\mathbf{p}$, respectively, which are functions of the wave vector $\mathbf{q}$. The wave vector can be described as a collective coordinate; that is, the normal coordinates can describe the collective displacements of atoms and the corresponding lattice momentum for a traveling wave with a given $\mathbf{q}$ extending over all unit cells.

The normal coordinates satisfy the following commutation relations:

$$\begin{aligned}
[\mathbf{X}(\mathbf{qb}), \mathbf{P}(\mathbf{q'b'})] &= \frac{1}{N_0\Omega} \sum_{\mathbf{l},\mathbf{l'}} \mathrm{e}^{-\mathrm{i}(\mathbf{q}\cdot\mathbf{l}-\mathbf{q'}\cdot\mathbf{l'})} [\mathbf{u}(\mathbf{lb}), \mathbf{p}(\mathbf{l'b'})] \\
&= \frac{1}{N_0\Omega} \sum_{\mathbf{l},\mathbf{l'}} \mathrm{e}^{-\mathrm{i}(\mathbf{q}\cdot\mathbf{l}-\mathbf{q'}\cdot\mathbf{l'})} \hat{\mathbf{I}} \mathrm{i}\hbar \delta_{\mathbf{ll'}} \delta_{\mathbf{bb'}} \\
&= \hat{\mathbf{I}} \mathrm{i}\hbar \delta_{\mathbf{qq'}} \delta_{\mathbf{bb'}},
\end{aligned} \tag{2.29}$$

where $[\mathbf{u}(\mathbf{lb}), \mathbf{p}(\mathbf{l'b'})] = \hat{\mathbf{I}} \mathrm{i}\hbar \delta_{\mathbf{ll'}} \delta_{\mathbf{bb'}}$. $\delta_{\mathbf{qq'}}$ is the Fourier transform of $\delta_{\mathbf{ll'}}$. The normal coordinates are canonically conjugate only if they exhibit the same wave vector $\mathbf{q}$ and basis vector $\mathbf{b}$. Because the operators $\mathbf{u}$ and $\mathbf{p}$ are Hermitian, the normal coordinate operators $\mathbf{X}$ and $\mathbf{P}$ are non-Hermitian. It can be expressed as

$$\mathbf{X}^\dagger(\mathbf{qb}) = \mathbf{X}(-\mathbf{qb}) = \frac{1}{\sqrt{N_0\Omega}} \sum_{\mathbf{l}} \mathbf{u}(\mathbf{lb}) \mathrm{e}^{\mathrm{i}\mathbf{q}\cdot\mathbf{l}}, \tag{2.30}$$

$$\mathbf{P}^\dagger(\mathbf{qb}) = \mathbf{P}(-\mathbf{qb}) = \frac{1}{\sqrt{N_0\Omega}} \sum_{\mathbf{l}} \mathbf{p}(\mathbf{lb}) \mathrm{e}^{-\mathrm{i}\mathbf{q}\cdot\mathbf{l}}. \tag{2.31}$$

The Hamiltonian from equation (2.26) can be rewritten with the help of the normal

coordinate operators from equation (2.27) and (2.28),

$$\begin{aligned}\hat{H} =& \frac{1}{N_0\Omega}\sum_{\mathbf{qq'lb}}\frac{\mathbf{P(qb)}\cdot\mathbf{P(q'b)}}{2m_b}\mathrm{e}^{-\mathrm{i}(\mathbf{q}+\mathbf{q}')\cdot\mathbf{l}} \\ &+\frac{1}{2}\frac{1}{N_0\Omega}\sum_{\mathbf{qq'},\mathbf{lb},\mathbf{l'b'}}\sum_{\alpha\beta}\phi_{\alpha\beta}(\mathbf{lb},\mathbf{l'b'})X_\alpha(\mathbf{qb})X_\beta(\mathbf{q'b'})\mathrm{e}^{\mathrm{i}(\mathbf{q}+\mathbf{q}')\cdot\mathbf{l}} \\ &+\frac{1}{3!}\frac{1}{(N_0\Omega)^{3/2}}\sum_{\substack{\mathbf{qq'q''},\\ \mathbf{lb},\mathbf{l'b'},\mathbf{l''b''}}}\sum_{\alpha\beta\gamma}\phi_{\alpha\beta\gamma}(\mathbf{lb},\mathbf{l'b'},\mathbf{l''b''}) \\ &\times X_\alpha(\mathbf{lb})X_\beta(\mathbf{l'b'})X_\gamma(\mathbf{l''b''})\mathrm{e}^{\mathrm{i}(\mathbf{q}\cdot\mathbf{l}+\mathbf{q}'\cdot\mathbf{l}'+\mathbf{q}''\cdot\mathbf{l}'')}.\end{aligned} \tag{2.32}$$

This equation can be simplified. Firstly, by performing the summation over $\mathbf{l}$ for the kinetic energy operator,

$$\begin{aligned}\hat{K} &= \sum_{\mathbf{qq'b}}\frac{\mathbf{P(qb)}\cdot\mathbf{P(q'b)}}{2m_b}\frac{1}{N_0\Omega}\sum_{\mathbf{l}}\mathrm{e}^{-\mathrm{i}(\mathbf{q}+\mathbf{q}')\cdot\mathbf{l}} \\ &= \sum_{\mathbf{qq'b}}\frac{\mathbf{P(qb)}\cdot\mathbf{P(q'b)}}{2m_b}\delta_{\mathbf{q}+\mathbf{q}',0} \\ &= \sum_{\mathbf{qb}}\frac{\mathbf{P(qb)}\cdot\mathbf{P}^\dagger\mathbf{(qb)}}{2m_b},\end{aligned} \tag{2.33}$$

where we have used $\sum_{\mathbf{l}}\mathrm{e}^{-\mathrm{i}(\mathbf{q}+\mathbf{q}')\cdot\mathbf{l}} = N_0\Omega\delta_{\mathbf{q}+\mathbf{q}',0}$ and equation (2.31) where $\mathbf{q} = -\mathbf{q}'$.

Before simplifying the term containing the second-order forces, we define it as following [37]:

$$\phi_{\alpha\beta}(\mathbf{bb'}|\mathbf{q}) = \sqrt{m_b m_{b'}}D_{\alpha\beta}(\mathbf{bb'}|-\mathbf{q}) = \sum_{\mathbf{h'}}\phi_{\alpha\beta}(\mathbf{0b},\mathbf{h'b'})\mathrm{e}^{-\mathrm{i}\mathbf{q}\cdot\mathbf{h'}}. \tag{2.34}$$

The translation symmetry condition from equation (2.13) was used, and we defined the relative cell index $\mathbf{l'} - \mathbf{l} = \mathbf{h'}$. The second term in equation (2.32) is the second-order potential energy operator and can be simplified by using the newly defined term for the second-order force constants $\phi_{\alpha\beta}(\mathbf{bb'}|\mathbf{q})$ from equation (2.34),

$$\begin{aligned}\hat{V}_2 &= \frac{1}{2}\sum_{\mathbf{qq'h'bb'}}\sum_{\alpha\beta}\phi_{\alpha\beta}(\mathbf{0b},\mathbf{h'b'})X_\alpha(\mathbf{qb})X_\beta(\mathbf{q'b'})\mathrm{e}^{\mathrm{i}\mathbf{q}\cdot\mathbf{h'}} \\ &= \frac{1}{2}\sum_{\mathbf{qbb'}}\sum_{\alpha\beta}\phi_{\alpha\beta}(\mathbf{bb'}|\mathbf{q})X_\alpha(\mathbf{qb})X^\dagger_\beta(\mathbf{qb'}).\end{aligned} \tag{2.35}$$

Before starting on the process to simplify the third term we make a new variable $\mathbf{h}'' = \mathbf{l}'' - \mathbf{l}$ and define the third-order forces as

$$\phi_{\alpha\beta\gamma}(\mathbf{qb}, \mathbf{q}'\mathbf{b}', \mathbf{q}''\mathbf{b}'') \equiv \sum_{\mathbf{h}'\mathbf{h}''} \phi_{\alpha\beta\gamma}(0\mathbf{b}, \mathbf{h}'\mathbf{b}', \mathbf{h}''\mathbf{b}'') \mathrm{e}^{\mathrm{i}\mathbf{q}'\cdot\mathbf{h}'} \mathrm{e}^{\mathrm{i}\mathbf{q}''\cdot\mathbf{h}''}. \tag{2.36}$$

Combining the third term of equation (2.32) and equation (2.36) one get the third-order potential energy operator,

$$\begin{aligned} \hat{V}_3 = &\frac{1}{3!} \frac{1}{(N_0\Omega)^{3/2}} \sum_{\mathbf{qb},\mathbf{q}'\mathbf{b}',\mathbf{q}''\mathbf{b}''} \sum_{\alpha\beta\gamma} \sum_{\mathbf{l}} \mathrm{e}^{\mathrm{i}(\mathbf{q}+\mathbf{q}'+\mathbf{q}'')\cdot\mathbf{l}} \\ &\times \phi_{\alpha\beta\gamma}(\mathbf{qb}, \mathbf{q}'\mathbf{b}', \mathbf{q}''\mathbf{b}'') X_\alpha(\mathbf{qb}) X_\beta(\mathbf{q}'\mathbf{b}') X_\gamma(\mathbf{q}''\mathbf{b}'') \\ = &\frac{1}{3!} \frac{1}{\sqrt{N_0\Omega}} \sum_{\mathbf{qb},\mathbf{q}'\mathbf{b}',\mathbf{q}''\mathbf{b}''} \delta_{\mathbf{G},\mathbf{q}+\mathbf{q}'+\mathbf{q}''} \sum_{\alpha\beta\gamma} \\ &\times \phi_{\alpha\beta\gamma}(\mathbf{qb}, \mathbf{q}'\mathbf{b}', \mathbf{q}''\mathbf{b}'') X_\alpha(\mathbf{qb}) X_\beta(\mathbf{q}'\mathbf{b}') X_\gamma(\mathbf{q}''\mathbf{b}''). \end{aligned} \tag{2.37}$$

The last step is the summation over $\mathbf{l}$ and the vector $\mathbf{G}$ is the reciprocal lattice vector.

Once again, the Hamiltonian can be rewritten, now with the help of the new operators: the kinetic energy operator (2.33), the second-order potential energy operator (2.35) and the third-order potential energy operator (2.37),

$$\begin{aligned} \hat{H} = &\sum_{\mathbf{qb}} \frac{\mathbf{P}(\mathbf{qb}) \cdot \mathbf{P}^\dagger(\mathbf{qb})}{2m_b} + \frac{1}{2} \sum_{\mathbf{qbb}'} \sum_{\alpha\beta} \phi_{\alpha\beta}(\mathbf{bb}'|\mathbf{q}) X_\alpha(\mathbf{qb}) X^\dagger_\beta(\mathbf{qb}') \\ &+ \frac{1}{3!} \frac{1}{\sqrt{N_0\Omega}} \sum_{\mathbf{qb},\mathbf{q}'\mathbf{b}',\mathbf{q}''\mathbf{b}''} \delta_{\mathbf{G},\mathbf{q}+\mathbf{q}'+\mathbf{q}''} \sum_{\alpha\beta\gamma} \\ &\times \phi_{\alpha\beta\gamma}(\mathbf{qb}, \mathbf{q}'\mathbf{b}', \mathbf{q}''\mathbf{b}'') X_\alpha(\mathbf{qb}) X_\beta(\mathbf{q}'\mathbf{b}') X_\gamma(\mathbf{q}''\mathbf{b}''). \end{aligned} \tag{2.38}$$

The Hamiltonian in equation (2.38) is expressed in terms of the first quantisation variables of positions $\mathbf{X}(\mathbf{qb})$ and momenta $\mathbf{P}(\mathbf{qb})$ with a total of nN_0 atoms, which are coupled by the second-order force constants $\phi_{\alpha\beta}(\mathbf{bb}'|\mathbf{q})$ and third-order force constants $\phi_{\alpha\beta\gamma}(\mathbf{qb}, \mathbf{q}'\mathbf{b}', \mathbf{q}''\mathbf{b}'')$.

2.3.2 The Annihilation- and Creation Operators

This section will further work on the Hamiltonian to introduce the second quantisation variable; the procedure is often called the *second quantisation method*. The normal coordinates $\mathbf{X}(\mathbf{qb})$ and $\mathbf{P}(\mathbf{qb})$ can be transformed such that they depend on the vibrational mode $j\mathbf{q}$. We make use of the polarisation vector and write a new set of normal

coordinates as

$$X(j\mathbf{q}) = \sum_{\mathbf{b}} \sqrt{m_b}\mathbf{e}^*(\mathbf{b}|j\mathbf{q}) \cdot \mathbf{X}(\mathbf{qb}), \tag{2.39}$$

$$P(j\mathbf{q}) = \sum_{\mathbf{b}} \frac{1}{\sqrt{m_b}}\mathbf{e}(\mathbf{b}|j\mathbf{q}) \cdot \mathbf{P}(\mathbf{qb}). \tag{2.40}$$

We define the phonon annihilation operator $a_{j\mathbf{q}}$ and the creation operator $a^\dagger_{j\mathbf{q}}$ [37],

$$a_{j\mathbf{q}} = \frac{1}{\sqrt{2\hbar\omega(j\mathbf{q})}} P(j\mathbf{q}) - \mathrm{i}\sqrt{\frac{\omega(j\mathbf{q})}{2\hbar}} X^\dagger(j\mathbf{q}), \tag{2.41}$$

$$a^\dagger_{j\mathbf{q}} = \frac{1}{\sqrt{2\hbar\omega(j\mathbf{q})}} P^\dagger(j\mathbf{q}) + \mathrm{i}\sqrt{\frac{\omega(j\mathbf{q})}{2\hbar}} X(j\mathbf{q}). \tag{2.42}$$

The annihilation operator $a_{j\mathbf{q}}$ and creation operator $a^\dagger_{j\mathbf{q}}$ obey the following commutation relation:

$$[a_{j\mathbf{q}}, a^\dagger_{j'\mathbf{q}'}] = \hat{\mathbf{I}}\delta_{\mathbf{qq}'}\delta_{jj'}. \tag{2.43}$$

The normal coordinates can be expressed as functions of the annihilation- and creation operators. This is done by solving the annihilation- and creation operator from equation (2.41) and (2.42) for $X(j\mathbf{q})$ and $P(j\mathbf{q})$,

$$X(j\mathbf{q}) = -\mathrm{i}\sqrt{\frac{\hbar}{2\omega(j\mathbf{q})}}(a^\dagger_{j\mathbf{q}} - a_{-j\mathbf{q}}), \tag{2.44}$$

$$P(j\mathbf{q}) = \sqrt{\frac{\hbar\omega(j\mathbf{q})}{2}}(a_{j\mathbf{q}} + a^\dagger_{-j\mathbf{q}}), \tag{2.45}$$

where $X^\dagger(j\mathbf{q}) = X(-j\mathbf{q})$ and $P^\dagger(j\mathbf{q}) = P(-j\mathbf{q})$ because they are non-Hermitian. Also, a traveling wave with a wave vector of the same magnitude in different directions will have the same frequency $\omega(j\mathbf{q}) = \omega(-j\mathbf{q})$.

One can express the normal coordinates $\mathbf{X}(\mathbf{qb})$ and $\mathbf{P}(\mathbf{qb})$ as functions of the polarisation vector and annihilation- and creation operators. We start by inserting the normal coordinates as a function of the phonon mode $j\mathbf{q}$ and polarisation vectors from equation (2.39) and (2.40) into the equation (2.44) and (2.45), then solve for $\mathbf{X}(\mathbf{qb})$ and $\mathbf{P}(\mathbf{qb})$,

$$\mathbf{X}(\mathbf{qb}) = -\mathrm{i}\sum_j \sqrt{\frac{\hbar}{2m_b\omega(j\mathbf{q})}}\mathbf{e}(\mathbf{b}|j\mathbf{q})(a^\dagger_{j\mathbf{q}} - a_{-j\mathbf{q}}), \tag{2.46}$$

$$\mathbf{P}(\mathbf{qb}) = \sum_j \sqrt{\frac{m_b \hbar \omega(j\mathbf{q})}{2}} \mathbf{e}^*(\mathbf{b}|j\mathbf{q})(a_{j\mathbf{q}} + a^\dagger_{-j\mathbf{q}}). \tag{2.47}$$

The kinetic energy operator from equation (2.33) can now be written in terms of the annihilation- and creation operators with the use of the orthonormality condition (2.21) and the momenta operator given in equation (2.47),

$$\begin{aligned}
\hat{K} &= \sum_{\mathbf{qb}} \frac{\mathbf{P}(\mathbf{qb}) \cdot \mathbf{P}^\dagger(\mathbf{qb})}{2m_b} \\
&= \frac{1}{4} \sum_{j\mathbf{q}} \hbar\omega(j\mathbf{q}) \mathbf{e}^*(\mathbf{b}|j\mathbf{q}) \mathbf{e}(\mathbf{b}|j\mathbf{q})(a_{j\mathbf{q}} + a^\dagger_{-j\mathbf{q}})(a^\dagger_{j\mathbf{q}} + a_{-j\mathbf{q}}) \\
&= \frac{1}{4} \sum_{j\mathbf{q}} \hbar\omega(j\mathbf{q})(a_{j\mathbf{q}} + a^\dagger_{-j\mathbf{q}})(a^\dagger_{j\mathbf{q}} + a_{-j\mathbf{q}}).
\end{aligned} \tag{2.48}$$

Similarly, the second-order potential energy operator can be expressed in terms of the annihilation- and creation operators. This derivation will make use of the orthonormality condition (2.21), eigenvalue equation (2.23), second-order force constants in equation (2.34) and the new normal coordinates in the equations (2.46) and (2.47),

$$\begin{aligned}
\hat{V}_2 &= \frac{1}{2} \sum_{\mathbf{qbb'}} \sum_{\alpha\beta} \phi_{\alpha\beta}(\mathbf{bb'}|\mathbf{q}) X_\alpha(\mathbf{qb}) X^\dagger_\beta(\mathbf{qb'}) \\
&= \frac{1}{4} \sum_{j\mathbf{qb}\alpha} \frac{\hbar}{2\omega(j\mathbf{q})} \left[\sum_{\mathbf{b'}\beta} D^*_{\alpha\beta}(\mathbf{bb'}|\mathbf{q}) \mathbf{e}^*_\beta(\mathbf{b'}|j\mathbf{q}) \right] \mathbf{e}_\alpha(\mathbf{b}|j\mathbf{q}) \\
&\quad \times (a^\dagger_{j\mathbf{q}} - a_{-j\mathbf{q}})(a_{j\mathbf{q}} - a^\dagger_{-j\mathbf{q}}) \\
&= \frac{1}{4} \sum_{j\mathbf{qb}} \hbar\omega(j\mathbf{q}) \left[\sum_\alpha \mathbf{e}^*_\alpha(\mathbf{b}|j\mathbf{q}) e_\alpha(\mathbf{b}|j\mathbf{q}) \right] (a^\dagger_{j\mathbf{q}} - a_{-j\mathbf{q}})(a_{j\mathbf{q}} - a^\dagger_{-j\mathbf{q}}) \\
&= \frac{1}{4} \sum_{j\mathbf{qb}} \hbar\omega(j\mathbf{q})(a^\dagger_{j\mathbf{q}} - a_{-j\mathbf{q}})(a_{j\mathbf{q}} - a^\dagger_{-j\mathbf{q}}).
\end{aligned} \tag{2.49}$$

The relations $D_{\alpha\beta}(\mathbf{bb'}|-\mathbf{q}) = D^*_{\alpha\beta}(\mathbf{bb'}|\mathbf{q})$ and $\omega(j\mathbf{q})^2 = \omega(-j\mathbf{q})^2$ have been used. Adding up the operator $\hat{K}$ and $\hat{V}_2$, one obtain the Hamiltonian for the harmonic approx-

imation,

$$\begin{aligned} H_{\text{harm}} &= \frac{1}{4}\sum_{j\mathbf{q}\mathbf{b}} \hbar\omega(j\mathbf{q}) \left[(a_{j\mathbf{q}} + a^\dagger_{-j\mathbf{q}})(a^\dagger_{j\mathbf{q}} + a_{-j\mathbf{q}}) + (a^\dagger_{j\mathbf{q}} - a_{-j\mathbf{q}})(a_{j\mathbf{q}} - a^\dagger_{-j\mathbf{q}})\right] \\ &= \frac{1}{2}\sum_{j\mathbf{q}} \hbar\omega(j\mathbf{q})(a_{j\mathbf{q}}a^\dagger_{j\mathbf{q}} + a^\dagger_{j\mathbf{q}}a_{j\mathbf{q}}). \end{aligned} \tag{2.50}$$

The summation over all negative wave vectors is just a duplicate of the summation over all positive wave vectors. Using the commutation relation between the annihilation- and creation operators from equation (2.43), the final form of the harmonic Hamiltonian is

$$H_{\text{harm}} = \sum_{j\mathbf{q}} \hbar\omega(j\mathbf{q})(a^\dagger_{j\mathbf{q}}a_{j\mathbf{q}} + \frac{1}{2}). \tag{2.51}$$

Expressing the anharmonic potential energy operator is done in a similar manner. We will simply substitute the normal coordinate $\mathbf{X}(\mathbf{qb})$ in equation (2.37) with the normal coordinate from equation (2.47),

$$\begin{aligned} \hat{V}_3 = \frac{1}{3!}\frac{i}{\sqrt{N_0}} &\sum_{\substack{\mathbf{qb},\mathbf{q'b'},\mathbf{q''b''} \\ jj'j''}} \sum_{\alpha\beta\gamma} \left(\frac{\hbar^3}{8m_b m_{b'} m_{b''}\omega(j\mathbf{q})\omega(j'\mathbf{q'})\omega(j''\mathbf{q''})}\right)^{1/2} \\ &\times \delta_{\mathbf{G},\mathbf{q}+\mathbf{q'}+\mathbf{q''}}\phi_{\alpha\beta\gamma}(\mathbf{qb},\mathbf{q'b'},\mathbf{q''b''})\mathbf{e}_\alpha(\mathbf{b}|j\mathbf{q})\mathbf{e}_\beta(\mathbf{b'}|j'\mathbf{q'})\mathbf{e}_\gamma(\mathbf{b''}|j''\mathbf{q''}) \\ &\times (a^\dagger_{j\mathbf{q}} - a_{-j\mathbf{q}})(a^\dagger_{j'\mathbf{q'}} - a_{-j'\mathbf{q'}})(a^\dagger_{j''\mathbf{q''}} - a_{-j''\mathbf{q''}}) \\ = \frac{1}{3!} &\sum_{j\mathbf{q},j'\mathbf{q'},j''\mathbf{q''}} \delta_{\mathbf{G},\mathbf{q}+\mathbf{q'}+\mathbf{q''}}\phi(j\mathbf{q},j'\mathbf{q'},j''\mathbf{q''}) \\ &\times (a^\dagger_{j\mathbf{q}} - a_{-j\mathbf{q}})(a^\dagger_{j'\mathbf{q'}} - a_{-j'\mathbf{q'}})(a^\dagger_{j''\mathbf{q''}} - a_{-j''\mathbf{q''}}). \end{aligned} \tag{2.52}$$

In the last step, the factor $\phi(j\mathbf{q}, j'\mathbf{q'}, j''\mathbf{q''})$ was introduced and it is given as

$$\begin{aligned} \phi(j\mathbf{q}, j'\mathbf{q'}, j''\mathbf{q''}) = &\frac{\mathrm{i}}{\sqrt{N_0}} \sum_{\mathbf{bb'b''}} \sum_{\alpha\beta\gamma} \left(\frac{\hbar^3}{8m_b m_{b'} m_{b''}\omega(j\mathbf{q})\omega(j'\mathbf{q'})\omega(j''\mathbf{q''})}\right)^{1/2} \\ &\times \phi_{\alpha\beta\gamma}(\mathbf{qb},\mathbf{q'b'},\mathbf{q''b''}) \\ &\times \mathbf{e}_\alpha(\mathbf{b}|j\mathbf{q})\mathbf{e}_\beta(\mathbf{b'}|j'\mathbf{q'})\mathbf{e}_\gamma(\mathbf{b''}|j''\mathbf{q''}), \end{aligned} \tag{2.53}$$

which is called the cubic term of the anharmonic potential energy operator. The Kronecker's delta $\delta_{\mathbf{G},\mathbf{q}+\mathbf{q'}+\mathbf{q''}}$ is due to translation invariance; the phonon wave vectors $\mathbf{q}$, $\mathbf{q'}$

and $\mathbf{q}''$ in equation (2.52) must satisfy conservation of momentum,

$$\mathbf{q} + \mathbf{q}' + \mathbf{q}'' = \mathbf{G}, \tag{2.54}$$

where $\mathbf{G}$ is the reciprocal lattice vector.

The second quantisation of the Hamiltonian up to the third-order of the potential energy is complete. To recapitulate: we introduced the quantum mechanical formalism where we defined the normal coordinates of positions and momenta as a function of the wave vector $\mathbf{q}$. Further, we introduced the second quantisation variables $a_{j\mathbf{q}}$ and $a^{\dagger}_{j\mathbf{q}}$ to the Hamiltonian by expressing a new set of normal coordinates as functions of the annihilation- and creation operators Now, we have the tools to express the quantisation of energy levels of phonons.

2.4 Harmonic Properties in a Crystal

2.4.1 Density of States

Density of states (DOS) of normal modes is defined as the number of modes between frequency ω and $\omega + \mathrm{d}\omega$. If the dispersion relation is known, a general expression for DOS can be derived with the use of periodic boundary conditions. It can be shown that only one $\mathbf{q}$-point in the reciprocal space is confined to a volume $(2\pi/L)^3$ [41, 42]. In other words, a unit volume in reciprocal space contains $(2\pi/L)^3 = N_0\Omega/8\pi^3$ values of $\mathbf{q}$.

Density of states must be evaluated over the reciprocal space, and the evaluation can be expressed as a Dirac delta function [37]. The expression for DOS is given as

$$g(\omega(j\mathbf{q})) = \frac{N_0\Omega}{8\pi^3} \sum_{j\mathbf{q}} \delta(\omega - \omega(j\mathbf{q})). \tag{2.55}$$

An accurate DOS is obtained by summing over a large number of $\mathbf{q}$-points; however, one does only need to consider the irreducible part of the first Brillouin zone as described in the section 2.1.3 about Brillouin zone.

2.4.2 Thermodynamics

The harmonic phonon energy can be obtained by applying the harmonic Hamiltonian on a phonon state $|n_{j\mathbf{q}}\rangle$ in phonon mode $j\mathbf{q}$,

$$H_{\text{harm}}|n_{j\mathbf{q}}\rangle = \sum_{j\mathbf{q}} \hbar\omega(j\mathbf{q})(n_{j\mathbf{q}} + \frac{1}{2})|n_{j\mathbf{q}}\rangle. \tag{2.56}$$

The operator $a^{\dagger}_{j\mathbf{q}}a_{j\mathbf{q}}|n_{j\mathbf{q}}\rangle = n_{j\mathbf{q}}|n_{j\mathbf{q}}\rangle$, where $n_{j\mathbf{q}}$ is the phonon occupation number. It is given by the Bose-Einstein distribution function,

$$n_{j\mathbf{q}} = \frac{1}{\mathrm{e}^{\hbar\omega(j\mathbf{q})/k_{\text{B}}T} - 1}, \tag{2.57}$$

which is derived from statistical thermodynamics.

The eigenvalues of equation (2.56) is the harmonic phonon energy,

$$E = \sum_{j\mathbf{q}} \hbar\omega(j\mathbf{q}) \left(n_{j\mathbf{q}} + \frac{1}{2} \right) = \sum_{j\mathbf{q}} \hbar\omega(j\mathbf{q}) \left(\frac{1}{\mathrm{e}^{\hbar\omega(j\mathbf{q})/k_{\text{B}}T} - 1} + \frac{1}{2} \right). \tag{2.58}$$

Once the phonon energy is known, the heat capacity at constant volume is easily derived,

$$C_{\text{V}} = \left. \frac{\partial E_{j\mathbf{q}}}{\partial T} \right|_{\text{V}} = \sum_{j\mathbf{q}} k_{\text{B}} \left(\frac{\hbar\omega(j\mathbf{q})}{k_{\text{B}}T} \right)^2 \frac{\mathrm{e}^{\hbar\omega(j\mathbf{q})/k_{\text{B}}T)}}{(\mathrm{e}^{\hbar\omega(j\mathbf{q})/k_{\text{B}}T} - 1)^2}. \tag{2.59}$$

Other thermodynamic quantities can be calculated if one know the partition function Z for phonons. The derivation of the partition function can be found in reference [39], and is given as

$$Z = \mathrm{e}^{-V/k_{\text{B}}T} \prod_{j\mathbf{q}} \frac{\mathrm{e}^{-\hbar\omega(j\mathbf{q})/2k_{\text{B}}T}}{1 - \mathrm{e}^{-\hbar\omega(j\mathbf{q})/k_{\text{B}}T}}. \tag{2.60}$$

The vibrational contribution to the free energy is then,

$$F_{\text{vib}} = -k_{\text{B}}T \ln(Z) = V - \frac{1}{2} \sum_{\mathbf{q}} \hbar\omega(j\mathbf{q}) + k_{\text{B}}T \sum_{j\mathbf{q}} \ln(1 - \mathrm{e}^{-\hbar\omega(j\mathbf{q})/k_{\text{B}}T}). \tag{2.61}$$

Once the vibrational free energy is known, the vibrational entropy is given as

$$\begin{aligned} S_{\text{vib}} &= -\frac{\partial F_{\text{vib}}}{\partial T} \\ &= \frac{1}{2T}\sum_{j\mathbf{q}} \hbar\omega(j\mathbf{q}) \coth(\hbar\omega(j\mathbf{q})2k_{\text{B}}T) - k_{\text{B}}\sum_{j\mathbf{q}} \ln(2\sinh(\hbar\omega(j\mathbf{q})/2k_{\text{B}}T)). \end{aligned} \tag{2.62}$$

2.5 Thermal Conductivity

2.5.1 Boltzmann Transport Equation

In perfect and harmonic crystals, there are no interactions between the phonon modes resulting in an infinite heat conduction. However, in real crystals there will be interactions between phonons and the heat conduction will have a finite value. The lattice thermal conductivity can be described through the Boltzmann transport equation (BTE) for phonons. The BTE assumes that the occupation number of a phonon mode $j\mathbf{q}$ can be described by its distribution function $n_{j\mathbf{q}}(\mathbf{r}, t)$ in the vicinity of position $\mathbf{r}$ at a time t. The total rate of change of the occupation number when the system is placed in a thermal gradient can be expressed as

$$\frac{\partial n_{j\mathbf{q}}}{\partial t} = \left.\frac{\partial n_{j\mathbf{q}}}{\partial t}\right|_{\text{diffusion}} + \left.\frac{\partial n_{j\mathbf{q}}}{\partial t}\right|_{\text{scattering}}, \tag{2.63}$$

where one have contribution to the rate of change from diffusion and scattering mechanisms.

A thermal gradient ∇T will make the phonons diffuse with a rate

$$\left.\frac{\partial n_{j\mathbf{q}}}{\partial t}\right|_{\text{diffusion}} = -v_{j\mathbf{q}}\nabla T\frac{\partial n_{j\mathbf{q}}}{\partial T}, \tag{2.64}$$

where $v_{j\mathbf{q}}$ is the group velocity at phonon mode $j\mathbf{q}$.

One assumes a steady state where the total rate of change of the phonon distribution number must be equal to zero. In the steady state, the deviation from the average occupation number $\bar{n}_{j\mathbf{q}}$ with respect to the thermal gradient is small. Thus, one can replace $n_{j\mathbf{q}}$ with $\bar{n}_{j\mathbf{q}}$ and equation (2.63) can be rewritten as

$$-v_{j\mathbf{q}}\nabla T\frac{\partial \bar{n}_{j\mathbf{q}}}{\partial T} + \left.\frac{\partial n_{j\mathbf{q}}}{\partial t}\right|_{\text{scattering}} = 0. \tag{2.65}$$

The average occupation number is given by the Bose-Einstein distribution function as in equation (2.57).

The second term in equation (2.65) represents the rate of change due to scattering mechanisms, e.g. anharmonic effects, boundary scattering or mass-disorder scattering. To solve said equation, expressions for the scattering mechanisms have to be derived.

2.5.2 Relaxation Time Approximation

By introducing the relaxation time approximation (RTA), an expression for the lattice thermal conductivity can be derived from the phonon BTE. The relaxation time is denoted $\tau_{j\mathbf{q}}$ and represents the the amount of time a phonon in mode $j\mathbf{q}$ will travel before it gets annihilated due to scattering. The simplest picture uses the *single-mode* relaxation time, and in this approximation it is assumed that only one phonon mode at a time deviates from its equilibrium distribution while all other modes remain at equilibrium. The scattering term in equation (2.65) can be expressed as

$$-v_{j\mathbf{q}}\nabla T\frac{\partial \bar{n}_{j\mathbf{q}}}{\partial T} = -\left.\frac{\partial n_{j\mathbf{q}}}{\partial t}\right|_{\text{scattering}} = \frac{n_{j\mathbf{q}} - \bar{n}_{j\mathbf{q}}}{\tau_{j\mathbf{q}}}. \tag{2.66}$$

An expression for lattice thermal conductivity can be derived from Fourier's law of heat conduction. If a material is placed in a thermal gradient, the Fourier's law state that the heat flux $\mathbf{Q}$, resulting from heat conduction due to the temperature difference, is proportional to the thermal gradient times a proportional constant,

$$\mathbf{Q} = -\kappa_{\text{l}}\nabla T. \tag{2.67}$$

The proportional constant κ_{l} is the lattice contribution to the thermal conductivity.

The heat flux from phonons is given as [37]

$$\mathbf{Q} = \frac{1}{N_0\Omega}\sum_j \int_{\mathbf{q}} \hbar\omega(j\mathbf{q}) n_{j\mathbf{q}} v_{j\mathbf{q}}\,\mathrm{d}\mathbf{q}, \tag{2.68}$$

where the summation is done to obtain the contribution to heat flux from all phonon branches, while the integral gathers the contribution over the reciprocal space. Substi-

tuting equation (2.66) into (2.68) we get,

$$\begin{aligned}\mathbf{Q} &= -\frac{1}{N_0\Omega}\sum_j \int_{\mathbf{q}} \left(\tau_{j\mathbf{q}} v_{j\mathbf{q}}^2 \hbar\omega(j\mathbf{q}) \frac{\partial \bar{n}_{j\mathbf{q}}}{\partial T}\nabla T - \hbar\omega(j\mathbf{q})\bar{n}_{j\mathbf{q}} v_{j\mathbf{q}}\right) \mathrm{d}\mathbf{q} \\ &= -\frac{1}{N_0\Omega}\sum_j \int_{\mathbf{q}} \tau_{j\mathbf{q}} v_{j\mathbf{q}}^2 C_{\mathrm{V},j\mathbf{q}} \mathrm{d}\mathbf{q}\nabla T.\end{aligned} \tag{2.69}$$

The term $\sum_j \int_{\mathbf{q}} \hbar\omega(j\mathbf{q})\bar{n}_{j\mathbf{q}} v_{j\mathbf{q}}\,\mathrm{d}\mathbf{q} = 0$ because the average occupation number is isotropic. Multiplying $\hbar\omega(j\mathbf{q})$ with $\partial\bar{n}_{j\mathbf{q}}/\partial T$ results in the heat capacity under isochoric conditions. From Fourier's law in equation (2.67), one see that the proportionality constant κ_l can be extracted from equation (2.69),

$$\kappa_\mathrm{l} = \frac{1}{N_0\Omega}\sum_j \int_{\mathbf{q}} \tau_{j\mathbf{q}} v_{j\mathbf{q}}^2 C_{\mathrm{V},j\mathbf{q}}\,\mathrm{d}\mathbf{q}. \tag{2.70}$$

If the scattering mechanisms are independent of each other, the total relaxation time can be expressed by using Mathiessen's rule,

$$\frac{1}{\tau_{j\mathbf{q}}} = \frac{1}{\tau_{j\mathbf{q}}^{\mathrm{anh}}} + \frac{1}{\tau_{j\mathbf{q}}^{\mathrm{bs}}} + \frac{1}{\tau_{j\mathbf{q}}^{\mathrm{md}}} + \cdots, \tag{2.71}$$

where each relaxation time in this equation correspond to anharmonic scattering, boundary scattering and mass-disorder scattering, respectively. The next section will present the said scattering mechanisms and an expression of its relaxation times within the RTA.

2.6 Scattering Mechanisms

2.6.1 Anharmonic

Three-phonon Interactions

Anharmonicity introduces interactions between the normal modes. In the first-order perturbation, the potential energy operator up to the third-order causes three-phonon interactions. Expanding the product $(a_{j\mathbf{q}}^\dagger - a_{-j\mathbf{q}})(a_{j'\mathbf{q}'}^\dagger - a_{-j'\mathbf{q}'})(a_{j''\mathbf{q}''}^\dagger - a_{-j''\mathbf{q}''})$ from equation (2.52) one gets,

$$\begin{aligned}&a_{j\mathbf{q}}^\dagger a_{j'\mathbf{q}'}^\dagger a_{j''\mathbf{q}''}^\dagger - a_{j\mathbf{q}}^\dagger a_{j'\mathbf{q}'}^\dagger a_{-j''\mathbf{q}''} - a_{j\mathbf{q}}^\dagger a_{-j'\mathbf{q}'} a_{j''\mathbf{q}''}^\dagger \\ &+a_{j\mathbf{q}}^\dagger a_{-j'\mathbf{q}'} a_{-j''\mathbf{q}''} - a_{-j\mathbf{q}} a_{j'\mathbf{q}'}^\dagger a_{j''\mathbf{q}''}^\dagger + a_{-j\mathbf{q}} a_{j'\mathbf{q}'}^\dagger a_{-j''\mathbf{q}''} \\ &+a_{-j\mathbf{q}} a_{-j'\mathbf{q}'} a_{j''\mathbf{q}''}^\dagger - a_{-j\mathbf{q}} a_{-j'\mathbf{q}'} a_{-j''\mathbf{q}''}.\end{aligned} \tag{2.72}$$

The three-phonon interaction becomes clear, where each of these operators acts on a three-phonon state $|n_{j\mathbf{q}} n_{j'\mathbf{q}'} n_{j''\mathbf{q}''}\rangle$. There are four different interactions from equation (2.72): (i) creation of three phonons, (ii) annihilation of three phonons, (iii) creation of one and annihilation of two phonons and (iv) creation of two and annihilation of one phonon. Because of conservation of energy, the options (i) and (ii) are not physically relevant.

The interactions that are left can be expressed in terms of energy and momentum conservation:

$$\omega(j\mathbf{q}) + \omega(j'\mathbf{q}') = \omega(j''\mathbf{q}''); \quad \mathbf{q} + \mathbf{q}' = \mathbf{q}'', \tag{2.73}$$

$$\omega(j\mathbf{q}) = \omega(j'\mathbf{q}') + \omega(j''\mathbf{q}''); \quad \mathbf{q} = \mathbf{q}' + \mathbf{q}'', \tag{2.74}$$

where the equations (2.73) and (2.74) are more commonly called the *coalescence process* of phonons and the *decay process* of phonons, respectively.

Considering the coalescence process: if $\mathbf{q} + \mathbf{q}'$ lies within the first BZ one call it a *normal*-process or *N*-process. However, if $\mathbf{q} + \mathbf{q}'$ lies outside the first BZ, it is "flipped" back into the first BZ by a non-zero reciprocal lattice vector $\mathbf{G}$. Such an event is called an *umklapp*-process or *U*-process, which is illustrated in figure 2.4. The same description can be made for the decay process.

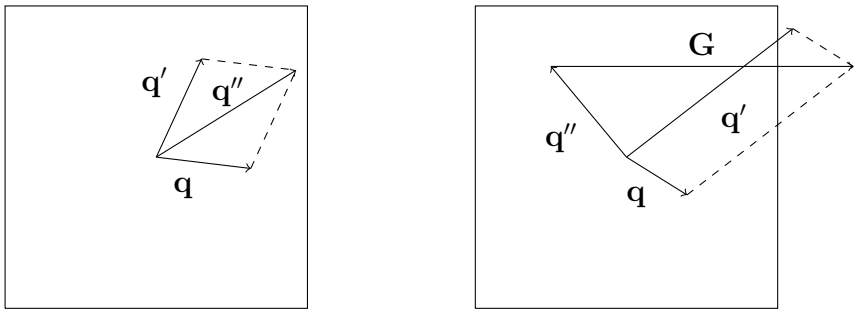

(a) *N*-process **(b)** *U*-process

Figure 2.4: Illustration of a) *N*-process of a three-phonon scattering where all wave vectors are within the first BZ, and (b) *U*-process where the wave vector $\mathbf{q}''$ is flipped back into the first BZ by a vector $\mathbf{G}$.

Anharmonic Relaxation Time

If one considers the anharmonic potential energy operator as a perturbation which acts on an initial state $|\mathrm{i}\rangle \equiv |n_{j\mathbf{q}}, n_{j'\mathbf{q}'}, n_{j''\mathbf{q}''}\rangle$: the system will change in time t and end up

in a final state $|\mathrm{f}\rangle$ given as

$$|\mathrm{f}\rangle = |n_{j\mathbf{q}} - 1, n_{j'\mathbf{q}'} - 1, n_{j''\mathbf{q}''} + 1\rangle, \tag{2.75}$$

$$|\mathrm{f}\rangle = |n_{j\mathbf{q}} - 1, n_{j'\mathbf{q}'} + 1, n_{j''\mathbf{q}''} + 1\rangle, \tag{2.76}$$

for the coalescence and decay process, respectively. The phonon occupation number $n_{j\mathbf{q}}$ is written as an expansion around its equilibrium up to the first-order perturbation $\psi_{j\mathbf{q}}$. The Bose-Einstein distribution then becomes

$$\begin{aligned} n_{j\mathbf{q}} &= \frac{1}{\mathrm{e}^{\hbar\omega(j\mathbf{q})/k_\mathrm{B}T - \psi_{j\mathbf{q}}} - 1} \\ &\simeq \bar{n}_{j\mathbf{q}} - \psi_{j\mathbf{q}} \frac{\partial \bar{n}_{j\mathbf{q}}}{\partial(\hbar\omega(j\mathbf{q}))} \\ &= \bar{n}_{j\mathbf{q}} + \psi_{j\mathbf{q}} \bar{n}_{j\mathbf{q}}(\bar{n}_{j\mathbf{q}} + 1). \end{aligned} \tag{2.77}$$

The function $\psi_{j\mathbf{q}}$ is a measure of the deviation from the equilibrium distribution for phonons in mode $j\mathbf{q}$.

The transition probability P_i^f from the initial state to the final state is given by Fermi's golden rule,

$$P_\mathrm{i}^\mathrm{f} = \frac{2\pi}{\hbar} |\langle \mathrm{f}|\hat{V}_3|\mathrm{i}\rangle|^2 \delta(E_\mathrm{f} - E_\mathrm{i}), \tag{2.78}$$

where E_i and E_f are the energy in the initial and final state, respectively. The delta function $\delta(E_\mathrm{f} - E_\mathrm{i})$ ensures energy conservation. By using Fermi's golden rule with the third-order potential energy operator $\hat{V}_3$ expressed in equation (2.52) on the initial and final state one get the transition probability for the three-phonon scattering mechanisms,

$$P_{j\mathbf{q},j'\mathbf{q}'}^{j''\mathbf{q}''} - P_{j''\mathbf{q}''}^{j\mathbf{q},j'\mathbf{q}'} = \tilde{P}_{j\mathbf{q},j'\mathbf{q}'}^{j''\mathbf{q}''}(\psi_{j\mathbf{q}} + \psi_{j'\mathbf{q}'} - \psi_{j''\mathbf{q}''}), \tag{2.79}$$

corresponding to the coalescence process: the annihilation of two and creation of one phonon. The two first terms correspond to forward and backward scattering, and $\tilde{P}_{j\mathbf{q},j'\mathbf{q}'}$ is given as

$$\begin{aligned} \tilde{P}_{j\mathbf{q},j'\mathbf{q}'}^{j''\mathbf{q}''} =& 2\pi \bar{n}_{j\mathbf{q}} \bar{n}_{j'\mathbf{q}'} (\bar{n}_{j''\mathbf{q}''} + 1) |\phi(-j\mathbf{q}, -j'\mathbf{q}', j''\mathbf{q}'')|^2 \\ & \times \delta(\omega(j''\mathbf{q}'') - \omega(j'\mathbf{q}') - \omega(j\mathbf{q})), \end{aligned} \tag{2.80}$$

A similar expression can be derived for the decay process: the annihilation of one and creation of two phonons,

$$P_{j\mathbf{q}}^{j'\mathbf{q}',j''\mathbf{q}''} - P_{j'\mathbf{q}',j''\mathbf{q}''}^{j\mathbf{q}} = \tilde{P}_{j\mathbf{q}}^{j'\mathbf{q}',j''\mathbf{q}''}(\psi_{j\mathbf{q}} - \psi_{j'\mathbf{q}'} - \psi_{j''\mathbf{q}''}), \tag{2.81}$$

where

$$\begin{aligned}\tilde{P}^{j'\mathbf{q}',j''\mathbf{q}''}_{j\mathbf{q}} =& 2\pi\bar{n}_{j\mathbf{q}}(\bar{n}_{j'\mathbf{q}'}+1)(\bar{n}_{j''\mathbf{q}''}+1)|\phi(-j\mathbf{q},j'\mathbf{q}',j''\mathbf{q}'')|^2 \\ &\times\delta(\omega(j\mathbf{q})-\omega(j'\mathbf{q}')-\omega(j''\mathbf{q}'')).\end{aligned} \tag{2.82}$$

The total rate of change in the phonon population $n_{j\mathbf{q}}$ due to the three-phonon interactions is the sum of the transition probabilities,

$$\begin{aligned}-\left.\frac{\partial n_{j\mathbf{q}}}{\partial t}\right|_{\text{anh}} =& \sum_{j'\mathbf{q}'j''\mathbf{q}''}\Big[\tilde{P}^{j''\mathbf{q}''}_{j\mathbf{q},j'\mathbf{q}'}(\psi_{j\mathbf{q}}+\psi_{j'\mathbf{q}'}-\psi_{j''\mathbf{q}''}) \\ &+\frac{1}{2}\tilde{P}^{j'\mathbf{q}',j''\mathbf{q}''}_{j\mathbf{q}}(\psi_{j\mathbf{q}}-\psi_{j'\mathbf{q}'}-\psi_{j''\mathbf{q}''})\Big],\end{aligned} \tag{2.83}$$

where the factor $1/2$ avoids double counting in the summation. The relaxation time $\tau^{\text{anh}}_{j\mathbf{q}}$ for anharmonic scattering can be expressed within the RTA with help of equation (2.66). The result is given as

$$\begin{aligned}\frac{1}{\tau^{\text{anh}}_{j\mathbf{q}}} =& \pi\sum_{j'\mathbf{q}'j''\mathbf{q}''}|\phi(-j\mathbf{q},j'\mathbf{q}',j''\mathbf{q}'')|^2 \\ &\Big[\frac{\bar{n}_{j'\mathbf{q}'}(\bar{n}_{j''\mathbf{q}''}+1)}{\bar{n}_{j\mathbf{q}}+1}\delta(\omega(j''\mathbf{q}'')-\omega(j'\mathbf{q}')-\omega(j\mathbf{q})) \\ &+\frac{(\bar{n}_{j'\mathbf{q}'}+1)(\bar{n}_{j''\mathbf{q}''}+1)}{\bar{n}_{j\mathbf{q}}+1}\delta(\omega(j\mathbf{q})-\omega(j'\mathbf{q}')-\omega(j''\mathbf{q}''))\Big].\end{aligned} \tag{2.84}$$

The deviation functions $\psi_{j'\mathbf{q}'}=0$ and $\psi_{j''\mathbf{q}''}=0$ because one assumes the single-mode relaxation time approximation where only phonons in mode $j\mathbf{q}$ deviates from its equilibrium distribution.

2.6.2 Mass-disorder

Introducing alloying in a crystal reduces the lattice thermal conductivity due to scattering of the phonons by the disorder in the crystal. Calculations of lattice thermal conductivity with scattering from mass-disorder within the relaxation time approximation requires an expression for $\tau^{\text{md}}_{j\mathbf{q}}$. This is done by considering the mass-disorder as a perturbation where one replaces the real crystal with an ordered *virtual crystal*, and the method is called the virtual crystal approximation (VCA).

The Hamiltonian for the ordered virtual crystal can be expressed as

$$\begin{aligned} H &= \frac{1}{2}\sum_{\mathbf{lb}\alpha} m(\mathbf{lb})\dot{u}_\alpha^2(\mathbf{lb}) + \hat{V}_2 \\ &= H_0 + H_{\mathrm{md}}. \end{aligned} \tag{2.85}$$

The second line separates the Hamiltonian into two parts: an unperturbed part H_0 and a perturbed part H_{md} with the contribution from mass-disorder. The unperturbed part is given as

$$\mathrm{H}_0 = \frac{1}{2}\sum_{\mathbf{lb}\alpha} \bar{m}(\mathbf{b})\dot{u}_\alpha^2(\mathbf{lb}) + \hat{V}_2, \tag{2.86}$$

where H_0 represent the virtual crystal, and $\bar{m}(\mathbf{b})$ is the average mass of atom $\mathbf{b}$. It is given as the sum of the concentration f_i of species i times the mass of the same element,

$$\bar{m}(\mathbf{b}) = \sum_i f_i(\mathbf{b}) m_i(\mathbf{b}). \tag{2.87}$$

The perturbed Hamiltonian H_{md} is given as

$$\begin{aligned} H_{\mathrm{md}} &= \frac{1}{2}\sum_{\mathbf{lb}\alpha} (m(\mathbf{lb}) - \bar{m}(\mathbf{b}))\dot{u}_\alpha^2 \\ &= \frac{1}{2}\sum_{\mathbf{lb}\alpha} \Delta m(\mathbf{lb})\dot{u}_\alpha^2, \end{aligned} \tag{2.88}$$

where $\Delta m(\mathbf{lb}) = m(\mathbf{lb}) - \bar{m}(\mathbf{b})$, and represents the difference in the mass of the real crystal compared to the virtual crystal. Further, by using the equation for atomic displacements (2.7), the first derivative of the displacement $\dot{u}_\alpha(\mathbf{lb})$ can be calculated. The Hamiltonian for mass-disorder can be written as

$$\begin{aligned} H_{\mathrm{md}} = -\frac{\hbar}{4}\sum_{\substack{\mathbf{b}jj' \\ \mathbf{q}\mathbf{q}'\mathbf{Q}}} &[\omega(j\mathbf{q}))\omega(j'\mathbf{q}')]^{1/2}\delta(\mathbf{q}+\mathbf{q}'+\mathbf{Q})\tilde{M}_{\mathbf{b}}(\mathbf{Q}) \\ &\times \mathbf{e}(\mathbf{b}|j\mathbf{q})\mathbf{e}(\mathbf{b}|j'\mathbf{q})[a_{j\mathbf{q}}a^\dagger_{-j'\mathbf{q}} + a^\dagger_{-j\mathbf{q}}a_{j'\mathbf{q}}] \end{aligned} \tag{2.89}$$

where $\tilde{M}_{\mathbf{b}}(\mathbf{Q})$ is the Fourier transform of $\Delta M(\mathbf{lb}) = \Delta m(\mathbf{lb})/\bar{m}(\mathbf{b})$:

$$\tilde{M}_{\mathbf{b}}(\mathbf{Q}) = \frac{1}{N}\Delta M(\mathbf{lb})\mathrm{e}^{-\mathrm{i}\mathbf{Q}\mathbf{l}}. \tag{2.90}$$

The delta function $\delta(\mathbf{q}+\mathbf{q}'+\mathbf{Q})$ is obtained by summing over $\mathbf{l}$. Applying Fermi's

golden rule and the single-mode RTA, the relaxation time for mass-disorder in a cubic system can be expressed as [46, 47]

$$\frac{1}{\tau_{j\mathbf{q}}^{\mathrm{md}}} = \frac{\pi}{6N}\omega^2(j\mathbf{q}) \sum_{\mathbf{b}} M_{\mathrm{var}}(\mathbf{b}) |\mathbf{e}(\mathbf{b}|j\mathbf{q})|^2 \sum_{j'\mathbf{q}'} \delta(\omega - \omega(j'\mathbf{q}')) |\mathbf{e}(\mathbf{b}|j'\mathbf{q}')|^2. \tag{2.91}$$

The scattering rate is described by the squared amplitudes of the initial phonon multiplied by the partial density of states of the final phonon weighted by the squared amplitude of the same phonon. $M_{\mathrm{var}}(\mathbf{b})$ is called the *mass-variance* parameter obtained from an ensemble average where a completely random distribution of the species is assumed. The parameter is given as

$$M_{\mathrm{var}}(\mathbf{b}) = \sum_i f_i(\mathbf{b}) \left(1 - \frac{m(\mathbf{lb})}{\bar{m}(\mathbf{b})}\right)^2. \tag{2.92}$$

The result from equation (2.91) accounts for the mass-disorder introduced when alloying on the *X*-site in *X*NiSn.

2.6.3 Grain boundaries

At sufficiently low temperatures, the mean free path (MFP) of a phonon will exceed the dimensions of the grain size in a polycrystalline material. In this temperature range it is assumed that phonons will scatter several times at the grain boundaries before it is scattered internally by another phonon or by mass-disorder; thus, scattering by the grain boundaries are most prominent at low temperatures. An expression for the relaxation time for boundary scattering is derived in [48],

$$\frac{1}{\tau_{j\mathbf{q}}^{\mathrm{bs}}} = \frac{v_{j\mathbf{q}}}{L}, \tag{2.93}$$

where $v_{j\mathbf{q}}$ is the group velocity and L is the MFP resulting from grain boundary scattering. This equation assumes completely diffusive scattering, i.e. there is no reflection of phonons, and all of the incoming energy is absorbed and re-emitted at all boundaries. The boundary MFP can be averaged over all geometrical orientations of the grain boundaries [48]. For a polycrystalline material the boundary MFP in the diffusive scattering model is equivalent to the average grain size; thus, the MFP will be denoted as the average grain size in the following sections.

The model is only valid if the scattering from grain boundaries occurs uniformly throughout the volume of the specimen. In a polycrystalline material, this condition

can be approximated to specimens with a small acoustic mismatch between the grains. However, to fully account for the effect of grain boundary scattering on the lattice thermal conductivity, the relative orientation between the grain boundaries and the surface roughness of the grains have to be considered.

Chapter 3

Computational Methods

Computational methods for modeling of material properties have been an increasing field the past years due to the increased power of computers. Density functional theory (DFT) is such a method and it is based upon first principles. The calculations of the second- and third-order force constants in this work are obtained from DFT as implemented in the VASP package [49, 50]. This chapter will go through the basics of DFT and how we obtain the force constants from the frozen phonon approach. A more in-depth description of the quantum mechanics in DFT may be found in [51–53].

3.1 Many-particle Problem

To understand various properties of materials, one have to describe the interactions between all electrons and nuclei within the material. The many particle wave function describes the position of the electrons and nuclei with $i = 1, 2, \cdots, N_\mathrm{e}$ and $j = 1, 2, \cdots, N_\mathrm{n}$, number of electrons and nuclei, respectively. The wave function can be written as

$$\Psi(\mathbf{r}_i, \mathbf{R}_j) \equiv \Psi(\mathbf{r}_1, \mathbf{r}_2, \cdots, \mathbf{r}_{N_\mathrm{e}}, \mathbf{R}_1, \mathbf{R}_2, \cdots, \mathbf{R}_{N_\mathrm{n}}). \tag{3.1}$$

A study of materials on a quantum mechanical level is based upon solving the time-independent or time-dependent Schrödinger equation; however, we will only consider the time-independent Schrödinger equation. It can be written as

$$\hat{H}\Psi(\mathbf{r}_i, \mathbf{R}_j) = E^\mathrm{tot}\Psi(\mathbf{r}_i, \mathbf{R}_j), \tag{3.2}$$

where $\hat{H}$ is the total energy Hamiltonian for the system, which contains the sum of all interactions. The Hamiltonian is given as

$$\begin{aligned}\hat{H} = &-\sum_{i=1}^{N_\mathrm{e}} \frac{\hbar^2 \nabla_i^2}{2m_\mathrm{e}} - \sum_{j=1}^{N_\mathrm{n}} \frac{\hbar^2 \nabla_j^2}{2m_j} + \sum_{i<i'}^{N_\mathrm{e}} \frac{q^2}{|\mathbf{r}_j - \mathbf{r}_{j'}|} \\ &+ \sum_{j<j'}^{N_\mathrm{n}} \frac{q^2 Z_j Z_{j'}}{|\mathbf{R}_j - \mathbf{R}_{j'}|} - \sum_{i=1}^{N_\mathrm{e}} \sum_{j=1}^{N_\mathrm{n}} \frac{q^2 Z_j}{|\mathbf{r}_i - \mathbf{R}_j|},\end{aligned} \tag{3.3}$$

where Z_j is the atom number and m_j is the mass of the nuclei. The first two terms in equation (3.3) represents the kinetic energy of the electrons and nuclei. The third and forth term describes the Coulomb repulsion between electron-electron pairs and nucleus-nucleus pairs. The last term describes Coulomb attraction between electron-nucleus pairs. A compact form of equation (3.2) can be defined:

$$\hat{H} = \hat{T}_\mathrm{e} + \hat{T}_\mathrm{n} + \hat{U}_\mathrm{ee} + \hat{U}_\mathrm{nn} + \hat{U}_\mathrm{en}, \tag{3.4}$$

where

$$\begin{aligned}\hat{T}_\mathrm{e} &= -\sum_{i=1}^{N_\mathrm{e}} \frac{\hbar^2 \nabla_i^2}{2m_\mathrm{e}} \\ \hat{T}_\mathrm{n} &= -\sum_{j=1}^{N_\mathrm{n}} \frac{\hbar^2 \nabla_j^2}{2m_j} \\ \hat{U}_\mathrm{ee} &= \sum_{i<i'}^{N_\mathrm{e}} \frac{q^2}{|\mathbf{r}_j - \mathbf{r}_{j'}|} \\ \hat{U}_\mathrm{nn} &= \sum_{j<j'}^{N_\mathrm{n}} \frac{q^2 Z_j Z_{j'}}{|\mathbf{R}_j - \mathbf{R}_{j'}|} \\ \hat{U}_\mathrm{en} &= -\sum_{i=1}^{N_\mathrm{e}} \sum_{j=1}^{N_\mathrm{n}} \frac{q^2 Z_j}{|\mathbf{r}_i - \mathbf{R}_j|}.\end{aligned} \tag{3.5}$$

3.1.1 Born-Oppenheimer Approximation

Solving the many-particle Schrödinger equation requires immense computational power. To simplify the many-particle problem, a separation of variables in the wave function can be done. The separation may be written as a product between the electron wave

function and nuclei wave function,

$$\Psi(\mathbf{r}_i, \mathbf{R}_j) = \psi(\mathbf{r}_1, \mathbf{r}_2, \cdots, \mathbf{r}_{N_\mathrm{e}}, \mathbf{R}_1, \mathbf{R}_2, \cdots, \mathbf{R}_{N_\mathrm{n}})\chi(\mathbf{R}_1, \mathbf{R}_2, \cdots, \mathbf{R}_{N_\mathrm{n}}), \tag{3.6}$$

where $\psi(\mathbf{r}_i, \mathbf{R}_j)$ and $\chi(\mathbf{R}_j)$ are the wave function for electrons and nuclei, respectively. The separation is based on the assumption that the nuclei are assumed to be stationary point particles compared to the electrons, which is due to the massive mass difference. The electrons depends on the positions of the stationary nuclei $\mathbf{R}_j$.

Furthermore, the *bra-ket* notation will be used for compactness. A wave function $\Psi(\mathbf{r}) \equiv \langle \mathbf{r}|\Psi\rangle$ will be written as the *ket* $|\Psi\rangle$, and the complex conjugate will be written as the *bra* $\langle\Psi|$. With this, the eigenvalue equation from (3.2) can be rewritten:

$$\hat{H}|\psi(\mathbf{R}_j)\rangle|\chi\rangle = E^{\mathrm{tot}}|\psi(\mathbf{R}_j)\rangle|\chi\rangle. \tag{3.7}$$

The dependence of the positions of the nuclei in the electron wave function is kept as a reminder. The Hamiltonian from equation (3.3) can be considered to have pure electronic terms and pure nuclear terms,

$$\begin{aligned} \hat{H}_\mathrm{e} &= \hat{T}_\mathrm{e} + \hat{U}_\mathrm{ee} + \hat{U}_\mathrm{en} \\ \hat{H}_\mathrm{n} &= \hat{T}_\mathrm{n} + \hat{U}_\mathrm{nn}. \end{aligned} \tag{3.8}$$

The next step is to multiply each side by $\langle\psi(\mathbf{R}_j)|$ and use the normalization condition $\langle\psi(\mathbf{R}_j)|\psi(\mathbf{R}_j)\rangle = 1$. This step gives

$$\begin{aligned} \langle\psi(\mathbf{R}_j)|\hat{H}_\mathrm{e}|\psi(\mathbf{R}_j)\rangle|\chi\rangle + \langle\psi(\mathbf{R}_j)|\hat{H}_\mathrm{n}|\psi(\mathbf{R}_j)\rangle|\chi\rangle &= E^{\mathrm{tot}}|\chi(\mathbf{R}_j)\rangle \\ E(\mathbf{R}_j)|\chi\rangle + \langle\psi(\mathbf{R}_j)|\hat{H}_\mathrm{n}|\psi(\mathbf{R}_j)\rangle|\chi\rangle &= E^{\mathrm{tot}}|\chi\rangle, \end{aligned} \tag{3.9}$$

where $E(\mathbf{R}_j)$ is the electronic energy,

$$\hat{H}_\mathrm{e}|\psi(\mathbf{R}_j)\rangle = E(\mathbf{R}_j)|\psi(\mathbf{R}_j)\rangle. \tag{3.10}$$

The second term in equation (3.9) may be simplified by neglecting all terms containing $\nabla_j|\psi(\mathbf{R}_j)\rangle$; that is, the electronic wave function does not change drastically upon displacements of the nuclei. The result is known as the *Born-Oppenheimer approximation*, where equation (3.9) may be written as

$$(\hat{T}_\mathrm{n} + \hat{U}_\mathrm{nn} + E(\mathbf{R}_j))|\chi\rangle = E^{\mathrm{tot}}|\chi\rangle. \tag{3.11}$$

The total energy can may be calculated by solving equation (3.11), where the electronic

energy $E(\mathbf{R}_j)$ is obtained from equation (3.10).

3.1.2 Hartee and Hartree-Fock Approximation

Approximations have been made to solve the many-electron wave function in equation (3.10). Hartree suggested that the electrons are independent of each other, and that the total electron wave function Ψ^{H} could be written as a product of all single-electron wave functions for all possible wave numbers,

$$\Psi^{\mathrm{H}}(\mathbf{r}_i) = \psi_1(\mathbf{r}_1)\psi_2(\mathbf{r}_2)\cdots\psi_{N_\mathrm{e}}(\mathbf{r}_{N_\mathrm{e}}). \tag{3.12}$$

The superscript stands for Hartree. However, the Hartree approximation neglects the anti-symmetry of the wave function; that is, the electrons are indistinguishable and do not obey the Pauli exclusion principle for fermions. The Hartree-Fock approximation expresses the many-particle wave function in a so-called *Slater determinant*,

$$\Psi^{\mathrm{HF}}(\mathbf{r}_i) = \frac{1}{\sqrt{N_\mathrm{e}!}}\begin{vmatrix} \psi_1(\mathbf{r}_1) & \psi_2(\mathbf{r}_1) & \cdots & \psi_{N_\mathrm{e}}(\mathbf{r}_1) \\ \psi_1(\mathbf{r}_2) & \psi_2(\mathbf{r}_2) & \cdots & \psi_{N_\mathrm{e}}(\mathbf{r}_2) \\ \vdots & \vdots & \ddots & \vdots \\ \psi_1(\mathbf{r}_{N_\mathrm{e}}) & \psi_1(\mathbf{r}_{N_\mathrm{e}}) & \cdots & \psi_{N_\mathrm{e}}(\mathbf{r}_{N_\mathrm{e}}). \end{vmatrix} \tag{3.13}$$

By using the variational method, one may obtain the ground state eigenfunction and transform the N_e-particle equation into N_e equations of single particles. One has to write the total energy as a functional of the single-particle wave functions to obtain the Hartree-Fock equations,

$$E[\psi_i] = \langle\psi_i|\hat{H}|\psi_i\rangle. \tag{3.14}$$

For simplicity, one may require that the wave functions are normalized and orthogonal, i.e.

$$\langle\psi_i|\psi_i\rangle = 1, \text{and } \langle\psi_i|\psi_{i'}\rangle = \langle\psi_{i'}|\psi_i\rangle = 0. \tag{3.15}$$

The variational method may be used to find the function ψ_i which minimizes the total energy to the ground state energy. The minimization step uses the Lagrange multiplier and it requires a lot of algebra. The full derivation can be found in reference [52]. The result is called the Hartree-Fock (HF) single-electron equations. There are N_e number of single electron equations which are only valid for the ground state energy due to the nature of the minimization process. It is given as

$$\left[-\frac{\hbar^2}{2m_\mathrm{e}}\nabla^2 + V_{\mathrm{ext}}(\mathbf{r}) + V^{\mathrm{H}}(\mathbf{r})\right]\psi_i(\mathbf{r}) + \int V_{\mathrm{x}}^{\mathrm{HF}}(\mathbf{r},\mathbf{r}')\psi_i(\mathbf{r}')\mathrm{d}\mathbf{r}' = \epsilon_i\psi_i(\mathbf{r}), \tag{3.16}$$

where $V_{\text{ext}}(\mathbf{r})$, $V^{\text{H}}(\mathbf{r})$ and $V_{\text{x}}^{\text{HF}}(\mathbf{r}, \mathbf{r}')$ are the external potential, Hartree potential and Hartree-Fock exchange potential. The Hartree and Hartree-Fock potentials are defined as

$$\begin{aligned} V^{\text{H}}(\mathbf{r}) &= \int \frac{n(\mathbf{r}') - n_i(\mathbf{r}')}{|\mathbf{r} - \mathbf{r}'|} \mathrm{d}\mathbf{r}' \\ V_{\text{x}}^{\text{HF}}(\mathbf{r}, \mathbf{r}') &= -\sum_i \frac{\psi_i^*(\mathbf{r}')\psi_i(\mathbf{r})}{|\mathbf{r} - \mathbf{r}'|}. \end{aligned} \tag{3.17}$$

The Hartree potential describes interactions between electrons in the system, but it does not include exchange and correlation effects. The $-n_i(\mathbf{r}')$ in the Hartree potential excludes self-interactions. The Hartree-Fock exchange potential is an effect from Pauli exclusion principle: two electrons cannot be in the same quantum state. In fact, they cannot be in the same quantum state with parallel spin. Incorporation of the spin requirement can be done as follows: each integral over the space variable must include a summation over the spin orientation $\sigma = \pm 1/2$, i.e. $\int \mathrm{d}\mathbf{r} \rightarrow \sum_\sigma \int \mathrm{d}\mathbf{r}$, the derivation has been shown in [53]. The Hartree-Fock approximation includes exchange effects but neglects the correlation effects.

3.2 Density Functional Theory

Density functional theory is based on the theorems by Hohenberg-Kohn [54]. The first theorem states that the external potential $V_{\text{ext}}(\mathbf{r})$ for any system of electrons is an unique functional of its ground state density $n_0(\mathbf{r})$. If the ground state density is known, then the external potential is known; thus, we will have the Hamiltonian and may solve the many-particle wave function in the ground state. Another consequence is that the ground state density determines all ground state properties. The theorem is very convenient to reduce the many-particle problem with $3N_{\text{e}}$ number of spatial variables to only 3 variables: x, y and z.

The second theorem states that there exists an universal energy functional of the density $F[n(\mathbf{r})]$ which is valid for any electron system, i.e. for all possible external potentials $V_{\text{ext}}(\mathbf{r})$. The density which minimizes the energy functional of a given system is the exact ground state density $n_0(\mathbf{r})$.

3.2.1 Kohn-Sham Equation

The Hohenberg-Kohn theorems states that one may define the ground state energy if the ground state density $n_0(\mathbf{r})$ is known. The problem is that the universal energy functional $F[n(\mathbf{r})]$ is not known.

The total energy functional can be written in terms of the universal functional $F[n(\mathbf{r})]$ and the external potential $V_{\text{ext}}(\mathbf{r})$,

$$\begin{aligned} E[n(\mathbf{r})] &= F[n(\mathbf{r})] + \int V_{\text{ext}}(\mathbf{r}) n(\mathbf{r}) \mathrm{d}\mathbf{r} \\ &= T_{\text{s}}[n(\mathbf{r})] + U_{\text{en}}[n(\mathbf{r})] + E^{\text{H}}[n(\mathbf{r})] + E_{\text{xc}}[n(\mathbf{r})], \end{aligned} \tag{3.18}$$

where $T_{\text{s}}[n(\mathbf{r})]$ is the kinetic energy of non-interacting electrons, $E^{\text{H}}[n(\mathbf{r})]$ is the Hartree energy and $E_{\text{xc}}[n(\mathbf{r})]$ is the exchange-correlation energy which contains the complex many-electron interactions.

The many-particle wave function is assumed to be described by the Hartree approximation in terms of Kohn-Sham (KS) single-particle wave functions,

$$\Psi(\mathbf{r}_i) = \psi_1^{\text{KS}}(\mathbf{r}_1)\psi_2^{\text{KS}}(\mathbf{r}_2)\cdots\psi_{N_{\text{e}}}^{\text{KS}}(\mathbf{r}_{N_{\text{e}}}), \tag{3.19}$$

where ψ_i^{KS} is the Kohn-Sham wave functions. The ψ_i^{KS} that minimizes the functionals in equation (3.18) will define the ground state density. The variational method is used to find the exact ground state energy, and the result will be the KS equation which includes exchange and correlation effects [55]. The Kohn-Sham equation is given as

$$\left[-\frac{\hbar^2}{2m_{\text{e}}}\nabla_i^2 + V_{\text{eff}}(\mathbf{r})\right]\psi_i^{\text{KS}}(\mathbf{r}) = \epsilon_i^{\text{KS}}\psi_i^{\text{KS}}(\mathbf{r}), \tag{3.20}$$

where ϵ_i^{KS} is the single-electron energies. $V_{\text{eff}}(\mathbf{r})$ is the effective potential,

$$\begin{aligned} V_{\text{eff}}(\mathbf{r}) &= V_{\text{ext}}(\mathbf{r}) + \frac{\delta E^{\text{H}}[n(\mathbf{r})]}{\delta n(\mathbf{r})} + \frac{\delta E_{\text{xc}}[n(\mathbf{r})]}{\delta n(\mathbf{r})} \\ &= V_{\text{ext}}(\mathbf{r}) + V^{\text{H}}(\mathbf{r}) + V_{\text{xc}}(\mathbf{r}). \end{aligned} \tag{3.21}$$

The total energy can be expressed in terms of the exchange-correlation energy and the single-electron energies,

$$E[n(\mathbf{r})] = \sum_i \epsilon_i^{\text{KS}} - \frac{1}{2}\int V^{\text{H}}(\mathbf{r})\mathrm{d}\mathbf{r} - \int V_{\text{xc}}(\mathbf{r})\mathrm{d}\mathbf{r} + E_{\text{xc}}[n(\mathbf{r})], \tag{3.22}$$

and it is obtained from self-consistent field calculations. The loop starts with an initial guess of the density $n(\mathbf{r})$. Then one solves the many KS single-electron wave functions in equation (3.20) with the initial density which gives the wave functions ψ_i^{KS} and the

total energy. A new density is defined with the obtained wave functions,

$$n(\mathbf{r}) = \sum_i |\psi_i^{\mathrm{KS}}|^2, \tag{3.23}$$

and a new effective potential is calculated. These steps are repeated until the total energy is converged; thus, we have reached the ground state energy and obtained the ground state density.

To solve the KS equation, we will need an expression for the unknown exchange-correlation functional $E_{\mathrm{xc}}[n(\mathbf{r})]$. There exist several approximations for such a complex functional.

3.3 Exchange and Correlation

The Kohn-Sham equation generates the exact energy if the exchange-correlation functional $E_{\mathrm{xc}}[n]$ is exact. The exchange-correlation functional is not known to date, and approximations are needed to describe it. The local density approximation (LDA) assumes that the density can be treated locally as uniform electron gas; that is, the exchange-correlation energy at any point in the system is the same as for uniform electron gas of the same density. The exchange-correlation functional within LDA is given as

$$E_{\mathrm{xc}}^{\mathrm{LDA}}[n(\mathbf{r})] = \int n(\mathbf{r}) \epsilon_{\mathrm{xc}}^{\mathrm{gas}}[n(\mathbf{r})] \mathrm{d}\mathbf{r}, \tag{3.24}$$

where $\epsilon_{\mathrm{xc}}^{\mathrm{gas}}[n(\mathbf{r})]$ is the exchange-correlation energy per particle of an uniform electron gas with density $n(\mathbf{r})$.

Real systems are not homogeneous: the electrons have variations in the density landscape. The generalized gradient approximation (GGA) describes the electron density with a gradient at a given point. The exchange-correlation functional is given as [56, 57]

$$E_{\mathrm{xc}}^{\mathrm{GGA}}[n(\mathbf{r})] = \int n(\mathbf{r}) \epsilon_{\mathrm{xc}}^{\mathrm{GGA}}[n, \nabla n(\mathbf{r})] \mathrm{d}\mathbf{r}, \tag{3.25}$$

where the exchange-correlation energy $\epsilon_{\mathrm{xc}}^{\mathrm{GGA}}$ accounts for the gradient to the electron density.

3.4 Frozen Phonon Approach

The force constants can be obtained from density functional perturbation theory (DFPT) [58, 59] or by a direct approach. We have used the direct approach called the finite-displacement method or frozen phonon method. In principle, the method consists of calculating the forces caused by displacement of one atom. The forces are calculated with DFT for each unique displacement; that is, crystal symmetry is used to reduce the number of displacements. Once the forces caused by displacing one atom are obtained, the interatomic force constant matrix up to the second-order can be constructed [60, 61]. The frequencies can now be calculated by solving the dynamical matrix equation. Constructing the third-order force constant matrix requires two simultaneously displacements of the atoms. This increases the number of unique displacements; therefore, the computational time increases significantly. The finite-displacement method requires a supercell approach, and the supercell have to be sufficiently large to prevent artificial forces due to the periodic boundary conditions used in DFT calculations.

Chapter 4

Computational Details

All first principles calculations in this work was performed with DFT as implemented in the VASP package [49] with the projector-augmented wave (PAW) pseudopotential [50]. The generalized gradient approximation (GGA) by Perdew, Burke and Ernzerhof (PBE) was used as the exchange correlation potential [57].

A convergence study of lattice thermal conductivity and frequencies were conducted with respect to $\mathbf{k}$-mesh and energy cutoff in TiNiSn half-Heusler with a $2\times2\times2$ supercell of the primitive unit cell. This was done within the PHONO3PY package [62]. Each PHONO3PY calculation included 255 unique displacements.

The primitive unit cell is relatively small; thus, artificial forces may arise due to the periodic boundary condition. Going from the primitive cell to the cubic cell increased the unit cell size and thus decreased interactions between each unit cell. The primitive $2\times2\times2$ supercell has 24 atoms and a volume of 420.45Å^3. The $2\times2\times2$ cubic supercell has 96 atoms and a volume of 1681.23 Å^3. All calculations after the convergence of κ_l and $\omega(j\mathbf{q})$ were done on the $2 \times 2 \times 2$ supercell of the conventional unit cell. The increase in size reduces the number of $\mathbf{k}$-points needed to acquire the same convergence. The energy cutoff and $\mathbf{k}$-mesh was set to $450\ \text{eV}$ and $3 \times 3 \times 3$, respectively. The effect on the frequencies from various values for the magnitude of the displacements were compared. The resulting forces from the frozen phonon approach was converged with an accuracy better than $10^{-8}\ \text{eV}/\text{Å}$.

Sampling of the frequencies and relaxation times requires an integration over the BZ. The forces were Fourier-interpolated into a finer mesh, as implemented in the packages PHONOPY [63] and PHONO3PY [62]. This study used the tetrahedron method to sample the BZ [64, 65]. A well converged DOS and relaxation times was achieved with a sampling mesh of $30 \times 30 \times 30$.

4.1 Relaxation of the Structures

Relaxation of the structure was done for the cubic *X*NiSn half-Heuslers containing in total 12 atoms. The energy cutoff was set to 600 eV with a $\mathbf{k}$-mesh of $7 \times 7 \times 7$. The obtained lattice parameters were in good agreement with previous first principles calculations [66, 67], as well as the reported values from experiments [68].

Table 4.1: The lattice parameters in the conventional *X*NiSn from our calculations in comparison with another theory and experimental results. The lattice parameters measurements was conducted at room temperature [68].

	a (Å)		
	This study	DFT [67]	Exp. [68]
TiNiSn	5.945	5.945	5.9298(1)
ZrNiSn	6.153	6.153	6.1089(1)
HfNiSn	6.109	6.113	6.0795(1)

4.2 Convergence of Lattice Thermal Conductivity and Frequency

4.2.1 k-mesh

The convergence tests of κ_l and $\omega(j\mathbf{q})$ was performed on a $2 \times 2 \times 2$ supercell of the primitive unit cell. The $\mathbf{k}$-mesh varied from $3 \times 3 \times 3$ to a denser mesh of $14 \times 14 \times 14$. The energy cutoff was set to $600\,\mathrm{eV}$ in those convergence calculations.

Figure 4.1a) shows κ_l for different temperatures. The change of the lattice thermal conductivity was below 10^{-1} W/mK for all the different $\mathbf{k}$-meshes. The change oscillates for all meshes and the lattice thermal conductivity had reached good convergence already at a mesh with $3\times3\times3$. The change in the frequencies with respect to the different $\mathbf{k}$-meshes are illustrated in figure 4.1b) for an arbitrary $\mathbf{q}$-vector with no degeneracy of the frequency. The results suggested that an error of $\sim 10^{-2}$ meV in the frequencies corresponds to an error of $\sim 10^{-1}$ W/mK in the lattice thermal conductivity.

4.2.2 Energy Cutoff

The convergence tests of κ_l and $\omega(j\mathbf{q})$ were performed with various values for the energy cutoff to the plane waves. The $\mathbf{k}$-mesh was set to $9 \times 9 \times 9$ for all convergence

calculations, where the energy cutoff varied from 250-800 eV with an interval of 50 eV.

Increasing the energy cutoff reduced the change in the lattice thermal conductivity. An energy cutoff equal to $450\ \mathrm{eV}$ showed a change less than 10^{-1} W/mK in κ_l for all temperatures. At higher energy cutoff, even less change in lattice thermal conductivity was observed. As for the frequency, the average change for all bands was less than 10^{-3} meV for an energy cutoff equal to $450\ \mathrm{eV}$. The results suggested that an error of $\sim 10^{-3}$ meV in frequencies corresponds to an error of $\sim 10^{-1}$ W/mK in lattice thermal conductivity.

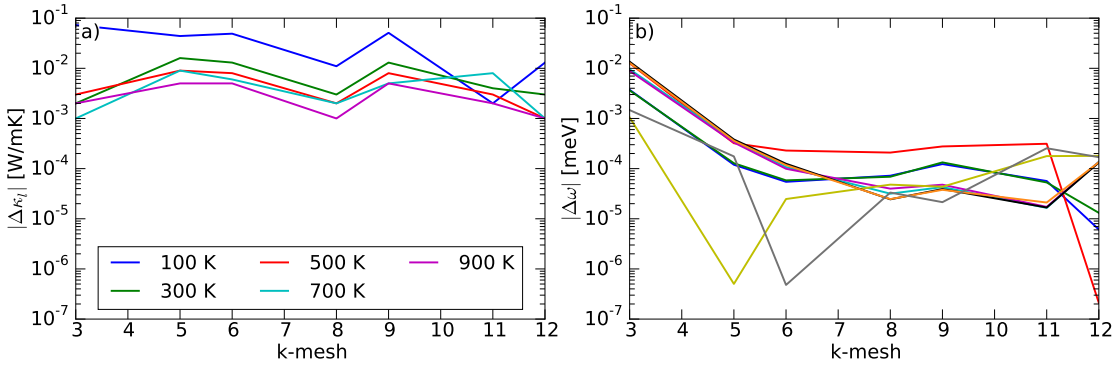

Figure 4.1: a) The change in κ_l and b) the change in $\omega(j\mathbf{q})$ at nine arbitrary phonon mode $j\mathbf{q}$ when increasing the mesh from $n \times n \times n$ to $(n+1) \times (n+1) \times (n+1)$. The value on the x-axis corresponds to the latter $(n+1) \times (n+1) \times (n+1)$ cubic mesh.

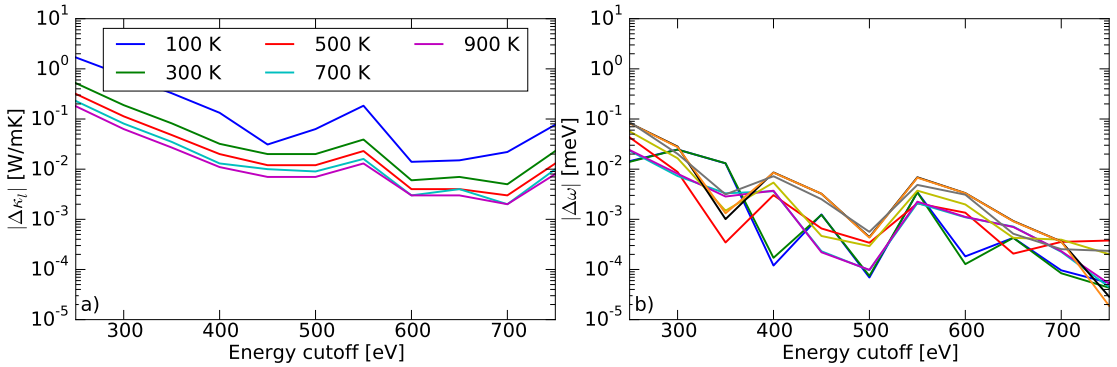

Figure 4.2: a) The change in lattice thermal conductivity and b) the change in frequency as a function of the energy cutoff.

4.3 Effect of Displacement

The harmonic approximation is not valid for too large displacements where anharmonicity have larger contributions. At very small displacements an inaccuracy was also ob-

served. The origin of this inaccuracy stems from the challenges in the calculations of very small energy differences with density functional theory [51]. The frequencies were relatively insensitive to the amplitude of the displacement. The highest variation of the frequencies was observed at the higher energetic phonons: the maximal change was 0.03 meV.

Calculations of the frequencies with amplitudes ranging from $0.001 - 0.1$ Å have been performed within the harmonic approximation. Figure 4.3 shows the change in frequencies as a function of the displacement lengths for three arbitrary $j\mathbf{q}$ phonon modes. Effects from anharmonicity had a larger impact when the displacements were above

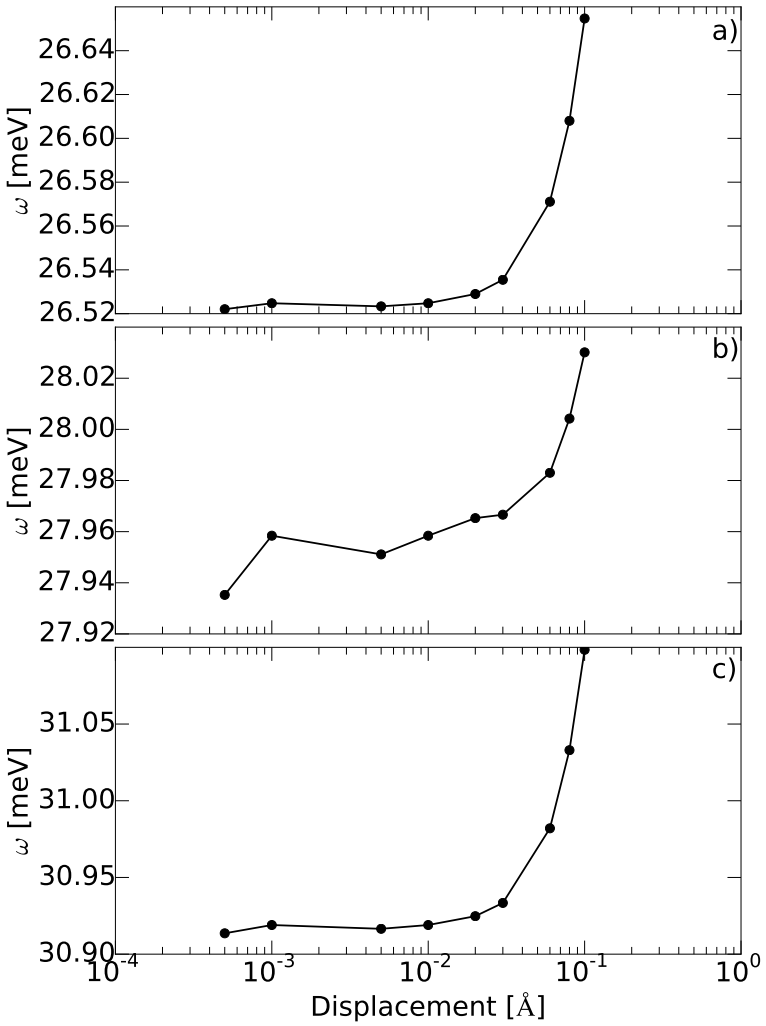

Figure 4.3: Frequencies at representative $j\mathbf{q}$ mode where a) is for a phonon at the Γ-point and the lowest TO branch, b) is for the L-point and the lowest TA branch and c) is for X-point and the highest energetic TO branch.

0.3 Å. Numerical inaccuracy was most prominent at the displacements below 0.001 Å. The displacement for further calculations was set to 0.03 Å for both the harmonic and anharmonic force calculations.

4.4 Brillouin Zone Sampling

Properties like DOS and relaxation times requires an evaluation of the sum in the reciprocal space with a large number of $\mathbf{q}$-points. It exists several different integration methods, e.g. the tetrahedron method and the Gaussian smearing method. An advantage with using the tetrahedron method compared to the Gaussian smearing method is that it can be parameter-free [62].

Density of states was obtained by evaluating the summation from equation (2.55) with the tetrahedron method. A converged result of DOS was obtained with a $30\times30\times30$ sampling mesh.

It has been reported that the Gaussian smearing method generally underestimates the relaxation time; thus, Gaussian smearing underestimates the lattice thermal conductivity as well [62]. The sampling of anharmonic relaxation times from equation (2.84) was performed with the tetrahedron method over the irreducible part of the Brillouin zone as described in [64, 65]. A converged result was obtained with a sampling mesh of $30 \times 30 \times 30$.

Chapter 5

Results

5.1 Harmonic Properties

5.1.1 Phonon Dispersion

The phonon dispersion shows the distribution of phonon vibrations within the first Brillouin zone, which is of great interest when investigating heat conduction from lattice vibrations. The phonon dispersion for TiNiSn, ZrNiSn and HfNiSn is shown in figure 5.1a-c), respectively. The three expected acoustic phonon branches and the six optical phonon branches are observed. As there are no imaginary phonon modes, the crystal is stable under small distortions. The inclusion of the non-analytic correction term results in a LO-TO splitting for the upper optical phonons at the zone center for all the three *X*NiSn half-Heuslers which are observed in figure 5.1.

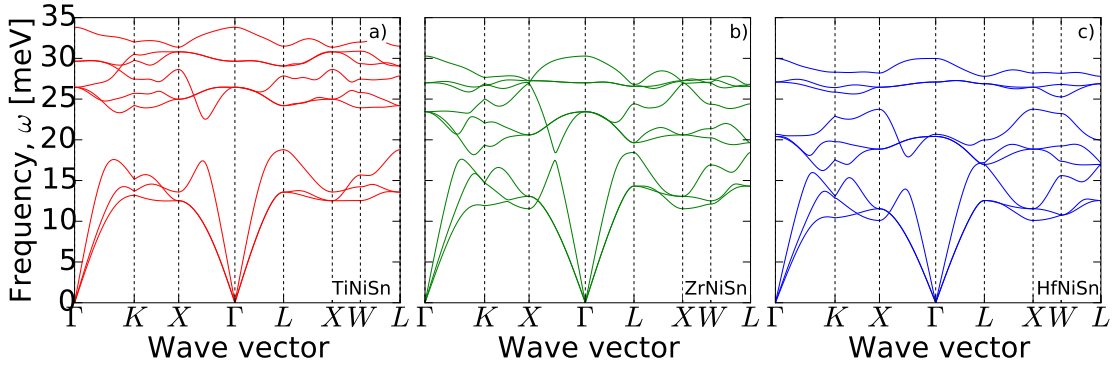

Figure 5.1: The phonon dispersion for a) TiNiSn, b) ZrNiSn and c) HfNiSn. The curves shows qualitative similarities; however, substitution on the *X*-site with a heavier atom show a shift of the phonon branches towards lower frequencies.

An energy gap between the acoustic and optical phonon branches is observed for the TiNiSn half-Heusler. The energy gap increases with the mass difference of the atoms: a substitution with Zr on the Ti-site decreases the frequencies, and the energy gap in the ZrNiSn half-Heusler is closed as seen in figure 5.1b); however, the phonon branches does not overlap in the reciprocal space. In this case, the frequencies for the acoustic phonons are shifted $< 3\%$, whereas the frequencies for the optical phonons are shifted $\sim 15\%$. A substitution with the heavier Hf-atom on the *X*-site results in a decrease of the frequencies for the acoustic phonons and a further decrease of the three lower optical phonons. A new frequency gap between the optical branches is observed in the HfNiSn half-Heusler; the frequencies for the upper three optical phonon branches are shifted $< 1\%$, whilst the frequency shift was very similar for all the other phonon branches with $\sim 13\%$ decrease in frequencies. In TiNiSn and ZrNiSn, a transition of phonons in the acoustic branches to the optical branches would require an additional momentum due to the lack of overlapping branches. In contrast, at the high symmetry point L in HfNiSn, a phonon can make a transition from the acoustic branches to the optical branches without the need of any additional momentum.

The shape of the phonon dispersion curves shows qualitative similarities; in fact, keeping the second-order forces of TiNiSn and changing the mass from Ti to Zr reproduces the closing of the energy gap. This result is illustrated in figure 5.2: the solid line is the dispersion of TiNiSn half-Heusler with its own forces, and the dotted line is the dispersion with a change in the mass from Ti to Zr while keeping the TiNiSn forces.

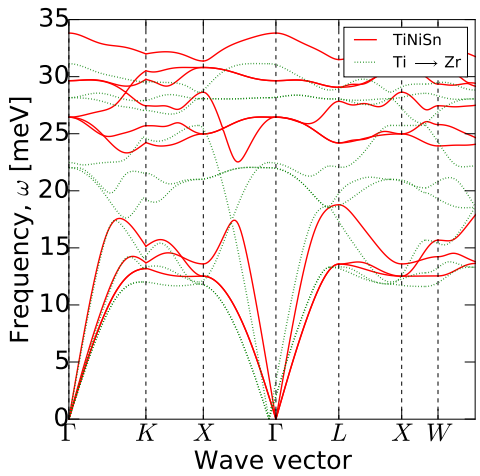

Figure 5.2: The phonon dispersion holding TiNiSn forces constant while changing the mass on the *X*-site. The solid line represents the dispersion with Ti mass and the dotted line is the dispersion with Zr mass

Because of the similar structures, the lowering of the frequencies is mainly due to the mass difference. The result emphasizes the possibility to tune the phonon dispersion with an isoelectronic substitution on the *X*-site without any drastic change in the phonon dispersion. This is of interest when investigating strategies to obtain a low lattice thermal conductivity. The effect of the phonon dispersion on κ_l are discussed in more detail when anharmonicity are included in the calculations in section 5.2.1.

5.1.2 Phonon Density of States

The total phonon density of states (DOS) represents the number of states per interval of energy which are available to be occupied. The partial density of states (PDOS) is a measure of the relative contribution from the motion of each atom to the phonon mode $j\mathbf{q}$. DOS and PDOS are shown in figure 5.3. The general trend when substituting the atom on the *X*-site (*X*=Ti, Zr or Hf) on the phonon dispersion is reflected in the DOS: the lowering of the frequencies in phonon branches are reflected as a shift in DOS towards lower frequencies, which is seen in figure 5.3.

There are regions with dominant contribution from one of the three atoms to the total phonon DOS in a *X*NiSn half-Heusler. The phonon states in the acoustic region are dominantly created by the heaviest atom in the *X*NiSn compound. For TiNiSn and ZrNiSn, the contribution comes from the Sn atoms. For HfNiSn, the contribution to the acoustic states is dominated by the Hf atoms.

The contribution to the highest energetic optical phonon states are dominated by the two lightest atoms in the *X*NiSn-structure. For TiNiSn and ZrNiSn, the contribution are dominated by the *X* and Ni-atom; whereas, Ni and Sn shows the most contribution to DOS in HfNiSn.

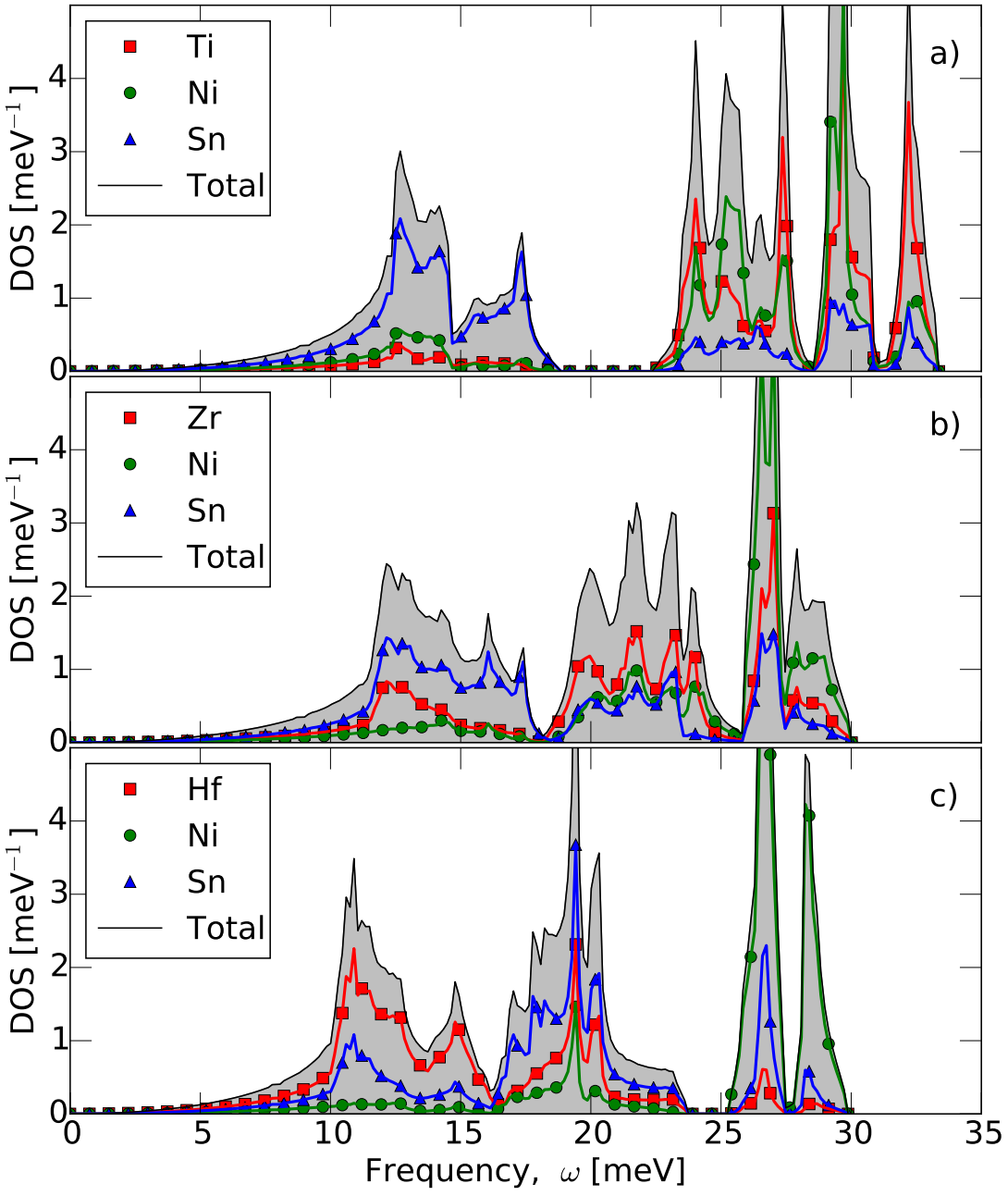

Figure 5.3: Phonon density of states and the partial DOS for a) TiNiSn, b) ZrNiSn and c) HfNiSn. The partial density of states from the *X*=Ti,Zr or Hf, Ni and Sn is shown with the squares, circles and triangles, respectively. The total density of states is shown with the black curve.

5.1.3 Heat Capacity

The heat capacity at constant volume C_V is calculated from the phonon dispersion as explained in section 2.4.2 about thermodynamics in equation (2.59). The results are normalized by the number of atoms in the conventional unit cell. The heat capacity at constant volume as a function of temperature is shown in figure 5.4 in the temperature range from 0 K to 1000 K: the inset shows the trend for C_V up to 100 K.

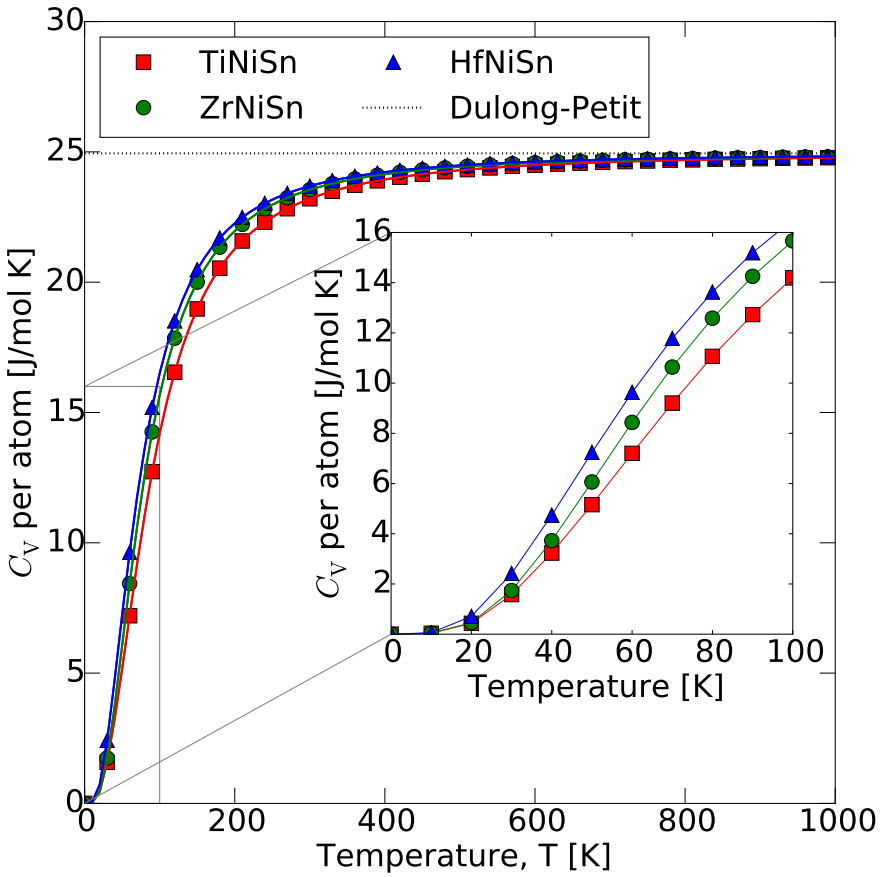

Figure 5.4: The heat capacity at constant volume as a function of temperature from zero up to 1000 K. The squares, circles and triangles are TiNiSn, ZrNiSn and HfNiSn, respectively. The inset shows the general trend for C_V when T goes from 0 to 100 K.

The heat capacity at constant volume increases when going from TiNiSn to ZrNiSn to HfNiSn. The difference in C_V is most prominent at lower temperatures, as seen in the inset of figure 5.4. The values of TiNiSn, ZrNiSn and HfNiSn at 100 K are 14.19, 15.67 and 16.51 $\mathrm{J/mol\,K}$. The trend $C_V(\mathrm{TiNiSn}) < C_V(\mathrm{ZrNiSn}) < C_V(\mathrm{HfNiSn})$ can be understood by the shift in DOS towards lower frequencies when substituting the atom

on the *X*-site with a heavier element; therefore, there are more available states at lower temperatures for the heaviest *X*NiSn half-Heusler.

The heat capacity at constant volume increases with temperature due to an increase in available states. At sufficiently high temperatures when $k_{\mathrm{B}}T >> \hbar\omega(j\mathbf{q})$, one can derive the Dulong-Petit law of $C_{\mathrm{V}} = 3N_{\mathrm{A}}k_{\mathrm{B}} = 24.94\,\mathrm{J/mol\,K}$, where N_{A} is Avogadro's constant. The value for all three *X*NiSn half-Heuslers converges towards the Dulong-Petit value, and it is illustrated as the dotted line in figure 5.4. At 2000 K, the calculated C_{V} differs by $\pm 0.04\ \mathrm{J/mol\,K}$ from the Dulong-Petit value.

5.2 Thermal Transport

5.2.1 Anharmonic Relaxation Times

Harmonic phonon vibrations does not interact with each other, and the thermal conductivity will be infinite; thus, describing the phonon interactions are a necessity to get a finite lattice thermal conductivity. Phonon-phonon scattering rates may be obtained by including higher ordered terms from the Taylor expansion of the potential energy. For three-phonon scattering events, the third-order force constants are taken into consideration. The inverse relaxation times due to three-phonon scattering are shown in figure 5.5. The peaks correspond to scattering events with a low relaxation time, and the peaks are shifted towards lower frequencies due to the lowering of phonon modes when going from Ti to Zr to Hf on the *X*-site. In fact, the peaks are placed close to the middle of the frequency range, which can be understood by the conservation of energy.

In three-phonon interactions, each phonon has their own energy ω, ω' and ω'' and their own wave vector $\mathbf{q}$, $\mathbf{q}'$ and $\mathbf{q}''$. Allowed scattering events requires the conservation of both energy and momentum, which are explained in section 2.6.1 about three-phonon interactions. Considering the annihilation of two phonons and creation of one phonon: the two initial phonons must have an energy equal to the final phonon. At what frequencies the three-phonon scattering events takes place are limited by the phonon dispersion. Further, conservation of momentum of the three phonons is also required, and the phonon dispersion restricts where in the first Brillouin zone the three-phonon scattering events takes place. It is expected that the scattering events are not uniformly distributed within the first Brillouin zone due to the conservation of both energy and momentum.

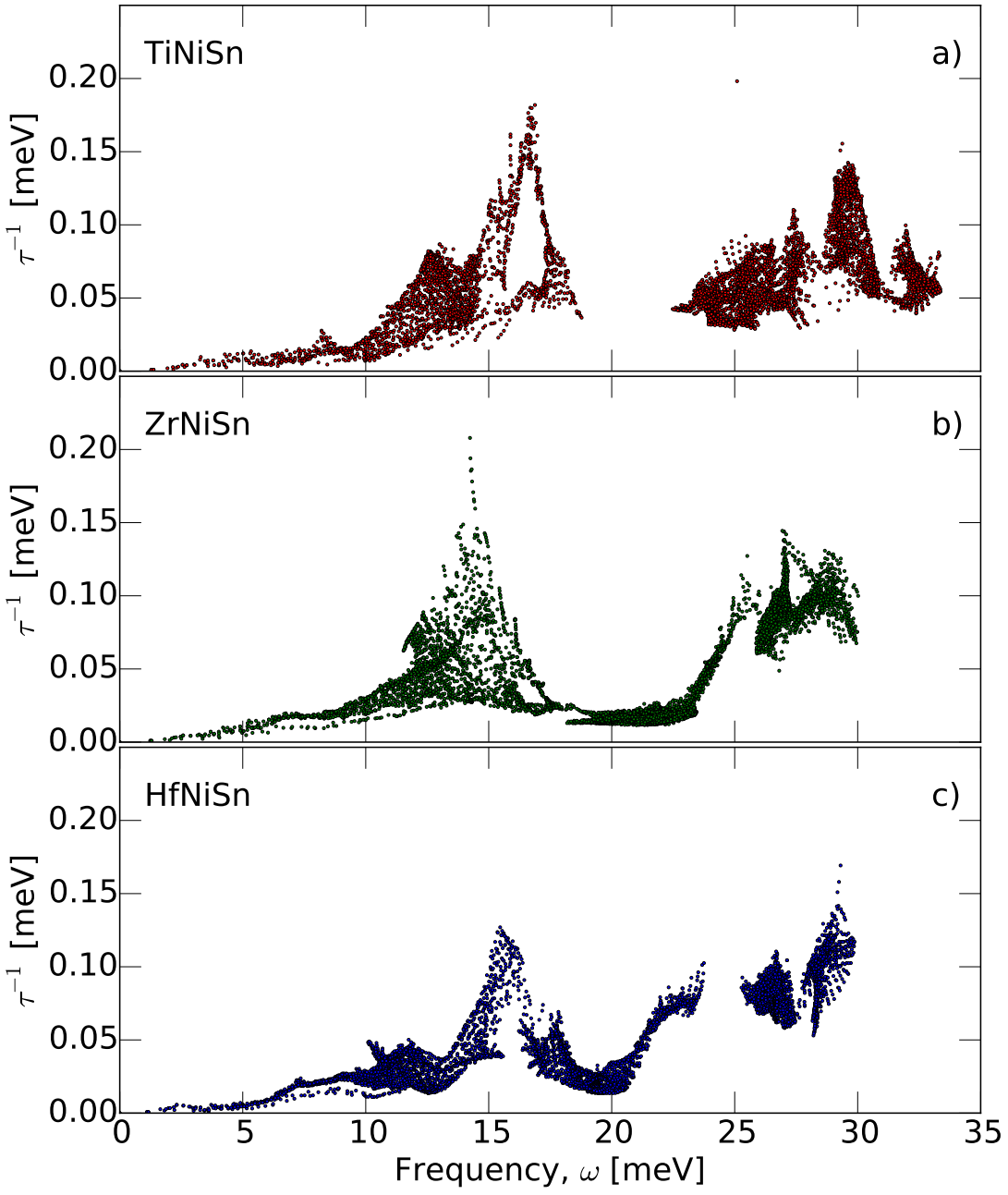

Figure 5.5: The inverse relaxation times for anharmonic three-phonon interactions in a) TiNiSn, b) ZrNiSn and c) HfNiSn as a function of phonon frequencies.

5.2.2 Lattice Thermal Conductivity

Lattice thermal conductivity may be calculated by solving the Boltzmann transport equation for phonons within the relaxation time approximation. We have all the ingredients to calculate the lattice thermal conductivity as described in equation (2.70) from section 2.5 about thermal conductivity. The calculated κ_l for the pure TiNiSn, ZrNiSn and HfNiSn is shown as functions of temperature in figure 5.6, where T goes from 300 K to 1000 K. At $300\mathrm{K}$, we obtains a κ_l of 14.5, 16.7 and $15.3\mathrm{W/mK}$ for TiNiSn, ZrNiSn and HfNiSn, respectively. Figure 5.6 shows the trend $\kappa_l(\mathrm{ZrNiSn}) > \kappa_l(\mathrm{HfNiSn}) > \kappa_l(\mathrm{TiNiSn})$ in the whole temperature range, with the greatest difference at lower temperatures. Lattice thermal conductivity decreases as a function of temperature and is less temperature dependent at higher temperatures due to the increase of anharmonicity. Higher temperatures increases the phonon population at higher frequencies; therefore, there will be more phonons which can participate in the three-phonon interactions.

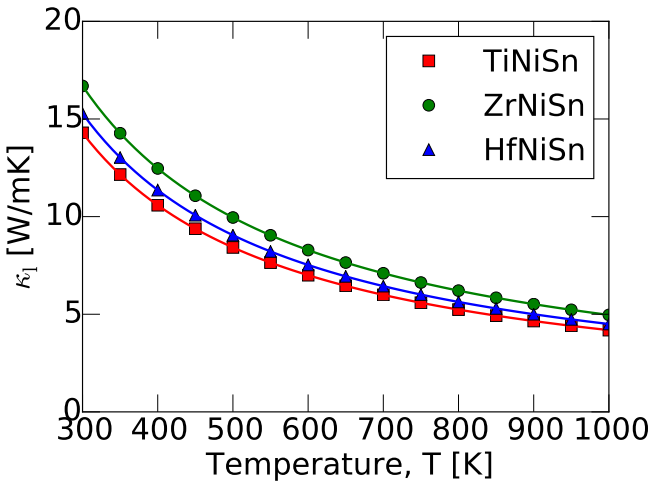

Figure 5.6: Lattice thermal conductivity for bulk *X*NiSn where the squares, circles and triangles represents TiNiSn, ZrNiSn and HfNiSn, respectively.

The acoustic and optical phonons do not carry the same amount of heat. Cumulative lattice thermal conductivity as a function of frequency, and its derivative, at 300 K is shown in figure 5.7a) and 5.7b) for the pure *X*NiSn half-Heuslers. The total accumulation of κ_l increases as a function of the frequency throughout the whole frequency spectrum: all phonons contributes to heat resistivity.

The plateau in figure 5.7a) for TiNiSn in the frequency range 17-23 meV represents the acoustic-optical gap. The optical phonons contributes less than 2 W/mK to lattice thermal conductivity for all three *X*NiSn half-Heuslers. The cumulative κ_l for ZrNiSn

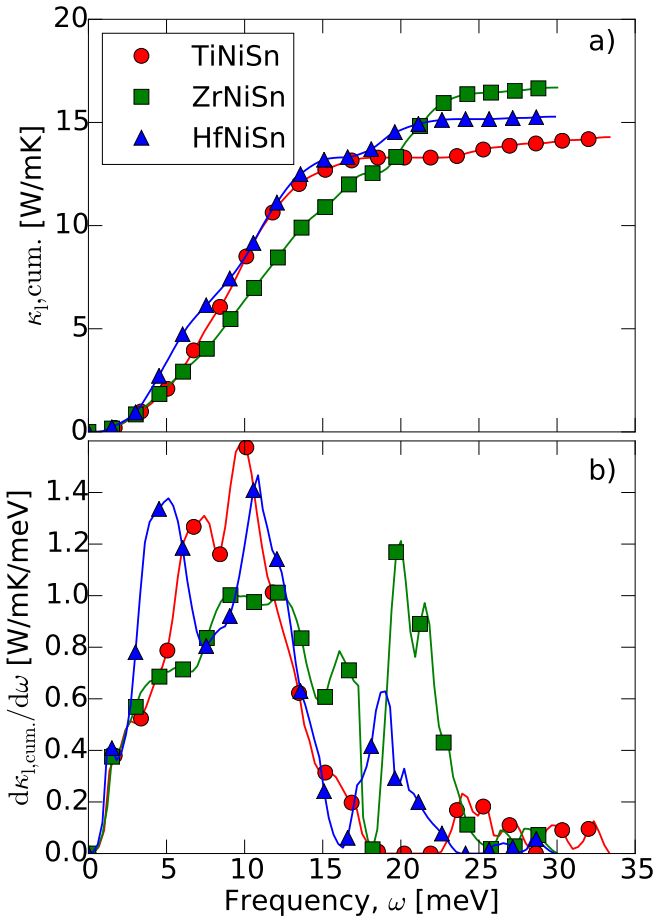

Figure 5.7: The cumulative lattice thermal conductivity is shown as a function of frequency for a) TiNiSn (circles), ZrNiSn (squares) and HfNiSn (triangles) at 300 K. Figure b) represents the derivative of the cumulative κ_l.

in figure 5.7a) increases evenly up to 25 meV. However, there is a small plateau at ~ 17 meV, which is the region in the dispersion where the lower optical branches and the acoustic branches barely overlap. The upper three optical branches contributes with < 1 W/mK to the lattice thermal conductivity; whilst, the acoustic phonons and the optical phonons from the three lower branches have similar contribution to the κ_l. The acoustic phonons in HfNiSn are the major heat carriers at room temperature, as seen in figure 5.7a) and the derivative in figure 5.7b). The cumulative κ_l for HfNiSn increases slightly faster compared to ZrNiSn and TiNiSn, illustrated by the small "bump" (triangles) in figure 5.7a) at frequencies between 5 and 10 meV. It can be understood from the lower acoustic phonon branches and the shift of DOS towards lower frequencies; thus, the most prominent heat carriers are located at lower frequencies in the heavier HfNiSn

half-Heusler. The optical phonons from the lower three optical branches contributes with $\sim$ 2 W/mK to κ_l, where the phonons from the upper three optical branches have a contribution $<$ 1 W/mK. As mentioned in section 5.1.2, the majority of the states in the acoustic region in HfNiSn stems from the motions of the Hf-atoms; thus, it becomes apparent that substitution on the Hf-site in HfNiSn will have a big impact on lattice thermal conductivity.

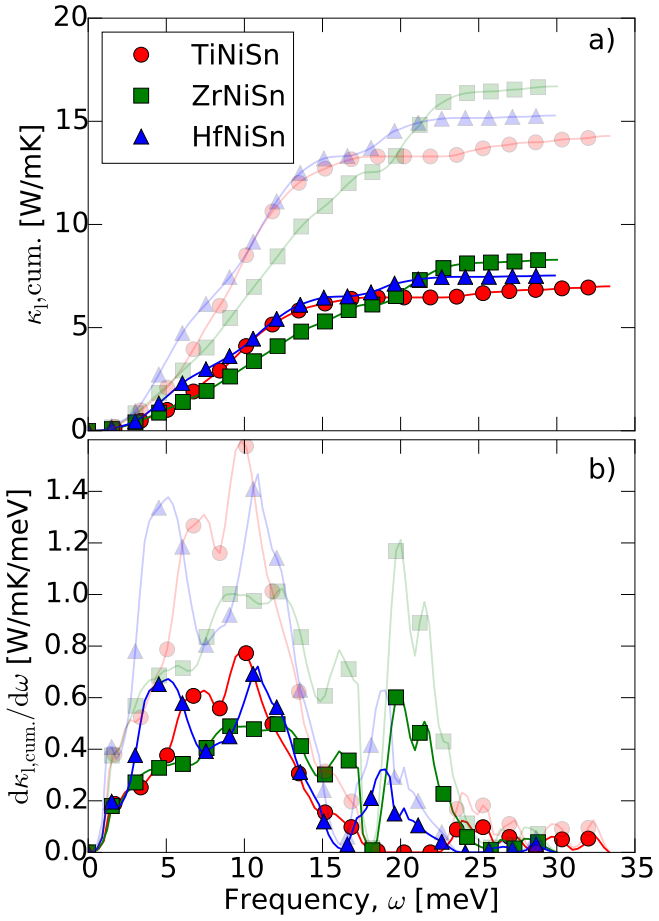

Figure 5.8: The cumulative lattice thermal conductivity is shown in a) as a function of frequency for TiNiSn (circles), ZrNiSn (squares) and HfNiSn (triangles) at 600 K. Figure b) represents the derivative of the cumulative κ_l. For comparison, the cumulative κ_l at 300 K for the same compositions are illustrated as the shaded curves.

At 600 K, the cumulative κ_l in figure 5.8a) shows an increase in the whole frequency range; still, the majority of the heat carriers are the acoustic phonons for all three TiNiSn, ZrNiSn and HfNiSn half-Heuslers. However, the contribution from the acoustic phonons at 600 K is considerable lower compared to the case at 300 K. There is almost a 50%

reduction of the acoustic heat carriers at 600 K compared to the case at 300 K which is seen in the maxima for the derivative of the cumulative κ_l in figure 5.8b) and 5.7b). Higher temperature increases the anharmonicity of the crystal; thus, more three-phonon scattering events takes place and a lower lattice thermal conductivity is expected.

5.3 Isoelectronic Substitution

5.3.1 Virtual Crystal Approximation

Introducing mass-disorder on the *X*-site breaks the symmetry. The frozen phonon approach utilizes symmetries in the crystal to reduce the number of displacements; thus, calculations of the force constants in an alloy with disorder becomes very computationally expensive because of the increase in number of displacements. Accounting for the scattering from mass-disorder is done within the virtual crystal approximation to effectively reduce the computational costs.

Keeping the mass constant on the *X*-site while changing the obtained forces from the first principles calculations for pure TiNiSn, ZrNiSn and HfNiSn shows similarities between DOS which suggests similarities between the force constants as shown in figure 5.9a-c). Also, the inverse relaxation time from anharmonic scattering show similarities between the forces obtained from the first principles calculations, and the results are shown in figure 5.9d-f). The virtual crystal approximation considers mass-disorder as a perturbation where the changes in the forces are neglected; however, the similarities in the force constants between the pure TiNiSn, ZrNiSn and HfNiSn makes VCA more applicable.

The differences between the DOS plots in the acoustic region is very small, and figure 5.9b) and 5.9c) suggests that ZrNiSn and HfNiSn exhibit similar force constants. This is somewhat expected due to the similarities in the atomic radii between Zr ($r_{\mathrm{Zr}} = 206$ pm) and Hf ($r_{\mathrm{Hf}} = 208$ pm). Also, the electronegativity for Zr and Hf are the most similar compared to Ti. The electronegativity in Ti, Zr and Hf is 1.53, 1.33 and 1.3, respectively; thus, it is expected that Zr and Hf makes more similar bonds to the neighboring atoms in the crystal. Similar calculations can be done keeping the mass constant for either Zr or Hf while changing the forces, and the DOS are quite similar also in the case of constant Zr or constant Hf.

A similar test may be performed for the third-order force constants. Again, the mass at the *X*-site is held constant with Ti mass, while varying the third-order force constants between the pure *X*NiSn half-Heuslers obtained from the first principles calculations. The result is shown in figure 5.9d-f). The spread of relaxation times in figure 5.9e) and

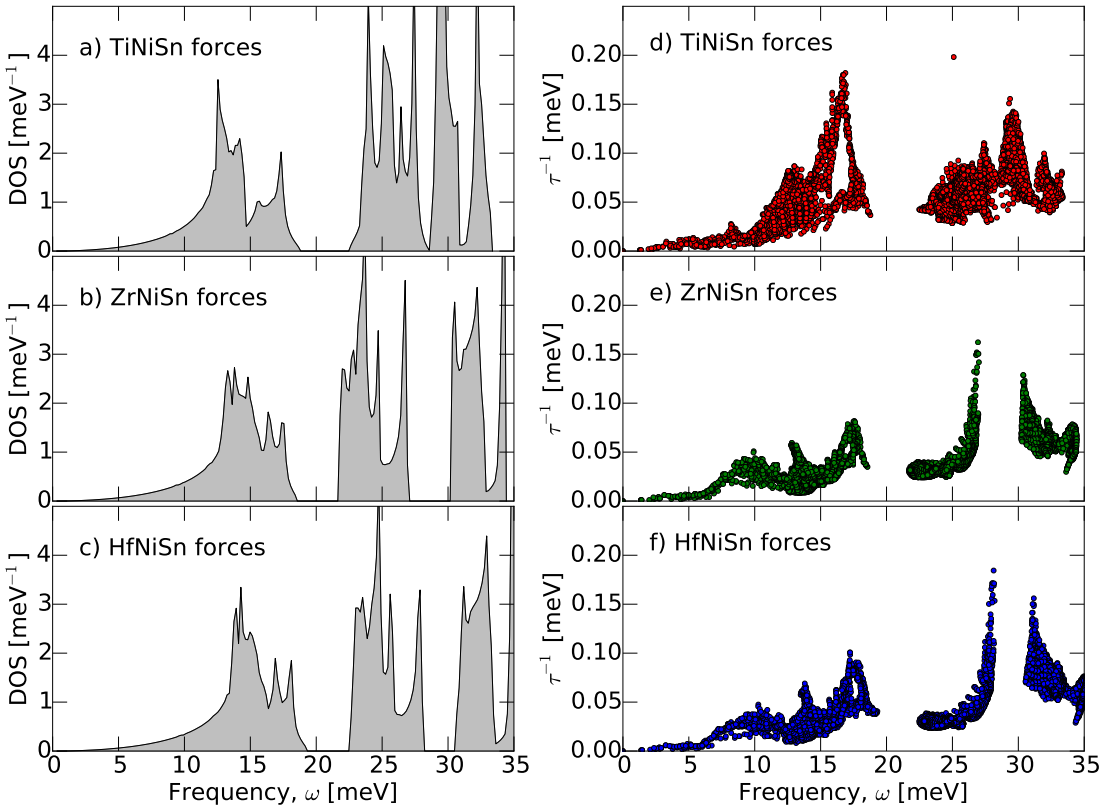

Figure 5.9: Density of states and the inverse τ for anharmonic scattering within the VCA: the mass on the X-site is held fixed at Ti mass, while changing the second- and third-order force constants. The calculated DOS with varying second-order forces are shown in figure a-c) for TiNiSn-, ZrNiSn- and HfNiSn forces, respectively. The inverse τ with varying third-order forces are shown in figure d-f) for TiNiSn-, ZrNiSn- and HfNiSn forces, respectively.

5.9f) as a function of frequency suggests that ZrNiSn and HfNiSn have more similar third-order forces, as compared to the distribution in figure 5.9d) for TiNiSn forces. Similar comparisons can be done for the inverse relaxation times with the third-order force constants with constant Zr- or Hf mass.

5.3.2 Optimal Alloying

Binary Substitution

Alloying on the X-site has proven to reduce κ_l [21, 23, 26–31]. To gain a better understanding of the role of the mass-disorder, the binary substitution on the X-site is considered. The inverse relaxation times from mass-disorder scattering are proportional

to the mass-variance parameter, $1/\tau^{\mathrm{md}_{j\mathbf{q}}} \propto M_{\mathrm{var}}(\mathbf{b})$, and it defines which degree the alloying contributes to scattering from mass-disorder. The mass-variance parameter is defined as $M_{\mathrm{var}}(\mathbf{b}) = \sum_i f_i(\mathbf{b})(1 - [m(\mathbf{lb})/\bar{m}(\mathbf{b})])^2$ [46, 47], where f_i is the concentration of the species i, $m(\mathbf{lb})$ is the mass of the bth atom in the lth unit cell and $\bar{m}(\mathbf{b})$ is the average mass of atom $\mathbf{b}$. Relaxation times from mass-disorder scattering $1/\tau^{\mathrm{md}}_{j\mathbf{q}}$ is combined with the anharmonic relaxation times $1/\tau^{\mathrm{anh}}_{j\mathbf{q}}$ before calculating the lattice thermal conductivity.

The mass-variance parameter as a function of alloy concentration on the *X*-site for (Ti,Zr)NiSn, (Ti,Hf)NiSn and (Zr,Hf)NiSn is shown in figure 5.10. There are specific values where the mass-variance parameter is the greatest. The mass-variance parameter in the case of 80% Ti and 20% Hf is 5 times greater than 70% Ti and 30% Zr and 4 times greater than 70% Zr and 30% Hf.

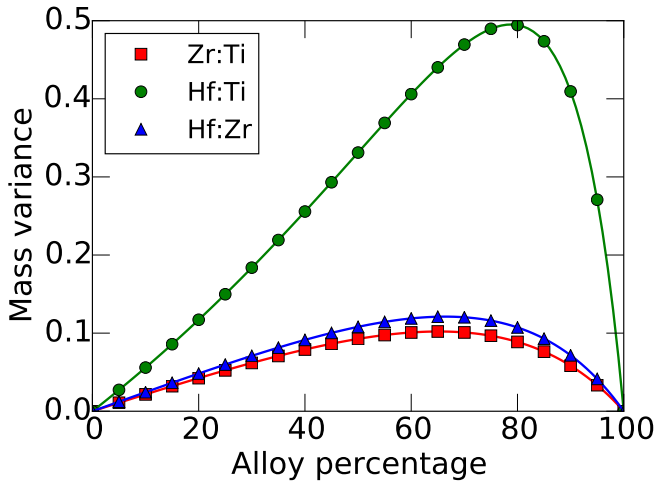

Figure 5.10: Mass-variance parameter as a function of binary alloy percentage. The binary substitution pair is indicated as squares for Zr:Ti, circles for Hf:Ti and triangles for Hf:Zr.

The occurrence of the highest mass-variance parameter can be understood by considering the mass-ratio difference, which is largest for the alloys containing Ti and Hf on the *X*-site. In order to minimize lattice thermal conductivity, the virtual crystal should be as light as possible, but still contain high enough concentration of Hf in order to have a significant contribution to the mass-disorder scattering. Considering an alloy in the optimal case with 80% Ti and 20% Hf; introducing Zr on the Ti-site will make the virtual crystal heavier which results in lower scattering effects, and by substituting Hf with Zr results in lower scattering effects due to the removal of the Hf contribution to mass-disorder in the crystal. Either way, the mass-variance parameter will decrease and the

relaxation times from mass-disorder scattering will increase; therefore, lattice thermal conductivity will increase.

The theory captures the expected U-shape for lattice thermal conductivity versus the percentage of alloying with a binary substitution at the X-site. Similar calculations of κ_l versus alloy concentration for Si-Ge-alloys have been reported to reproduce the experimental results [70–72]. The resulting κ_l as a function of alloy percentage in Hf:Ti, Zr:Ti and Hf:Zr at the X-site is given in figure 5.11a-c). An interpolation between κ_l with respect to the composition has been done. The lattice thermal conductivity drops drastically with an alloy percentage between 0-10% at 300 K; however, the change in κ_l becomes relative small with an alloy percentage in the range 20-80%. The lattice thermal conductivity becomes less sensitive to mass-disorder scattering at 600 K and 900 K, as observed earlier for κ_l as a function of temperature for pure TiNiSn, ZrNiSn and HfNiSn.

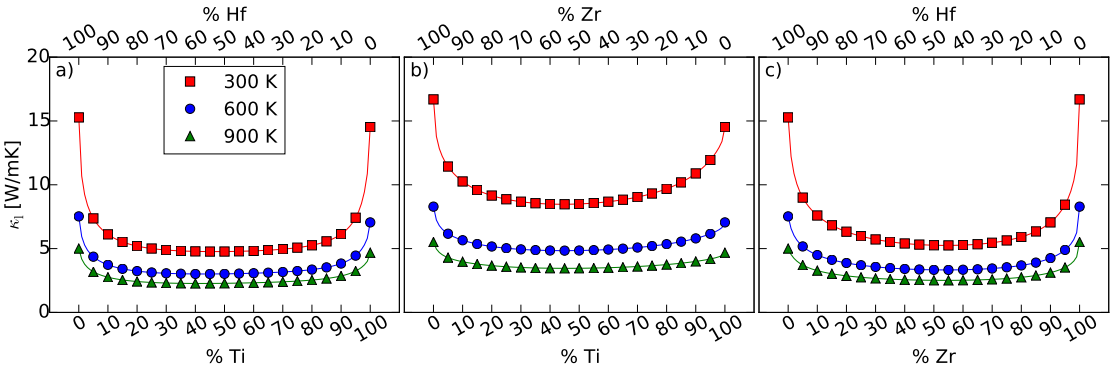

Figure 5.11: Lattice thermal conductivity as a function of alloy percentage for a binary substitution on the X-site, for a) Hf:Ti, b) Zr:Ti and c) Hf:Zr. The squares, circles and triangles represents κ_l at 300 K, 600 K and 900 K, respectively.

Ternary Substitution

The relaxation times from mass-disorder scattering with ternary substitutions on the X-site is calculated for the composition $Ti_xZr_yHf_{1-x-y}NiSn$, where $x, y = 0.1, 0.2, \cdots, 1.0$ and $x + y \leq 1$. Lattice thermal conductivity for $Ti_xZr_yHf_{1-x-y}NiSn$ is mapped in the ternary diagrams in figure 5.12 at 300 K and figure 5.13 at 600 K. The diagrams a-c) in said figures are calculations of κ_l with pure TiNiSn-, ZrNiSn- and HfNiSn forces, respectively. The lattice thermal conductivity are then interpolated with respect to the composition, and the interpolated κ_l at 300 K and 600 K are given in figure 5.12d) and 5.13d), respectively. Note that the scale for lattice thermal conductivity at 300 K goes from 2-12 W/mK; whereas, the scale at 600 K goes from 2-6 W/mK.

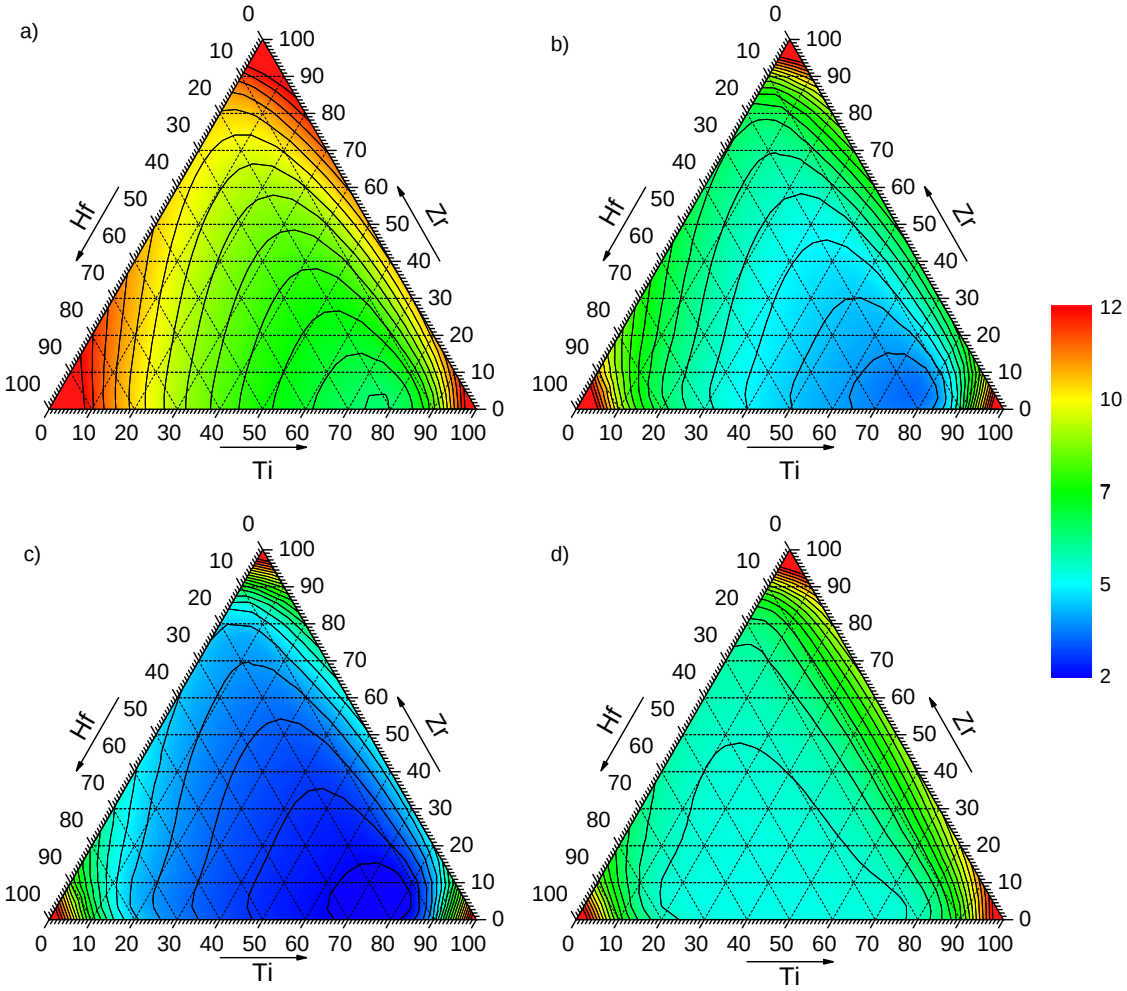

Figure 5.12: Lattice thermal conductivity mapped for the whole $Ti_xZr_yHf_{1-x-y}NiSn$ at 300 K. The bottom right, top and bottom left corner of the diagrams correspond to 100% Ti, Zr and Hf, respectively. Figure a-c) is the calculated κ_l with TiNiSn forces, ZrNiSn forces and HfNiSn forces, respectively. Figure d) is κ_l with an interpolation between κ_l with respect to the composition.

The highest κ_l is observed at the corners of the ternary diagrams with zero percentage of alloying. The optimal alloy percentage in 5.12a-c) and 5.13a-c) is 80% Ti and 20% Ti, which is related to the mass-variance parameter. However, the interpolated result in figure 5.12d) and 5.13d) shifts the minimum to an alloy percentage of $50/50$ between Ti and Hf on the *X*-site, which is a result of the different effect of alloying when using pure TiNiSn, ZrNiSn and HfNiSn. The different effects of alloying on κ_l are observed by the difference in the color map. The broader, blue area in figure 5.12c) is related to cumulative κ_l, where substitution the Hf-site reduces the acoustic heat carriers.

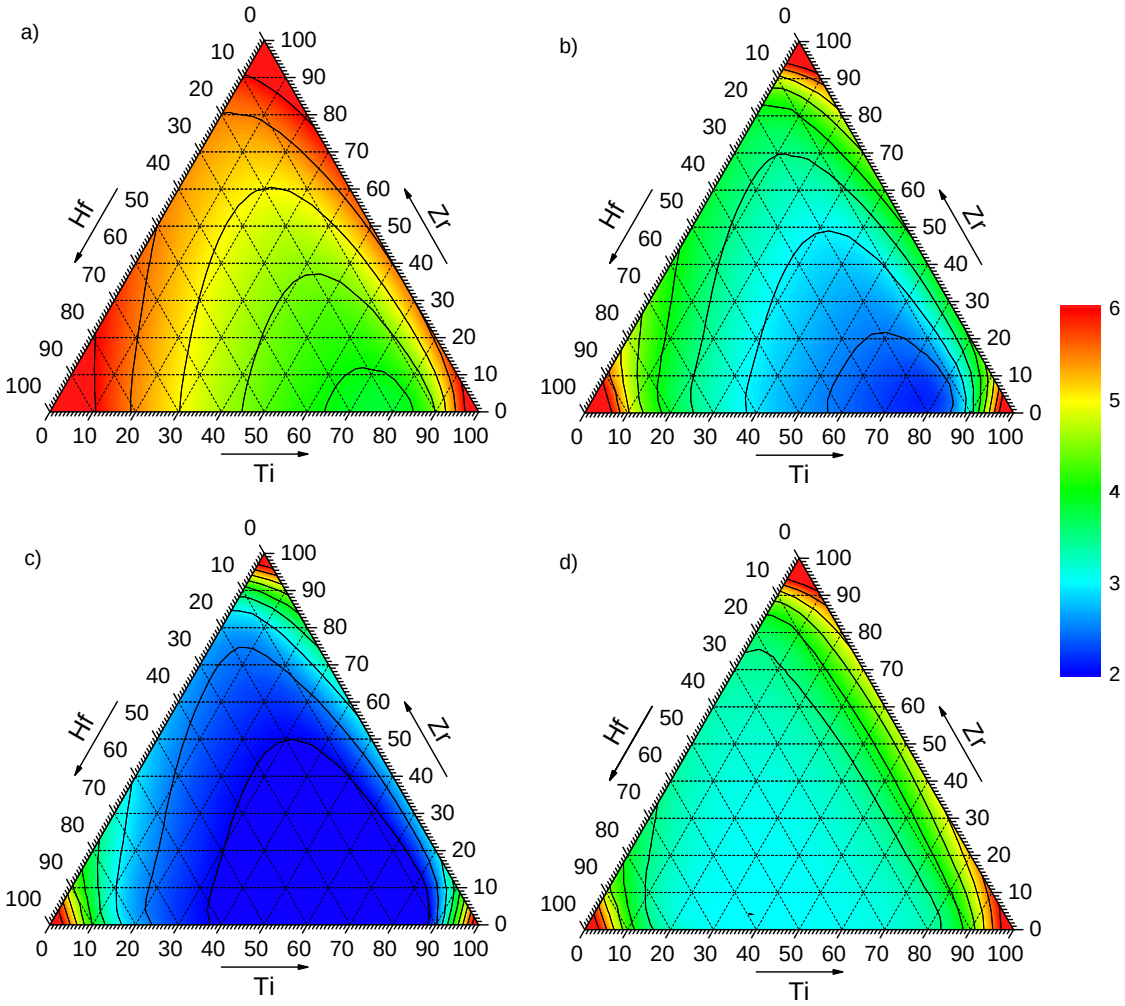

Figure 5.13: Lattice thermal conductivity mapped for the whole $Ti_xZr_yHf_{1-x-y}NiSn$ at 600 K. The bottom right, top and bottom left corner of the diagrams correspond to 100% Ti, Zr and Hf, respectively. Figure a-c) is the calculated κ_l with TiNiSn forces, ZrNiSn forces and HfNiSn forces, respectively. Figure d) is κ_l with an interpolation between κ_l with respect to the composition.

5.4 Smaller Grains for a Low Lattice Thermal Conductivity

A binary or ternary substitution on the *X*-site in a *X*NiSn Half-Heusler scatters the phonons at higher frequencies. Thus, the main heat carriers in such alloys are the phonons at lower frequencies, which are particularly sensitive to scattering from grain boundaries. Further reduction of κ_l in *X*NiSn alloys can be achieved by considering scattering from grain boundaries, as presented in equation (2.93). The inverse relaxation times from boundary scattering is inversely proportional to frequency; therefore, scattering from grain boundaries will mainly affect the acoustic phonons. Figure 5.14 shows κ_l as a function of the grain size at three different temperatures for the TiNiSn Half-Heusler alloy.

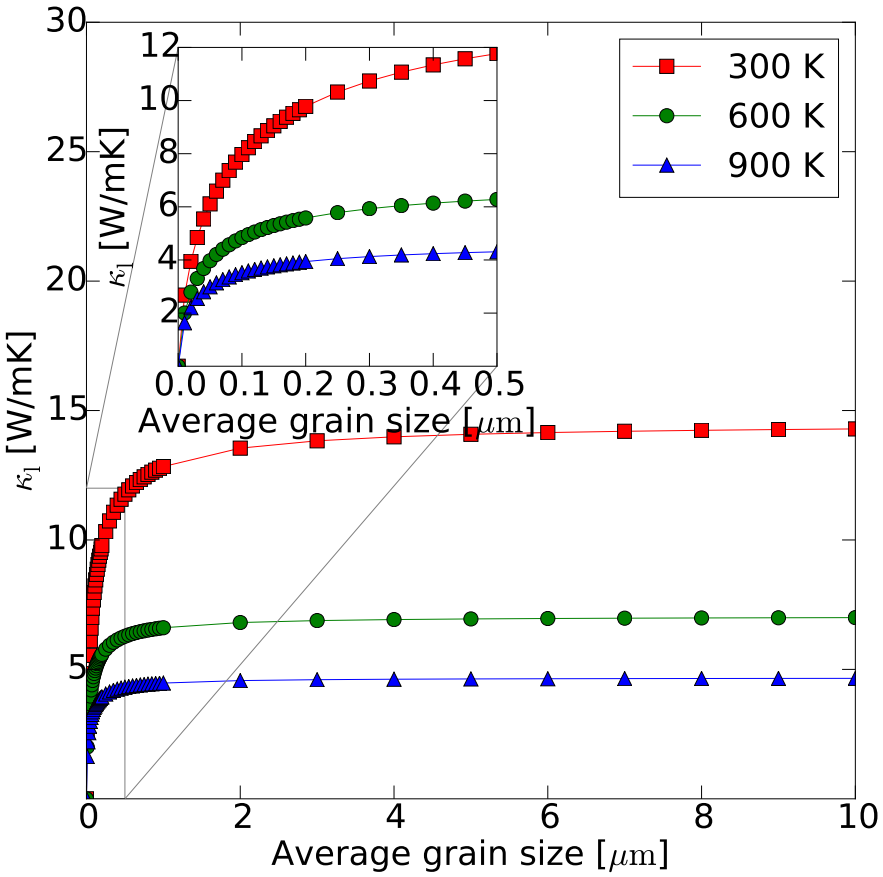

Figure 5.14: Lattice thermal conductivity as a function of grain size at 300 K, 600 K and 900 K for the TiNiSn Half-Heusler alloy.

The grain size dependence of κ_l is most prominent at grain sizes $L \leq 2\ \mu\mathrm{m}$ for all temperatures. The largest reduction in κ_l is observed at lower temperatures. This may be related to the smaller phonon population at lower temperatures; thus, the grain boundaries have more phonons to scatter. The small change in κ_l at larger grain sizes stems from the phonons with the highest group velocity which are the acoustic phonons near the zone center. It can be directly related to the scattering model for grain boundaries, where $1/\tau^{\mathrm{bs}_{j\mathbf{q}}} = v_{j\mathbf{q}}/L$. The choice of the parameter L will be discussed in the section 6.2.4 about calculations of low lattice thermal conductivity based on relevant grain sizes.

Chapter 6

Discussion and Analysis

6.1 Calculations of Low Lattice Thermal Conductivity

The lattice thermal conductivity for pure TiNiSn, ZrNiSn and HfNiSn based on the first principles calculations in this study is too high to be applicable for thermoelectric applications: the calculated κ_l is around five times higher than commercial Bi_2Te_3 [20]. A more thorough comparison of the κ_l to the literature, both experimental and theoretical studies, is conducted in the next section.

The half-Heuslers TiNiSn, ZrNiSn and HfNiSn show similar structure in the phonon dispersion; however, a heavier atom at the *X*-site lowers the frequencies. The atomic specific contribution to density of states from the *X*-, Ni- and Sn-atoms is significantly different. Comparing the density of states for the three TiNiSn, ZrNiSn and HfNiSn half-Heuslers, one can see a large contribution from the Hf-atoms to the acoustic phonon states, whereas TiNiSn and ZrNiSn have their main contribution in this region from the Sn-atoms. From the cumulative lattice thermal conductivity, the acoustic phonons with frequencies lower than 15 meV are the majority heat carriers in all three of the pure half-Heuslers in this study. Therefore, it is expected that a substitution on the *X*-site will have a big effect for HfNiSn, which will result in a removal of the available states for the acoustic phonons and increase the number of states at higher frequencies. The bigger effect on the κ_l for HfNiSn can be observed by the broader, blue area in the ternary diagrams in figure 5.12c). The alloying in TiNiSn and ZrNiSn has shown a significant reduction in lattice thermal conductivity; therefore, one cannot consider the direct removal of the acoustic heat carriers as the main source for the reduction in κ_l.

The conservation of energy and momentum limits where in the first Brillouin zone an anharmonic scattering event can take place. If a phonon with a large wave vector takes part in a coalescence process with another phonon with a large wave vector, it would re-

quire a phonon with a short wave vector to conserve momentum. With respect to energy conservation, an ideal case would exhibit a phonon dispersion which has the acoustic phonon branches in a frequency range exactly half of the upper optical branches. At the same time, the lower optical phonon branches should barely overlap with both the acoustic region and the upper optical region. This kind of dispersion will increase the possible three-phonon scattering events; coalescence and decay processes will be energetically possible in the whole frequency range. Also, this situation will make it possible for a coalescence process for all of the acoustic heat carriers with other phonons resulting in a scattering of the majority heat carriers to higher energetic states. This is beneficial to reduce κ_{l} because the phonons in the optical bands contribute less to heat conduction, seen from the cumulative κ_{l}. Therefore, the structure of the dispersion will limit where in the first Brillouin zone a scattering event can take place due to conservation of the energy and momentum.

The isoelectronic substitution on the *X*-site within the virtual crystal approximation has shown a significant reduction in lattice thermal conductivity, especially for alloy percentages over 10% on the *X*-site. The κ_{l} as a function of binary alloy percentage in figure 5.11 shows small changes in the κ_{l} when the alloy percentage is in the range 20-80$\%$: these findings suggests that the scattering from mass-disorder are mostly utilized when alloying with 20% on the *X*-site. The mass-disorder scattering are expected to efficiently scatter phonons at higher frequencies, and this is directly related to the expression for the relaxation time from mass-disorder scattering where $1/\tau_{j\mathbf{q}}^{\mathrm{md}} \propto \omega^4(j\mathbf{q})$. In contrast, grain boundaries scatters the lower energetic phonons. The relaxation times for grain boundary scattering have the following frequency dependence, $1/\tau_{j\mathbf{q}}^{\mathrm{bs}} \propto \omega^{-1}(j\mathbf{q})$. The grain size must be less than 2 $\mu\mathrm{m}$ to have a significant impact on the κ_{l}, which is shown in figure 5.14 with κ_{l} as a function of grain sizes.

Combining the anharmonic, mass-disorder and grain boundary scattering results in a low lattice thermal conductivity. From section 5.3.2 about optimal alloying, we know that the composition $Ti_{0.5}Hf_{0.5}NiSn$ shows a big reduction in κ_{l}. Combining the scattering from mass-disorder in the composition $Ti_{0.5}Hf_{0.5}NiSn$ with the scattering from grain boundaries results in an low κ_{l}. Lattice thermal conductivity as a function of temperature is shown in figure 6.1 for the pure TiNiSn and HfNiSn; as well as the composition $Ti_{0.5}Hf_{0.5}NiSn$ with and without grain boundary scattering. There is not any new physics here, which has not been discussed. The onset of new scattering mechanisms reduces the lattice thermal conductivity, and the κ_{l} becomes less temperature dependent. A reduction of the κ_{l} is observed when increasing the temperature. This is related to the increased anharmonicity at higher temperatures.

A demonstration that the mass-disorder scattering and grain boundary scattering af-

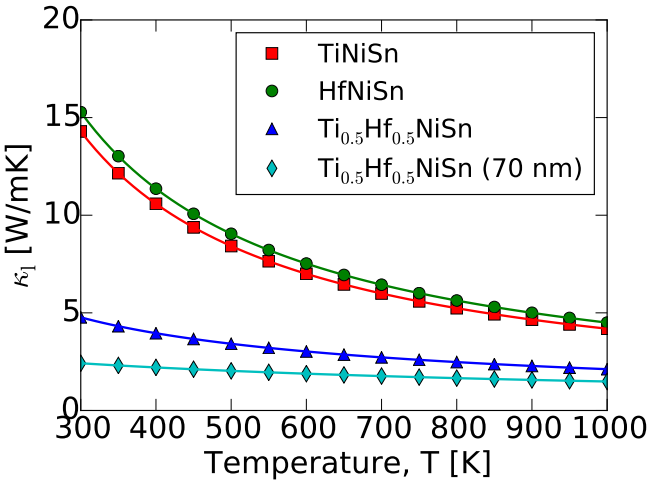

Figure 6.1: The lattice thermal conductivity as a function of temperature. Pure TiNiSn and HfNiSn are shown as squares and circles, respectively. A reduction in κ_l is observed when including scattering from mass-disorder, and the triangles represent the κ_l for $Ti_{0.5}Hf_{0.5}NiSn$. Further reduction is achieved including scattering from grain boundaries, shown with the diamonds.

fects phonons at different frequencies is shown in figure 6.2. The cumulative lattice thermal conductivity for pure TiNiSn and $Ti_{0.5}Hf_{0.5}NiSn$ with and without grain boundary scattering is considered. The acoustic phonons are the main contributors to heat conduction in pure TiNiSn (diamonds). The derivative of the cumulative κ_l for TiNiSn shows that the onset of grain boundary scattering with an average grain size of 70 nm (triangles) scatters all acoustic phonons to some degree; whilst, the optical phonons are unaffected. Therefore, one observes a large reduction in κ_l because grain boundaries scatters the heat carriers with the most contribution to heat conduction.

The mass-disorder in $Ti_{0.5}Hf_{0.5}NiSn$ without boundaries (circles) scatter all phonons above 5 meV. The effects on the κ_l from mass-disorder scattering increases at higher frequencies, which are in accordance with the ω^4 dependence. The onset of boundary scattering with 70 nm (stars) reduces the κ_l even further because the boundaries scatters the phonons in the low-acoustic region which is the frequency region where the mass-disorder does not scatter the phonons efficiently.

These observations confirms the theory about frequency dependence: mass-disorder are the most effective at higher frequencies and grain boundary scattering are the most effective at lower frequencies. From cumulative κ_l in figure 6.2, one can see that both scattering mechanisms scatters the phonons in the frequency range 5-12 meV.

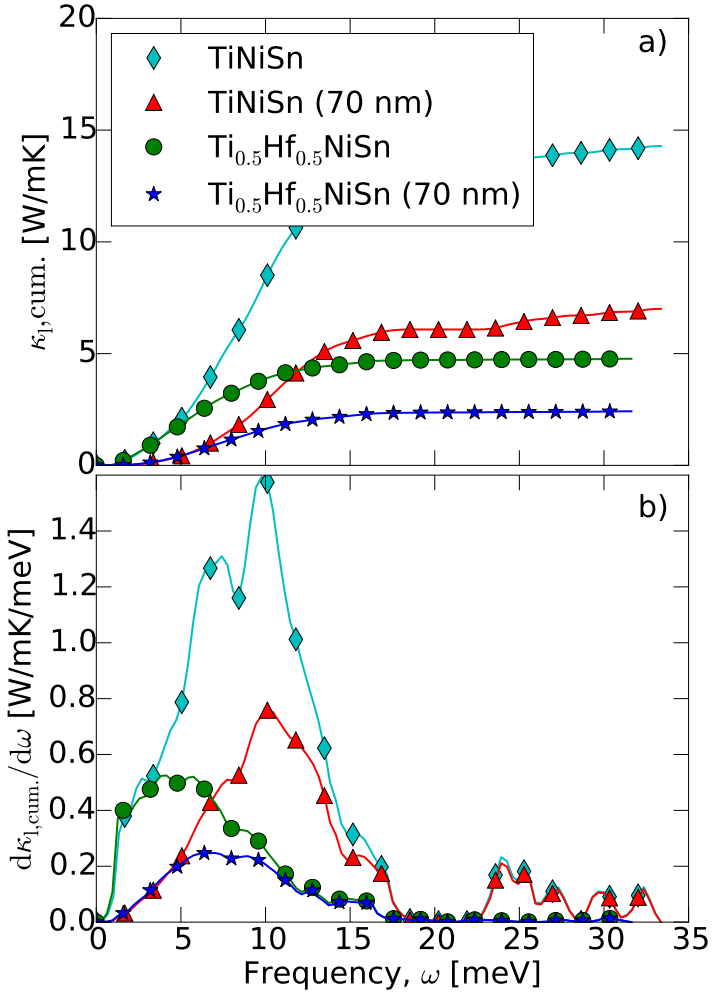

Figure 6.2: Illustration of the effect of mass-disorder and grain boundary scattering. The cumulative κ_l is given in a) and its derivative in b) as a function of frequency. Pure TiNiSn with and without grain boundary scattering are is shown as diamonds and triangles, respectively. The composition $Ti_{0.5}Hf_{0.5}NiSn$ with and without grain boundary scattering is shown as circles and stars, respectively.

6.2 Comparison Between Theory and Experiments

6.2.1 Bulk Properties of Pure *X*NiSn Half-Heuslers

There are in total four phonon branches at the Γ-point: the acoustic modes go to zero as one approach the Γ-point and the transverse-optical branches are degenerated. The vibrational properties from theoretical calculations in this study and the experimental

values from [73, 74] are presented in table 6.1 at the zone-center. The experimental values are obtained from Raman and infrared spectroscopy, and the experiments were conducted at two different temperatures: at 80 K and 300 K. The values in the parentheses are from the experiments at 300 K. There are a negligible frequency difference between the $\mathrm{TO}-\mathrm{LO}$ branches; however, the $\mathrm{TO}'-\mathrm{LO}'$ shows a significant gap in the frequency. The splitting of the higher energetic $\mathrm{TO}'-\mathrm{LO}'$ is in the order of 3-4 meV. This trend matches the behavior from the experimental studies. All of the calculated phonon dispersions for pure *X*NiSn agrees well with previous theoretical studies on the same materials [67, 75, 76].

Table 6.1: The calculated phonon frequencies in meV at the zone center in comparison with experimental values from [73, 74]; the experimental results are obtained with Raman and infrared spectroscopy. The experiments conducted in [74] at 80 K; the experiments in [73] at 300 K, which are the values given in the parentheses.

	TiNiSn				
Phonon branch	Theory	Raman		IR	
TO	26.443	27.277	(27.524)		(27.624)
LO	26.461				(27.673)
TO'	29.647		(31.492)	32.980	(31.864)
LO'	33.818	35.212		36.203	(35.645)

	ZrNiSn			
Phonon branch	Theory	Raman		IR
$\mathrm{T_1O}$	23.447		(24.946)	(24.673)
LO	23.451			(24.958)
$\mathrm{T_1O}'$	26.997		(29.384)	(29.012)
LO'	30.281			(32.236)

	HfNiSn				
Phonon branch	Theory	Raman		IR	
$\mathrm{T_1O}$	20.409	21.697	(20.953)	21.325	(21.697)
LO	20.674			22.069	(21.821)
$\mathrm{T_1O}'$	27.095	28.888	(28.640)	29.632	(29.508)
LO'	29.984	31.616		32.484	(31.368)

To date, there are no experimental studies of the anharmonic relaxation times; however, a similar theoretical study of anharmonic relaxation times and lattice thermal con-

ductivity for the pure *X*NiSn half-Heuslers has been performed by Andrea et al. [66]. The inverse relaxation times in this study from the three-phonon interactions show qualitative similarities to the obtained values in their study. They illustrated that the inverse relaxation time in the first Brillouin zone is not evenly distributed, which are shown in figure 2 in [66]. The peaks of the inverse relaxation time in figure 5.5 from this study are in good agreement with the indicated regions of the phonon dispersion with the strongest scattering mechanisms. The placement of the region of the strongest anharmonic scattering events is in good accordance with the discussion about the role of energy and momentum conservation during a three-phonon scattering event.

Theoretical and experimental values found in the literature of κ_l are presented in table 6.2. The κ_l are all of the same order; however, the table shows a great variation in the values. On the theory part, the calculated κ_l from this study differs from what was obtained in [66]: even with the qualitative similarities in the phonon dispersion and anharmonic relaxation times. At 300 K we obtains a κ_l of 14.3, 16.7 and 15.3 $\mathrm{W/mK}$ for TiNiSn, ZrNiSn and HfNiSn; whereas, Andrea et al. calculated the κ_l at 300 K to be 15.4, 13.4 and 15.8 W/mK for TiNiSn, ZrNiSn and HfNiSn, respectively. The approach to calculate the κ_l differs in this study and theirs; we solved the BTE with help of RTA, where they solved the BTE with a direct solution as described in [77]. The setup of the DFT calculations has two different initial parameters: the sampling mesh and the magnitude of the displacements. The calculations in [66] used an amplitude of 0.01 Å with a sampling mesh of $7\times7\times7$; and, in this study a amplitude of 0.03 Åand a sampling mesh of $3\times3\times3$ was used. Due to the insensitivity of the magnitude of the displacement, as illustrated in section 4.3, the difference in the κ_l is believed to come from the different sampling meshes. Generally, a denser mesh produces more accurate calculations from first principles. The force constants may differ from this study and Andrea et al.; thus, all of the subsequent properties may also differ. As discussed in the prior section, three-phonon scattering events are strongly dependent on phonon dispersion. Although a qualitative similarity in the phonon dispersions, the fine features in the dispersions will strongly influence the conservation of energy and momentum in anharmonic scattering; thus, a difference in the lattice thermal conductivity is observed.

The calculated κ_l in this work are comparable to reported experimental values in the literature. However, the experimental values of κ_l show a great variation between the different synthesis methods, even between the same synthesis methods. The variation between the experimental measurements is believed to stem from different microstructures. Yu et al. demonstrated a decrease in the κ_l due to grain-refinement by melt-spinning [34]; thus, the microstructure plays a major role in the lattice thermal conductivity. All the experimental studies in table 6.2 reported a single-phase half-Heusler.

Table 6.2: Lattice thermal conductivities at 300 K from theory and experimental measurements with their respective method. All samples are reported to be single-phased with respect to the characterization method in the parentheses. The table is adapted from [66].

Composition	κ_l [W/mK]	Method	Ref.
TiNiSn	14.3	RTA-BTE	This work
	15.4	LBTE	[66]
	17.9	LBTE	[11]
	16.8	ML	[11]
	9.3*	AM (XRD)	[18]
	7.5	AM (SEM/XRD)	[26]
	8	AM (XRD)	[15]
ZrNiSn	16.7	RTA-BTE	This work
	13.4	LBTE	[66]
	19.6	LBTE	[11]
	17.5	ML	[11]
	8.8*	AM (XRD)	[18]
	10.1	AM/SPS (SEM/XRD/EDX)	[27]
	6.8	LM/SPS (XRD)	[78]
	5.69	LM/SPS (SEM/XRD)	[34]
	4.75	LM/MS/SPS (SEM/XRD)	[34]
HfNiSn	15.3	RTA-BTE	This work
	15.8	LBTE	[66]
	19.5	ML	[11]
	6.7*	AM (XRD)	[18]
	12	AM (XRD)	[16]
	6.3	LM/SPS (XRD)	[78]
	5.38	LM/SPS (SEM/XRD)	[34]
	4.8	LM/MS/SPS (SEM/XRD)	[34]

RTA-BTE: Relaxation time approximation - Boltzman transport equation
LBTE: Linearized Boltzmann equation
ML: Machine learning algorithm
AM: Arc melting
LM: Levitation melting
MS: Melt-spinning
SPS: Spark plasma sintering
XRD: X-ray diffraction
EDX: Energy dispersive x-ray spectroscopy
SEM: Scanning electron microscopy
Note: Entries with * represent the total thermal conductivity.

6.2.2 Effect of Alloying

Different synthesis methods of the same half-Heusler composition may yield different microstructures which can affect the measured lattice thermal conductivity. The virtual crystal approximation does not consider the multiphase behavior; therefore, whether the model captures the mass-disorder correctly cannot be concluded from a direct comparison of the measured κ_{l} between the experimental values and with the calculated κ_{l}. This section presents a rough approximation where scattering effects from microstructures can be excluded. This includes both scattering at the interface between different phases and scattering from grain boundaries. If these effects can be separated out, the comparison between theory and experiment would be much more direct.

Mathiessen's rule states that the inverse of the total relaxation times is a sum of the inverse relaxation times from the scattering mechanisms under investigation. The κ_{l} is proportional to the $\tau_{j\mathbf{q}}$, which are derived from solving the Boltzmann transport equation within the relaxation time approximation in section 2.5. In order to separate out the effect of the scattering from the boundaries, the total κ_{l} with mass-disorder and grain boundaries is written as a sum of the contributions from different scattering mechanisms

$$\frac{1}{\kappa_{\mathrm{l,tot}}} = \frac{1}{\kappa_{\mathrm{l,anh}}} + \frac{1}{\kappa_{\mathrm{l,md}}} + \frac{1}{\kappa_{\mathrm{l,bs}}}. \tag{6.1}$$

We now assume that we investigate an alloy system $X_{\mathrm{x}}X'_{\mathrm{1\text{-}x}}$NiSn, that is a mixture of the pure half-Heusler compounds XNiSn and X'NiSn. The total thermal conductivity without scattering from mass-disorder can be written as

$$\frac{1}{\kappa'_{\mathrm{l,tot}}} = \frac{1}{\bar{\kappa}_{\mathrm{l,anh}}} + \frac{1}{\kappa_{\mathrm{l,bs}}}, \tag{6.2}$$

where the $\bar{\kappa}_{\mathrm{l,anh}}$ is the mean value of the lattice thermal conductivity of the pure XNiSn and X'NiSn half-Heuslers. Considering the half-Heusler with composition $X_{\mathrm{x}}X'_{\mathrm{1\text{-}x}}$NiSn, then the mean value is given as

$$\bar{\kappa}_{\mathrm{l,anh}} = x \times \kappa_{\mathrm{l,anh}}^{X\mathrm{NiSn}} + (1-x) \times \kappa_{\mathrm{l,anh}}^{X'\mathrm{NiSn}}. \tag{6.3}$$

Further, by assuming that the same synthesis procedure within the same paper produced the same microstructure for all of the compositions, the effect from grain boundary scattering on the total lattice thermal conductivity can be eliminated by subtracting equation (6.2) from (6.1). One obtains an expression for the effect of mass-disorder

scattering which we denote $\kappa'_{\mathrm{l,md}}$,

$$\frac{1}{\kappa'_{\mathrm{l,md}}} = \frac{1}{\kappa_{\mathrm{l,tot}}} - \frac{1}{\kappa'_{\mathrm{l,tot}}} = \frac{1}{\kappa_{\mathrm{l,anh}}} - \frac{1}{\bar{\kappa}_{\mathrm{l,anh}}} + \frac{1}{\kappa_{\mathrm{l,md}}} \approx \frac{1}{\kappa_{\mathrm{l,md}}}. \tag{6.4}$$

Also, one assumes equal contributions from anharmonic scattering in a composition with mass-disorder and the pure half-Heusler. Therefore, the resulting $\kappa'_{\mathrm{l,md}}$ should be relatively similar independent of the synthesis method. The calculated $\kappa'_{\mathrm{l,md}}$ is not a contribution to the total κ_{l}, but a value expressing the effect of mass-disorder scattering with respect to the composition. Thus, one can now compare the κ_{l} obtained with the virtual crystal approximation with experiments in the literature in more direct manner.

Table 6.3 shows the total κ_{l} for various compositions and the effect of mass-disorder scattering $\kappa'_{\mathrm{l,md}}$. The theory is compared to experimental values from the literature. Consider the composition $Ti_{0.5}Hf_{0.5}NiSn$ from the theory: the value for $\kappa'_{\mathrm{l,md}}$ is obtained by considering the inverse κ_{l} for $Ti_{0.5}Hf_{0.5}NiSn$ with mass-disorder and subtracting the inverse mean value of the bulk conductivity $\kappa'_{\mathrm{l,tot}}$, as described in equation (6.4). A similar procedure is done for the experimental value of $\kappa'_{\mathrm{l,md}}$. In the case of $Ti_{0.5}Hf_{0.5}NiSn$: the calculated κ_{l} and the values from experimental measurements in the literature differ by 1 W/mK; however, by applying the model to calculate the effect of alloying shows reasonably similar values of $\kappa'_{\mathrm{l,md}}$. The other compositions also shows reasonable similarities with a higher variation in both κ_{l} and $\kappa'_{\mathrm{l,md}}$.

There are uncertainties in the approximation to exclude the effect of boundaries from the lattice thermal conductivity. The boundaries from multiphase compositions and grain boundaries are equally treated; it is also assumed that the microstructures in *X*NiSn, *X*′NiSn and $X_xX'_{1-x}$NiSn are the same, which are most probably not the case. Despite these uncertainties, the role of mass-disorder from the virtual crystal approximation are comparable with the experimental values.

Table 6.3: Theoretical and experimental κ_{l} for binary alloys are represented in the first column. The second column represents the effect of mass-disorder scattering $\kappa'_{\mathrm{l,md}}$ with respect to the composition.

Composition	κ_{l} [W/mK]	$\kappa'_{\mathrm{l,md}}$ [W/mK]	Ref.
$Ti_{0.75}Zr_{0.25}NiSn$	9.3	24.45	Theory
	7.2*	27.94	[26]
	7.0*	21.00	[15]
$Ti_{0.5}Zr_{0.5}NiSn$	8.5	18.67	Theory
	7.4*	27.31	[26]
	8.0*	29.33	[15]
	4.9	10.69	[18]
$Ti_{0.25}Zr_{0.75}NiSn$	8.9	19.68	Theory
	7.2*	22.01	[26]
	7.3*	19.62	[15]
$Zr_{0.5}Hf_{0.5}NiSn$	5.3	7.84	Theory
	4.4	10.18	[18]
	4.3	8.00	[16]
	3.1	5.81	[23]
	3.2	8.75	[36]
	3.7	8.19	[78]
$Zr_{0.4}Hf_{0.6}NiSn$	5.4	8.19	Theory
	4.0	9.93	[78]
	3.0*	8.00	[33]
$Ti_{0.5}Hf_{0.5}NiSn$	4.8	7.02	Theory
	4.4	9.78	[18]
	3.7**	8.59	[23]
	3.7**	7.30	[79]

Note: Entries with * represents compositions with 5 % doping of Sb on the Sn-site, and entries with ** represents compositions with 2 % doping of Sb on the Sn-site.

6.2.3 Fitting of the Grain Sizes

The decrease of κ_l as a function of alloy percentage in a binary substitution was demonstrated in figure 5.11. A comparison with experimental measurements in the literature is presented; however, the theory does not include scattering from grain boundaries, and κ_l is expected to be overestimated. Katayama et. al [79] prepared half-Heusler alloys with composition $Ti_{1-x}Hf_xNiSn$, whereas Liu et al. [78] prepared $Zr_{1-x}Hf_xNiSn$. The theory overestimates all values for lattice thermal conductivity given in [78, 79]. The articles did not report any grain sizes; therefore, the average grain size was used as a fitting parameter. The grain size was set to $200\ \mathrm{nm}$ and $150\ \mathrm{nm}$ for the results from Katayama et al. and Liu et al., respectively. The results are shown in figure 6.3. The experimen-

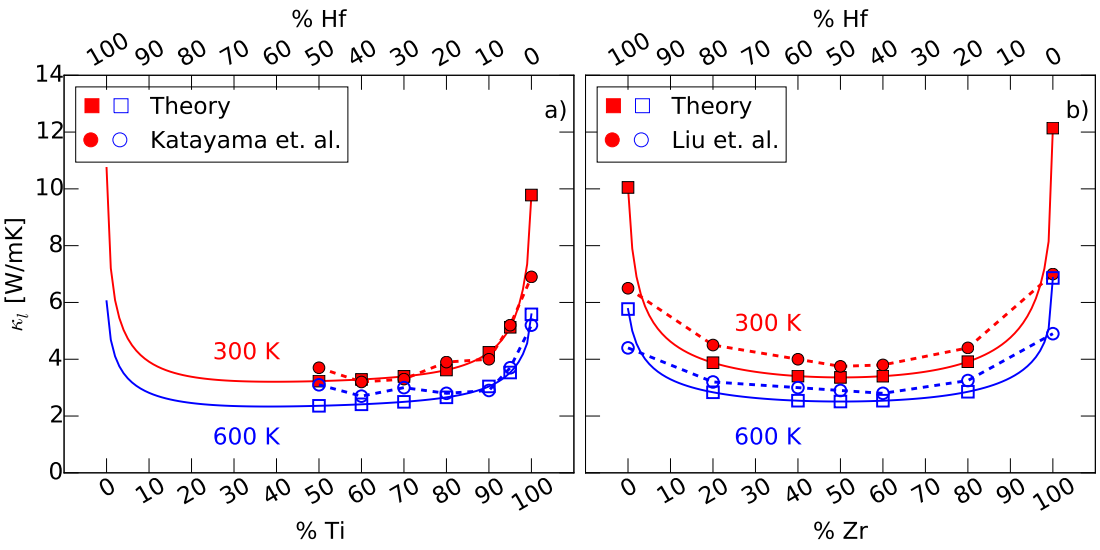

Figure 6.3: Lattice thermal conductivity as a function of binary substitution on the *X*-site. The squares are the theory with a solid line, and circles are the experimental results reproduced from [78, 79]. The dashed line is a guide to the eye to illustrate the general trend. The filled and unfilled markers are the κ_l at $300\ \mathrm{K}$ and $600\ \mathrm{K}$, respectively. Figure a) show the κ_l with Ti:Hf substitution fitted to an average grain size of $200\ \mathrm{nm}$, and figure b) is Zr:Hf substitution with an average grain size of $150\ \mathrm{nm}$.

tal results are shown as circles and theory are shown as squares; the filled and unfilled markers are at $300\ \mathrm{K}$ and $600\ \mathrm{K}$, respectively. The dashed line is a guide to the eye to illustrate the general trend. Both articles show a decrease in κ_l with alloy percentages up to 20%, which is consistent with the theory. However, the theory overestimates κ_l for the pure half-Heusler. Katayama et al. reported a majority of single phase TiNiSn with a small amount of metallic phases after 2 weeks of annealing at $1073\ \mathrm{K}$. The metallic phases have been demonstrated to have a significant effect on κ_l [80]. Downie et al.

prepared the compositions $TiNi_{1+y}Sn$ with $y \leq 0.06$, and the measured κ_l reduced with increasing amount of Ni. In fact, there was a reduction of κ_l by 2 W/mK at both 400 K and 700 K when going from zero excess Ni to $y = 0.06$.

6.2.4 Calculations Based on Relevant Grain Sizes

There are reports of the average grain size in the literature, and basing the average grain size upon the reported values have shown good accordance between theory and experimental measurements. At 300 K, the theory predicts the κ_l in TiNiSn with an average grain size of $10\ \mu\mathrm{m}$ to be $14.29\ \mathrm{W/mK}$, and with an average grain size $0.05\ \mu\mathrm{m}$ to be $6.11\ \mathrm{W/mK}$. The experimental κ_l for $TiNiSn_{0.95}Sb_{0.05}$ was reported to be $10\ \mathrm{W/mK}$ and $4\ \mathrm{W/mK}$ with reported grain sizes of $10\ \mu\mathrm{m}$ and $0.05\ \mu\mathrm{m}$, respectively [26]. They reported a single-phase half-Heusler by x-ray diffraction. The theory captures the same trend as the experiment, but the theory overestimates κ_l by 2-3 W/mK.

Lattice thermal conductivity as a function of temperature is shown in figure 6.4. Triangles are the κ_l with a combination of anharmonic scattering and mass-disorder scattering; squares represents κ_l with a combination of anharmonic, mass-disorder and grain boundary scattering and circles are experimental results found in the literature [29, 34, 35]. The average grain size is based on the reported values from the said papers. Bhardwaj et al. [35] characterized the microstructure of $Zr_{0.25}Hf_{0.75}NiSn$ with x-ray diffraction analysis and transmission electron microscope images, and concluded that the average grain size of that composition is in the range of 30-100 nm. Yu et al. [34] reported an average grain size in the range of 300-400 nm in composition $Zr_{0.4}Hf_{0.6}NiSn_{0.98}Sb_{0.02}$ with x-ray diffraction analysis and scanning electron microscope images. Joshi et al. [81] reported an average grain size to be in the range of 200-300 nm for the the composition $Zr_{0.25}Hf_{0.75}NiSn_{0.99}Sb_{0.01}$ from x-ray diffraction and transmission electron microscope images.

A decrease in κ_l as a function of temperature is observed for all compositions. However, the calculated κ_l is too high compared to the experimental results if one does not consider scattering from grain boundaries. Combining the anharmonic and mass-disorder scattering with grain boundary scattering results in further reduction of κ_l. The lowest temperature dependence of κ_l is when the grain size is the smallest, i.e. figure 6.4b) with a grain size of 50 nm. The theory reproduces the temperature dependence observed from experimental measurements of κ_l in the literature; however, the theory overestimates the κ_l in comparison with the experimental values in [29, 34, 35].

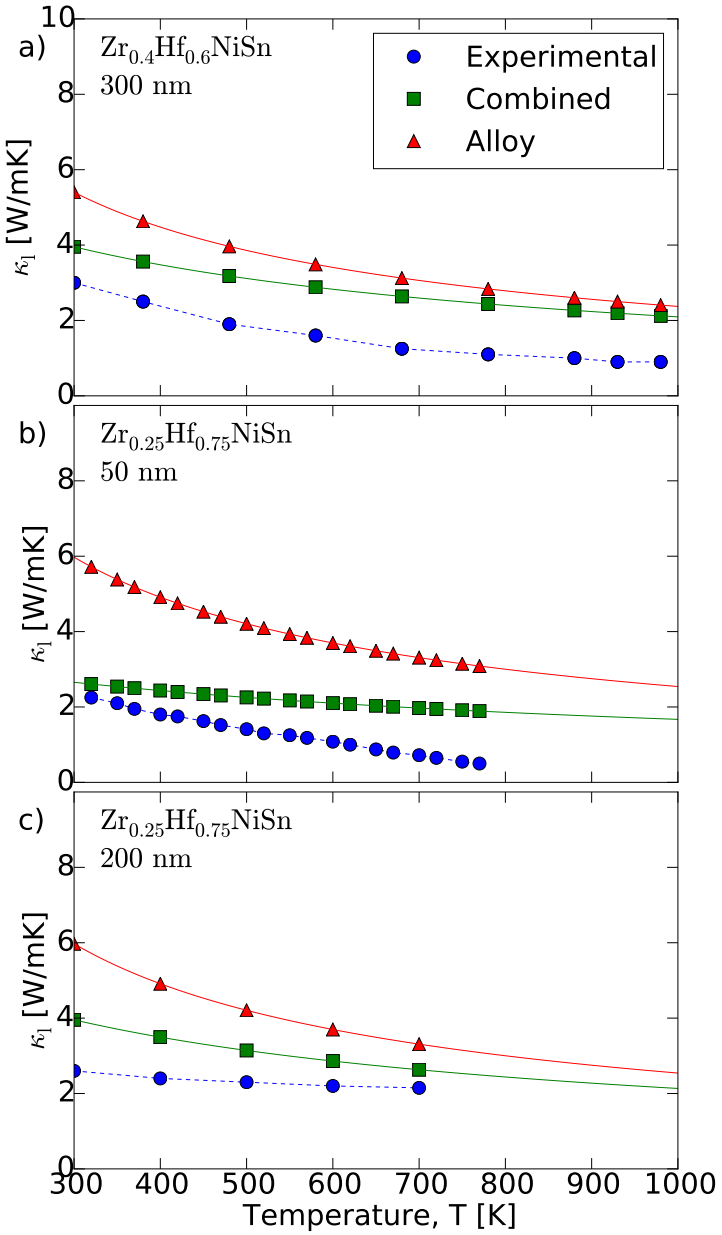

Figure 6.4: Lattice thermal conductivity as a function of temperature. The triangles are κ_l with anharmonic scattering and mass-disorder scattering, the squares represents κ_l with a combination of anharmonic, mass-disorder and grain boundary scattering and circles are experimental results found in the literature. a) κ_l for the composition $Zr_{0.4}Hf_{0.6}NiSn$ with an average grain size of 300 nm, and the experimental results are from [34]. b) κ_l for the composition $Zr_{0.25}Hf_{0.75}NiSn$ with grain size of 50 nm, and the experimental results are from [35]. c) κ_l for the composition $Zr_{0.25}Hf_{0.75}NiSn$ with an average grain size of 200 nm, and the experimental results are from [29]. The composition from Yu et al. [34] and Joshi et al. [29] had a doping concentration on the Sn-site of 2% Sb and 1% Sb, respectively.

6.3 Validity of the Scattering Models

The observed overestimation of the lattice thermal conductivity may be related to the scattering models. The mass-disorder is considered to be a perturbation, where the disorder is assumed to be distributed completely random; thus, completely ignoring multiphase behavior and the possibility for phonons to be scattered by the interface between the phases. There have been reports in the literature that the multiphase behavior may be beneficial for thermoelectric properties [24, 30, 82].

Schwall and Balke reported three phases in $Ti_{0.5}Zr_{0.25}Hf_{0.25}NiSn$ where two of them is either Ti-rich or Hf-rich [30]. A scattered phonon from the interface between the Ti-rich phase and Hf-rich phase can be described by the acoustic mismatch model, which describes the two sides of the phase-interface as two different mediums. It assumes complete specularity and accounts for the possibility for reflection, refraction and the angle of the incident phonon. The reflection and refraction is described by the acoustic analog to Snell's law, and a more detailed description of the model can be found in [83].

The effects on κ_{l} from phase-interface scattering are believed to be very small if the grain sizes is much smaller than the size of the observed phase-domains. The element-specific EDX mappings in figure 2 in [30] suggests domain size in the order of $\sim 10\ \mu m$ or higher. The grain boundary scattering has a big impact on the κ_{l} with an average grain size of $< 2\,\mu\mathrm{m}$. Thus, scattering of the acoustic phonons may already be mostly utilized with sufficiently low grain size. However, multiphase behavior may have a significant effect if the phases and grains are of the same order.

The grain boundary scattering model considers all grains to be equal in geometry with an average grain size, and it does not consider a distribution of grain sizes. Moreover, it is assumed that phonons scatter completely diffusive at the interface between each grain; that is, there is no reflection of phonons. It is believed that the diffusive scattering model will overestimate the calculated κ_{l} due to no back-scattering of phonons at the grain boundaries. There exists a parameter called the *specularity parameter* which accounts for the possibility to have reflection of phonons at the boundary [48]. The specularity parameter describes how many times a phonon is reflected before it is diffusively scattered. There are few attempts to quantify the specularity parameter between two grains or phases in the literature; however, the attempts that have been made are typically based on matching the results from BTE that includes the grain boundary relaxation time $1/\tau_{j\mathbf{q}^{\mathrm{bs}}}$ to thin film or nanowire measurements [84]. Without any prior knowledge of the specularity parameter, it is just a fitting parameter to get good agreement between theory and experiments; thus, it is not included in these calculations.

Chapter 7

Conclusions

Lattice thermal conductivity is an important property in thermoelectric generators and coolers; also, an understanding of the heat conduction from lattice vibrations is useful in thermal isolation materials for example for the development of zero emission buildings. The efficiency of such applications depends on the nano-scale thermal conductivity in their constituting materials. It is possible to tailor the nano-materials to exhibit the desired thermal properties for a particular application. In this thesis, the tailoring of half-Heusler compounds as thermoelectric materials is discussed from a theoretical point of view.

The thermal conductivity has contributions from electrons and lattice vibrations. The lattice thermal conductivity can be calculated from first principles by considering the forces up to the third-order of the expanded crystal potential. The determination of lattice thermal conductivity was done by solving the Boltzmann transport equation for phonons within the relaxation time approximation (RTA). In the RTA, the relaxation time of a phonon mode was calculated while all other modes are considered to be in equilibrium. From these calculations, an understanding of the limiting factors of the three-phonon scattering events was obtained.

Pure *X*NiSn (*X*=Ti, Zr or Hf) shows too high lattice thermal conductivity to be applicable as an efficient thermoelectric material. One strategy to lower the κ_l is to have an isoelectronic substitution on the *X*-site in the *X*NiSn half-Heusler alloys where *X* = Ti, Zr, Hf. Introducing such alloying will break the symmetry of the unit cell, and explicit density functional theory calculations on such crystals are very time consuming. The effects of alloying in $Ti_xZr_yHf_{1-x-y}NiSn$ on the κ_l in this work was explored within the virtual crystal approximation (VCA). The result was mapped on a ternary alloying diagram, and it was found that the greatest reduction of κ_l comes from compositions with the highest mass-difference. The lowest κ_l was thus obtained in the composition

$Ti_{0.5}Hf_{0.5}NiSn$. The effects from mass-disorder scattering from theory and experimental results was found to be comparable.

The effect on the lattice thermal conductivity from nanostructuring was studied with an empirical model due to the computational expenses with explicit DFT calculations on nanostructured materials. Phonons incident on a grain boundary are diffusively scattered and the relaxation times can be calculated by considering a particular value of the grain size representing that for all the grains. For grain sizes less than 0.5 μm, a significant reduction in κ_l was observed. For comparison, the grain size was chosen with respect to reported values in the literature. The resulting κ_l from the theory showed a slight overestimation compared to the experiments; however, the theory captured the temperature dependence of the κ_l. The orientations and distributions of the grains are not included in this model; also, it disregards the possibility for a phonon wave packet to be reflected at the boundary, which will have an impact on the thermal conductivity. The possibility for reflection can be introduced by including a specularity parameter, and a lower κ_l can be obtained. However, in this thesis the specularity has been disregarded because of the lack of literature on the topic. The multiphase behavior in half-Heusler alloys has been reported to be beneficial for a low κ_l, but the VCA fails to capture the scattering from the boundaries between two phases. If the phase-domain is in the order of $10\ \mu m$ or higher, it is believed the multiphase behavior have less of an effect on the lattice thermal conductivity with sufficiently low grain sizes because the scattering of the lower energetic phonons are already mostly utilized.

In conclusion, the approach presented in this thesis allows calculations of κ_l for any composition of *X*NiSn in combination with scattering due to grain boundaries. All ingredients to calculate κ_l were computed from first principles: the vibrational properties and anharmonic scattering rates. This approach reproduces the available experimental results in the literature for κ_l when combining the scattering mechanisms: anharmonic, mass-disorder and grain boundary scattering. The addition of mass-disorder scattering were observed to scatter phonons at higher frequencies; whilst, grain boundaries scattered the phonons with lower frequency. These findings may be beneficial for further investigation of the *X*NiSn half-Heusler compounds, both for experimentalists and theoreticians. The results may be used to decide which compound to make or it can be used as a reference to other calculation methods. Also, the methods presented to calculate the lattice thermal conductivity are transferable to other half-Heusler alloys or other thermoelectric materials. These methods are not confined to the field of thermoelectricity but may as well be used to understand heat conduction from lattice vibrations in isolation materials or other application areas where an understanding of heat conduction in the constituting materials is important.

Further work on this topic would include a calculation of the dispersion in an ordered alloy, e.g. $Ti_{0.5}Hf_{0.5}NiSn$: the dispersion may verify the assumptions regarding the structure of the dispersion for an increased possibility for three-phonon scattering events. It would be interesting to implement another description of boundaries to capture transmission probabilities, angle of the incident waves and the mismatch in acoustic dispersion to check if such a model would reproduce the experimental values even better; however, such implementation would require a lot more prior knowledge of the materials.

Bibliography

1. Tritt, T. M. & Subramanian, M. A. Thermoelectric Materials, Phenomena, and Applications: A Bird's Eye View. *MRS Bulletin* **31,** 188–198 (2006).
2. Ioffe, A. *Semiconductor Thermoelements and Thermoelectric Cooling* 1st (Infosearch, 1957).
3. Goldsmid, H. & Nolas, G. *A review of the new thermoelectric materials* in *20th International Conference on Thermoelectrics, Proceedings* (2001).
4. Snyder, G. J. & Toberer, E. S. Complex thermoelectric materials. *Nature Materials* **7,** 105 –114 (2008).
5. Chen, S. & Ren, Z. Recent progress of half-Heusler for moderate temperature thermoelectric applications. *Materials Today* **16,** 387 –395 (2013).
6. Rull-Bravo, M., Moure, A., Fernandez, J. F. & Martin-Gonzalez, M. Skutterudites as thermoelectric materials: revisited. *RSC Adv.* **5,** 41653–41667 (2015).
7. Salzgeber, K., Prenninger, P., Grytsiv, A., Rogl, P. & Bauer, E. Skutterudites: Thermoelectric Materials for Automotive Applications? *Journal of Electronic Materials* **39,** 2074–2078 (2009).
8. Iversen, B. B. *et al.* Why are Clathrates Good Candidates for Thermoelectric Materials? *Journal of Solid State Chemistry* **149,** 455 –458 (2000).
9. Takabatake, T., Suekuni, K., Nakayama, T. & Kaneshita, E. Phonon-glass electron-crystal thermoelectric clathrates: Experiments and theory. *Rev. Mod. Phys.* **86,** 669–716 (2014).
10. Momma, K. & Izumi, F. *VESTA3* for three-dimensional visualization of crystal, volumetric and morphology data. *Journal of Applied Crystallography* **44,** 1272–1276 (2011).
11. Carrete, J., Li, W., Mingo, N., Wang, S. & Curtarolo, S. Finding Unprecedentedly Low-Thermal-Conductivity Half-Heusler Semiconductors via High-Throughput Materials Modeling. *Phys. Rev. X* **4,** 011019 (2014).

12. Graf, T., Felser, C. & Parkin, S. S. Simple rules for the understanding of Heusler compounds. *Progress in Solid State Chemistry* **39,** 1 –50 (2011).

13. Aliev, F. G. *et al.* Gap at the Fermi level in the intermetallic vacancy system RBiSn(R=Ti,Zr,Hf). *Zeitschrift für Physik B Condensed Matter* **75,** 167–171 (1989).

14. Öğüt, S. & Rabe, K. M. Band gap and stability in the ternary intermetallic compounds NiSn *M* (*M* =Ti,Zr,Hf): A first-principles study. *Phys. Rev. B* **51,** 10443–10453 (1995).

15. Tritt, T. M. *et al. Effects of various grain structure and sizes on the thermal conductivity of Ti-based half-Heusler alloys* in *Thermoelectrics, 2001. Proceedings ICT 2001. XX International Conference on* (2001), 7–12.

16. Uher, C., Yang, J., Hu, S., Morelli, D. T. & Meisner, G. P. Transport properties of pure and doped *M* NiSn (*M* =Zr, Hf). *Phys. Rev. B* **59,** 8615–8621 (1999).

17. Shen, Q. *et al.* Effects of partial substitution of Ni by Pd on the thermoelectric properties of ZrNiSn-based half-Heusler compounds. *Applied Physics Letters* **79,** 4165–4167 (2001).

18. Hohl, H. *et al.* Efficient dopants for ZrNiSn-based thermoelectric materials. *Journal of Physics: Condensed Matter* **11,** 1697 (1999).

19. Kawaharada, Y., Uneda, H., Muta, H., Kurosaki, K. & Yamanaka, S. High temperature thermoelectric properties of NiZrSn half-Heusler compounds. *Journal of Alloys and Compounds* **364,** 59 –63 (2004).

20. Xie, W. *et al.* Recent Advances in Nanostructured Thermoelectric Half-Heusler Compounds. *Nanomaterials* **2,** 379 (2012).

21. Sakurada, S. & Shutoh, N. Effect of Ti substitution on the thermoelectric properties of (Zr,Hf)NiSn half-Heusler compounds. *Applied Physics Letters* **86** (2005).

22. Shutoh, N. & Sakurada, S. Thermoelectric properties of the $Ti_x(Zr_{0.5}Hf_{0.5})_{1-x}NiSn$ half-Heusler compounds. *Journal of Alloys and Compounds* **389,** 204 –208 (2005).

23. Kimura, Y., Ueno, H. & Mishima, Y. Thermoelectric Properties of Directionally Solidified Half-Heusler ($M^a_{0.5}$, $M^b_{0.5}$)NiSn (M^a, M^b = Hf, Zr, Ti) Alloys. *Journal of Electronic Materials* **38,** 934–939 (2009).

24. Downie, R. A., MacLaren, D. A. & Bos, J.-W. G. Thermoelectric performance of multiphase XNiSn (X = Ti, Zr, Hf) half-Heusler alloys. *J. Mater. Chem. A* **2,** 6107–6114 (2014).

25. Gałazka, K. *et al.* Phase formation, stability, and oxidation in (Ti, Zr, Hf)NiSn half-Heusler compounds. *Physica Status Solidi (a)* **211,** 1259–1266 (2014).

26. Bhattacharya, S. *et al.* Effect of boundary scattering on the thermal conductivity of TiNiSn-based half-Heusler alloys. *Phys. Rev. B* **77,** 184203 (2008).

27. Muta, H., Kanemitsu, T., Kurosaki, K. & Yamanaka, S. Substitution Effect on Thermoelectric Properties of ZrNiSn Based Half-Heusler Compounds. *Materials Transactions* **47,** 1453–1457 (2006).

28. Kim, S.-W., Kimura, Y. & Mishima, Y. High temperature thermoelectric properties of TiNiSn-based half-Heusler compounds. *Intermetallics* **15,** 349–356 (2007).

29. Joshi, G. *et al.* Enhancement of thermoelectric figure-of-merit at low temperatures by titanium substitution for hafnium in n-type half-Heuslers $Hf_{0.75}TiZr_{0.25}NiSn_{0.99}Sb_{0.01}$. *Nano Energy* **2,** 82–87 (2013).

30. Schwall, M. & Balke, B. Phase separation as a key to a thermoelectric high efficiency. *Phys. Chem. Chem. Phys.* **15,** 1868–1872 (2013).

31. Culp, S. R., Poon, S. J., Hickman, N., Tritt, T. M. & Blumm, J. Effect of substitutions on the thermoelectric figure of merit of half-Heusler phases at 800 C. *Applied Physics Letters* **88** (2006).

32. Bhattacharya, S. *et al.* Grain structure effects on the lattice thermal conductivity of Ti-based half-Heusler alloys. *Applied Physics Letters* **81,** 43–45 (2002).

33. Yu, C. *et al.* High-performance half-Heusler thermoelectric materials $Hf_{1-x}Zr_xNiSn_{1-y}Sb_y$ prepared by levitation melting and spark plasma sintering. *Acta Materialia* **57,** 2757–2764 (2009).

34. Yu, C. *et al.* Reduced Grain Size and Improved Thermoelectric Properties of Melt Spun (Hf,Zr)NiSn Half-Heusler Alloys. *Journal of Electronic Materials* **39,** 2008–2012 (2009).

35. Bhardwaj, A. *et al.* Implications of nanostructuring on the thermoelectric properties in half-Heusler alloys. *Applied Physics Letters* **101** (2012).

36. Xie, H.-H. *et al.* Increased electrical conductivity in fine-grained (Zr,Hf)NiSn based thermoelectric materials with nanoscale precipitates. *Applied Physics Letters* **100** (2012).

37. Srivastava, G. P. *The Physics of Phonons* (CRC Press, 1990).

38. Willis, B. T. M. & Pryor, A. W. *Thermal Vibrations in Crystallography* (Cambridge University Press, 1975).

39. Dove, M. T. *Introduction to Lattice Dynamics* (Cambridge University Press, 1993).

40. A. A. Maradudin, G. H. W. & Montroll, E. W. *Theory of lattice dynamics in the harmonic approximation* (New York: Academic Press, 1963).

41. Kittel, C. *Introduction to Solid State Physics* 8th Ed. (Wiley, 2004).

42. Hofmann, P. *Solid State Physics: An Introduction* (Wiley, 2011).

43. *Brillouin zone* [Online; accessed 30-Aug-2015]. <https://en.wikipedia.org/wiki/Brillouin_zone> (2015).

44. Brüesch, P. *Phonons: Theory and Experiments I* (Springer-Verlag Berlin Heidelberg, 1982).

45. Giannozzi, P., de Gironcoli, S., Pavone, P. & Baroni, S. *Ab initio* calculation of phonon dispersions in semiconductors. *Phys. Rev. B* **43,** 7231–7242 (1991).

46. Tamura, S. Isotope scattering of dispersive phonons in Ge. *Phys. Rev. B* **27,** 858–866 (1983).

47. Tamura, S. Isotope scattering of large-wave-vector phonons in GaAs and InSb: Deformation-dipole and overlap-shell models. *Phys. Rev. B* **30,** 849–854 (1984).

48. Ziman, J. M. *Electrons and Phonons: The Theory of Transport Phenomena in Solids* (Oxford Classic Texts in the Physical Sciences, 1960).

49. Kresse, G. & Furthmüller, J. Efficient iterative schemes for *ab initio* total-energy calculations using a plane-wave basis set. *Phys. Rev. B* **54,** 11169–11186 (1996).

50. Kresse, G. & Joubert, D. From ultrasoft pseudopotentials to the projector augmented-wave method. *Phys. Rev. B* **59,** 1758–1775 (1999).

51. David S. Sholl, J. A. S. *Density Functional Theory: A Practical Introduction* (John Wiley & Sons, Inc., 2009).

52. Giustino, F. *Materials Modelling using Density Functional Theory: Properties and Predictions* (Oxford University Press, 2014).

53. Engel, E. & Dreizler, R. M. *Density Functional Theory: An advanced Course* (Springer Berlin Heidelberg, 2011).

54. Hohenberg, P. & Kohn, W. Inhomogeneous Electron Gas. *Phys. Rev.* **136,** B864–B871 (1964).

55. Kohn, W. & Sham, L. J. Self-Consistent Equations Including Exchange and Correlation Effects. *Phys. Rev.* **140,** A1133–A1138 (1965).

56. Lee, J. G. *Computational Materials Science: An Introduction* (CRC Press, 2011).

57. Perdew, J. P., Burke, K. & Ernzerhof, M. Generalized Gradient Approximation Made Simple. *Phys. Rev. Lett.* **77,** 3865–3868 (1996).

58. Gonze, X. & Lee, C. Dynamical matrices, Born effective charges, dielectric permittivity tensors, and interatomic force constants from density-functional perturbation theory. *Phys. Rev. B* **55,** 10355–10368 (1997).

59. Baroni, S., de Gironcoli, S., Dal Corso, A. & Giannozzi, P. Phonons and related crystal properties from density-functional perturbation theory. *Rev. Mod. Phys.* **73,** 515–562 (2001).

60. Parlinski, K., Li, Z. Q. & Kawazoe, Y. First-Principles Determination of the Soft Mode in Cubic ZrO_2. *Phys. Rev. Lett.* **78,** 4063–4066 (1997).

61. Chaput, L., Togo, A., Tanaka, I. & Hug, G. Phonon-phonon interactions in transition metals. *Phys. Rev. B* **84,** 094302 (2011).

62. Togo, A., Chaput, L. & Tanaka, I. Distributions of phonon lifetimes in Brillouin zones. *Phys. Rev. B* **91,** 094306 (2015).

63. Togo, A. & Tanaka, I. First principles phonon calculations in materials science. *Scripta Materialia* **108,** 1 –5 (2015).

64. MacDonald, A. H., Vosko, S. H. & Coleridge, P. T. Extensions of the tetrahedron method for evaluating spectral properties of solids. *Journal of Physics C: Solid State Physics* **12,** 2991 (1979).

65. Blöchl, P. E., Jepsen, O. & Andersen, O. K. Improved tetrahedron method for Brillouin-zone integrations. *Phys. Rev. B* **49,** 16223–16233 (1994).

66. Andrea, L., Hug, G. & Chaput, L. Ab initio phonon properties of half-Heusler NiTiSn, NiZrSn and NiHfSn. *Journal of Physics: Condensed Matter* **27,** 425401 (2015).

67. Page, A., Uher, C., Poudeu, P. F. & Van der Ven, A. Phase separation of full-Heusler nanostructures in half-Heusler thermoelectrics and vibrational properties from first-principles calculations. *Phys. Rev. B* **92,** 174102 (2015).

68. Downie, R. A., Barczak, S. A., Smith, R. I. & Bos, J. W. G. Compositions and thermoelectric properties of XNiSn (X = Ti, Zr, Hf) half-Heusler alloys. *J. Mater. Chem. C* **3,** 10534–10542 (2015).

69. Csonka, G. I. *et al.* Assessing the performance of recent density functionals for bulk solids. *Phys. Rev. B* **79,** 155107 (2009).

70. Abeles, B. Lattice Thermal Conductivity of Disordered Semiconductor Alloys at High Temperatures. *Phys. Rev.* **131,** 1906–1911 (1963).

71. Garg, J., Bonini, N., Kozinsky, B. & Marzari, N. Role of Disorder and Anharmonicity in the Thermal Conductivity of Silicon-Germanium Alloys: A First-Principles Study. *Phys. Rev. Lett.* **106,** 045901 (2011).

72. Kundu, A., Mingo, N., Broido, D. A. & Stewart, D. A. Role of light and heavy embedded nanoparticles on the thermal conductivity of SiGe alloys. *Phys. Rev. B* **84,** 125426 (2011).

73. Popović, Z., Kliche, G., Liu, R. & Aliev, F. Vibrational properties of MeNiSn (Me = Ti, Zr, Hf). *Solid State Communications* **74,** 829 –832 (1990).

74. Mestres, N., Calleja, J., Aliev, F. & Belogorokhov, A. Electron localization in the disordered conductors TiNiSn and HfNiSn observed by Raman and infrared spectroscopies. *Solid State Communications* **91,** 779 –784 (1994).

75. Wee, D., Kozinsky, B., Pavan, B. & Fornari, M. Quasiharmonic Vibrational Properties of TiNiSn from Ab Initio Phonons. *Journal of Electronic Materials* **41,** 977–983 (2012).

76. Haci Özişik, H. B. Ö. Kemal Çolakoğlu. Ab-initio first principles calculations on half-heusler NiYSn (Y=Zr, Hf) compounds. Part 1: Structural, lattice dynamical, and thermo dynamical properties. *Fizika* **154** (2010).

77. Chaput, L. Direct Solution to the Linearized Phonon Boltzmann Equation. *Phys. Rev. Lett.* **110,** 265506 (2013).

78. Liu, Y. *et al.* Demonstration of a phonon-glass electron-crystal strategy in (Hf,Zr)-NiSn half-Heusler thermoelectric materials by alloying. *J. Mater. Chem. A* **3,** 22716–22722 (2015).

79. Katayama, T., Kim, S. W., Kimura, Y. & Mishima, Y. The effects of quaternary additions on thermoelectric properties of TiNiSn-based half-heusler alloys. *Journal of Electronic Materials* **32,** 1160–1165 (2003).

80. Downie, R. A., MacLaren, D. A., Smith, R. I. & Bos, J. W. G. Enhanced thermoelectric performance in TiNiSn-based half-Heuslers. *Chem. Commun.* **49,** 4184–4186 (2013).

81. Joshi, G. *et al.* Enhancement in Thermoelectric Figure-Of-Merit of an N-Type Half-Heusler Compound by the Nanocomposite Approach. *Advanced Energy Materials* **1,** 643–647 (2011).

82. Populoh, S. *et al.* High figure of merit in (Ti,Zr,Hf)NiSn half-Heusler alloys. *Scripta Materialia* **66,** 1073 –1076 (2012).

83. Swartz, E. T. & Pohl, R. O. Thermal boundary resistance. *Rev. Mod. Phys.* **61,** 605–668 (1989).

84. Hurley, D., Shindé, S. L. & Piekos, E. S. in (eds Shindé, L. S. & Srivastava, P. G.) 175–205 (Springer New York, New York, NY, 2014).